Optimizing the Design of Partially and Fully Depleted MESFETs for Low Dropout Regulators

by

William Lepkowski

A Dissertation Presented in Partial Fulfillment
of the Requirements for the Degree
Doctor of Philosophy

ARIZONA STATE UNIVERSITY

December 2010

Optimizing the Design of Partially and Fully Depleted MESFETs for Low Dropout Regulators

by

William Lepkowski

has been approved

September 2010

Graduate Supervisory Committee:

Trevor Thornton, Chair
Bertan Bakkaloglu
Michael Goryll
Raja Ayyanar

ACCEPTED BY THE GRADUATE COLLEGE

ABSTRACT

The constant scaling of supply voltages in state-of-the-art CMOS processes has led to severe limitations for many analog circuit applications. Some CMOS processes have addressed this issue by adding high voltage MOSFETs to their process. Although it can be a completely viable solution, it usually requires a changing of the process flow or adding additional steps, which in turn, leads to an increase in fabrication costs. Si-MESFETs (silicon-metal-semiconductor-field-effect-transistors) from Arizona State University (ASU) on the other hand, have an inherent high voltage capability and can be added to any silicon-on-insulator (SOI) or silicon-on-sapphire (SOS) CMOS process free of cost. This has been proved at five different commercial foundries on technologies ranging from 0.5 to 0.15 μm.

Another critical issue facing CMOS processes on insulated substrates is the scaling of the thin silicon channel. Consequently, the future direction of SOI/SOS CMOS transistors may trend away from partially depleted (PD) transistors and towards fully depleted (FD) devices. FD-CMOS are already being implemented in multiple applications due to their very low power capability. Since the FD-CMOS market only figures to grow, it is appropriate that MESFETs also be developed for these processes.

The beginning of this thesis will focus on the device aspects of both PD and FD-MESFETs including their layout structure, DC and RF characteristics, and breakdown voltage. The second half will then shift the focus towards

implementing both types of MESFETs in an analog circuit application. Aside from their high breakdown ability, MESFETs also feature depletion mode operation, easy to adjust but well controlled threshold voltages, and f_T's up to 45 GHz. Those unique characteristics can allow certain designs that were previously difficult to implement or prohibitively expensive using conventional technologies to now be achieved. One such application which benefits is low dropout regulators (LDO). By utilizing an n-channel MESFET as the pass transistor, a LDO featuring very low dropout voltage, fast transient response, and stable operation can be achieved without an external capacitance. With the focus of this thesis being MESFET based LDOs, the device discussion will be mostly tailored towards optimally designing MESFETs for this particular application.

TABLES OF CONTENTS

Page

LIST OF TABLES viii

LIST OF FIGURES ix

CHAPTER

1. INTRODUCTION 1

1.1. MESFET Device Structure 1

1.2. MESFET Fabrication 4

1.3. Device Operation 7

1.4. Threshold Voltage..12

1.5. Tradeoff Between Breakdown Voltage and Transconductance Gain..18

1.6. Conclusion 21

2. SCALING PD-SOI MESFETs 22

2.1. Optimizing FD-MESFET Layout 22

2.2. DC Characterization..27

2.3. RF Characterization 32

2.4. MESFET Breakdown..37

2.5. Conclusion 41

3. FD-SOI & SOS MESFETS...44

3.1. FD-MESFET Architecture..44

3.2. Regions of Device Operation......................................49

CHAPTER Page

3.3. Turn-On Characteristics 54

3.4. Breakdown Mechanisms 56

3.5. Layout Alternatives and Potential Improvements 59

3.6. Modeling 64

3.7. Conclusion 69

4. N-MESFET LDO 70

4.1. PMOS LDO Overview 71

4.2. NMOS LDO Overview 76

4.3. N-MESFET LDO Overview 80

4.4. Selecting N-MESFET Pass Device 82

4.5. N-MESFET LDO Issues 83

4.6. Measurement Setup & PCB Board Design 87

4.7. Buffer Design and Transient Results 91

4.8. PSRR Results 93

4.9. Improving FD-MESFET LDOs 94

4.10. Conclusions 96

5. PD SOI MESFET LDOs 98

5.1. PD-MESFET LDO Overview 99

5.2. MESFET Pass Transistor Characteristics 102

5.3. PD-MESFET LDO Results 104

5.4. PD-MESFET LDO Results Across Temperature 108

CHAPTER Page

5.4. Low Voltage Opportunities and Body Bias Effects 111

5.5. Radiation Effects On MESFET LDO 114

5.6. Conclusion 118

6. CONCLUSION 120

6.1. Optimizing MESFET Pass Transistor........................120

6.2. Future LDO Opportunities 122

6.3. Other Potential Applications For MESFETs 123

6.4. Conclusion 124

REFERENCES 126

APPENDIX

A ELECTRICAL CHARACTERISTICS OF SURFACE MOUNT COMPONENTS USED ON PCB BOARDS FOR TESTING PD AND FD-MESFET LDO 130

B BARE DIE PICTURE OF LARGE PASS DEVICE 136

C ADDITIONAL WIDE TEMPERATURE MEASUREMENTS FROM HONEYWELL LDO 138

D ADDITIONAL RADIATION MEASUREMENTS FROM HONEYWELL LDO 143

E 3-D LAYOUT OF THE PD-MESFET PASS TRANSISTOR 147

LIST OF TABLES

Table Page

1. Scaling of Key Layout Rules for SB-MESFETs 26

2. Comparison of SB and BT-MESFETs in the 150 nm SOI CMOS Process 27

3. Area of MESFETs in Fig. 37a 62

4. Area of MESFETs in Fig. 39a 64

5. Improvements in Peregrine's Newer Process 96

6. LDO Performance Summary 97

7. Area of MESFETs in Fig. 62 99

LIST OF FIGURES

Figure Page

1. Cross-sectional view of a PD-MESFET structure which uses silicide block to create the SiO_2 spacers. 2

2. Fabrication steps for n-type MOSFETs and MESFETs in typical SOS or SOI CMOS processes [3]. 6

3. Cross-section of MESFET showing the lateral growth of the silicide contacts and lateral diffusion of the source/drain implant [12]. 7

4. FOC plot showing the different regions of operation for the MESFET. The device is from a 350 nm SOI CMOS process and has the following characteristics: W = 100 μm, L_g = 100 μm, and L_{aS} = L_{aD} = 0.6 μm. 9

5. Shows the variation of the depletion region under different regions of operation. a) V_{GS} = 0 V and V_{DS} = 0 V. b) Linear region. c) Pinch-off. d) Saturation region. e) Subthreshold region. 10

6. From the drain current curves, it can be seen that the MESFET's threshold voltage is becoming more positive with increasing gate length. Devices are from a 350 nm SOI CMOS process. 14

7. The Gummel plot shows the changes in DC operation for a 100 μm device with L_g = L_{aS} = L_{aD} = 0.6 μm between -60 to 150 ˚C. The device is from a 350 nm SOI CMOS process. 15

8. Structure of the MESFET PTAT used in [18]. 17

9. The tradeoff of peak transconductance and breakdown voltage is shown as a function of L_{aD}. Devices are from a 350 nm SOI CMOS process. 20

10. The transconductance of the device is greatly affected by L_{aS}. The degregation in transconductance can be minimized by appropriately sizing L_{aS}. Devices are from a 350 nm SOI CMOS process. 20

11. Top-view of PD-MESFET layout with the gate contacted inside the access region (silicide block is used to create the SiO_2 spacers). 23

12. Top-view of PD-MESFET layout with the gate contacted outside the access region to reduce L_g (silicide block is used to create the SiO_2 spacers). 23

13. Top-view of the BT PD-MESFET layout with the gate contacted outside the access region to reduce L_g. 26

14. Cross-sectional view of a PD-MESFET structure which uses the body-tie method to create oxide spacers. 27

15. Gummel plots for the smallest gate lengths fabricated on each process: a) 350 nm SOI CMOS and b) 150 nm SOI CMOS. 28

16. Threshold voltage extracted for each of the devices plotted in Fig. 15a-b. 30

17a-d). Measured family of curve plots corresponding to the four devices shown in Fig. 15b. In each graph the gate voltage is stepped from +0.5 V (uppermost curve) to -0.5 V in 0.25 V steps..31

18. Exhibits the trade-off in current drive and output resistance for the MESFETs in Fig. 17a-d. 32

19. The GSG structure used for RF characterization in the 150 nm process..33

20. Shows the roll-off in transconductance gain as L_{aD} increases from 300 nm to 1 µm on the 150 nm SOI CMOS process. 34

21. Shows the exponential scaling of the peak cut-off frequencies for MESFETs manufactured on 150 and 350 nm SOI CMOS processes. 35

22. A comparison of the f_T dependence on drain current for two MESFETs with nominally identical dimensions but fabricated using different SOI CMOS technology nodes. 36

23. Shows the cut-off frequencies versus drain current for select devices on the 150 nm SOI CMOS process. 37

24. Shows the breakdown voltage of various MESFET structures on the 150 nm SOI CMOS process. 40

25. The family of curves for a MESFET with L_g = 400 nm, L_{aS} = 600 nm and L_{aD} = 1 μm. The gate voltage is stepped from +0.4 V (uppermost curve) to -0.4 V in 0.1 V steps. 41

26. Comparison of Gummel plots for nominally identical L_g = 300 nm devices fabricated on the 150 nm process in August 2008 and May 2009. 43

27. 3-D rendering of the FD-SOI MESFET showing two conducting channels confined between islands of silicide. Electrical contact to each silicide island is provided by contacts to the first layer of metal interconnect. 46

28. Shows a cross-section in the y-z plane through the center of the device. The conducting channels are formed underneath the regions of silicide block. The current flows into the channels as indicated in the figure. 46

29. Threshold voltage of SOS MESFETs as a function of the channel width. The dashed lines are linear fits to the data [27]. 49

30. Lateral depletion for various regions of device operation. a) V_{GS} = 0 V and V_{DS} = 0 V. b) Linear region. c) Pinch-off. d) Saturation region. e) Subthreshold region. 52

31. Depletion growth from top view [13]. a) V_{GS} = 0 V and V_{DS} = 0 V. b) Linear region. c) Pinch-off. d) Saturation region. e) Subthreshold region. 53

32. Family of curves plot showing regions of MESFET operation. 54

33. The turn-on characteristics, I_D-V_{GS} for a) n-MESFETS (V_{DS} = 2 V) and b) p-MESFETs (V_{DS} = -2 V) for different channel widths. The insets show the magnitude of the gate current for L_{CW} = 0.25 μm. 55

34. The family of curves plot for a) the n-MESFET and b) the p-MESFET for gate voltages in the range of -0.5 to +0.5 V in 0.1 V steps. L_g^N = 1.8 μm, L_{CW}^N = 0.25 μm, L_g^P = 1.8 μm, and L_{CW}^P = 0.25 μm. 57

35. Compares the FOC for two devices that are nominally the same but with different doping profiles. The heavier doping improved the current drive and output resistance, but reduced the breakdown of the device. 59

36. 3-D rendering a FD-MESFET which extends silicide block into the gate region to reduce the effective gate length. 61

37. a) Compares two devices, that are nominally similar expect one utilizes the structure in Fig. 27 and the other uses Fig. 36. b) Compares the two devices after they have been normalized to current per unit area. 61

38. 3-D rendering of a FD-MESFET showing silicide block being offset in order to reduce the effective gate length...............................63

39. a) Compares the Gummel plots of three devices with different gate offsets on the MIT-LL process. b) Compares the same devices after they have been normalized to current per unit area. 63

40. Screen shot of how to change g_{min} in Cadence's Analog Design Environment. 65

41. Large signal model of a MESFET with the TOM3 sub-circuit. I_{BGD} and I_{BDS} are used to model the breakdown voltage in the circuit [23]. 66

42. Compares the measured results (solid line) to the simulated model (open circles) for the family of curves plot. 67

43. Compares the Gummel plots of the measured results (solid line) to the simulated model (open circles). 67

44. Compares the measured results (solid line) to the simulated model (open circles) for the drain current vs. gate voltage at $V_D = 2$ V. 68

45. Compares the g_m of the measured results (solid line) to the simulated model (open circles) at $V_D = 2$ V. 68

46. Basic circuit schematic of a LDO using a P-channel pass transistor in a common source configuration. The LDO has been compensated through C_{Load} and R_{ESR} [26]. 72

47. Range of stability chart for the Texas Instruments TPS76301 LDO. CSR refers to the ESR from the capacitor plus any external resistor if applicable [34]. 74

48. Includes the key internal parasitic components as well as the added external components that affect the stability of the PMOS LDO system. 75

49. Closed-loop gain response of a compensated LDO utilizing a PMOS pass transistor. 76

50. Circuit schematic of an LDO using a NMOS pass transistor in a common drain configuration. 78

51. Includes the key internal parasitic components that affect the stability of the NMOS LDO system. 78

52. Closed-loop gain response of an LDO utilizing a NMOS pass transistor. 79

53. Schematic of the LDO regulator using an N-MESFET pass transistor. 81

54. Measured and simulated drain and gate current of the scaled down MESFET used in the LDO. 83

55. Measured total dropout voltage resulting from the PMOS power-down switch and N-MESFET pass device. Also shown is the contribution from only the PMOS switch. 84

56. Measured ground current and current efficiency versus load current. At higher loads the current efficiency approaches 99%. 86

57. Multisim schematic of the PCB test board. 89

58. a) Die micrograph of the LDO. b) Picture of the bonded LDO on a gold-plated PCB. 90

59. Measured line regulation for both the low-to-high, a), and high-to-low transitions, b). The output voltage settles in less than ≤ 800 ns. 92

60. Measured load regulation for both the low-to-high, a), and high-to-low transitions, b). The output voltage settles in less than ≤ 1 μs...93

61. PSRR for loads of 10.8 and 34 mA..94

62. a) Compares MESFETs from FD and PD technologies to exhibit the gain in current drive and reduction in gate current with PD-MESFETs. b) Compares the two in Part a) after they have been normalized...99

63. Simple circuit schematic of the board level LDO design with a picture of the bonded out die. The device excluding pads is 0.73 x 0.55 mm while the cavity of the DIP-8 package is 7.37 x 4.32 mm. 100

64. PCB test board for the PD-MESFET LDO. 101

65. Schematic of PCB board used to test the PD-MESFET LDO. 102

66. Gummel plot of bonded out PD-MESFET pass transistor.......................103

67. a) FOC for MESFET pass transistor. b) FOC of MESFET that is 1/28 the size of the pass transistor. 104

68. a) Ground current with the low I_q error amplifier. b) Ground current with the low I_q error amplifier at light loads. 105

69. Transient line regulation with the low I_q error amplifier. I_{out} = 50 mA, $t_r = t_f$ = 200 ns and T = 50 μs. 106

70. Transient line regulation with the moderate I_q error amplifier. I_{out} = 50 mA, $t_r = t_f$ = 200 ns and T = 50 μs. 107

71. Transient load regulation with the low I_q error amplifier. V_{in} = 2.4 V, $t_r = t_f$ = 500 ns and T = 50 μs. 107

72. Transient load regulation with the moderate I_q error amplifier. V_{in} = 2.4 V, $t_r = t_f$ = 500 ns and T = 50 μs. 108

73. Line regulation at -50, 25, and +150^oC at a load of 50 mA. 109

74. Load regulation at -50, 25, and +150^oC at a V_{in} = 2.4 V. 110

75. The dropout voltage was measured up to 100 mA for -50, 25, and +150^oC and extrapolated from 100 to 150 mA. 110

76. a) Ground current at 85^oC with the low I_q error amplifier. b) Ground current at 85^oC with the low I_q error amplifier at light loads. 111

77. Compares the MESFET pass transistor at two different bulk-to-source voltages. 113

78. Compares the dropout voltage when the substrate of the MESFET is biased at 0 V and 1.8 V. 113

79. Compares the Gummel plot of MESFET pass device after an exposure dose of 1 Mrad(Si). 115

80. a) DC line regulation at various cumulative radiation exposures. b) Zoom in of Part a). 116

81. a) DC load regulation at various cumulative radiation exposures. b) Zoom in of Part a). 117

82. The output voltage of the PD-MESFET LDO at cumulative radiation doses of 10, 20, 50, 100, 200, 500, and 1000 krad(Si). 117

83. Electrical characteristics of the 2N3904 BJT. The 2N3094 was used with the Honeywell and Peregrine LDO to switch in a load for the load transient response. Refer to [45] for the complete datasheet. 131

84. The electrical characteristics of the NCS2001 operational amplifier which was used as the moderate I_q error amplifier in the Honeywell LDO. Refer to [46] for the complete datasheet. 132

85. The electrical characteristics of the LMP2231 operational amplifier which was used as the low I_q error amplifier in the Honeywell LDO. Refer to [47] for the complete datasheet. 135

86. Picture of bare die which includes the large MESFET device (upper left corner). Excluding pads, the MESFET is 0.73 x 0.55 mm. 137

87. The regulated output voltage of the Honeywell MESFET regulator was defined at a nominal load of 50 mA and measured over the temperature range of -50 to +150°C. 139

88. The line regulation in V/V from -50 to +150°C......................................139

89. The load regulation in mV/mA from -50 to +150°C. 140

90. Transient load regulation with the moderate I_q error amplifier at -50°C. V_{in} = 2.4 V, $t_r = t_f$ = 500 ns and T = 50 µs. 140

91. Transient load regulation with the moderate I_q error amplifier at +150°C. V_{in} = 2.4 V, $t_r = t_f$ = 500 ns and T = 50 µs...........................141

92. Transient line regulation with the moderate I_q error amplifier at -50°C. I_{out} = 50 mA, $t_r = t_f$ = 200 ns and T = 50 µs. 141

93. Transient line regulation with the moderate I_q error amplifier at +150°C. I_{out} = 50 mA, $t_r = t_f$ = 200 ns and T = 50 µs.........................142

94. Dropout voltage verses total ionizing dose at a load of 50 mA..............144

95. Transient line regulation with the moderate I_q error amplifier after 1 Mrad(Si). I_{out} = 50 mA, $t_r = t_f$ = 200 ns and T = 50 µs. 145

96. Transient load regulation with the moderate I_q error amplifier after 1 Mrad(Si). V_{in} = 2.4 V, $t_r = t_f$ = 500 ns and T = 50 µs. 145

97. Load regulation comparing the MESFET LDO immediately after 1 Mrad(Si) and after 24 hours of annealing...146

98. Line regulation comparing the MESFET LDO immediately after 1 Mrad(Si) and after 24 hours of annealing...146

99. Layout of two interdigitated fingers. 149

100. Shows a zoom in of Fig. 99. 149

101. Shows 4 of the 28 rows in the PD-MESFET pass transistor. 150

102. Zooms in on one section of Fig. 101 to show the source, drain, and gate lines..150

103. Removes the entire drain line and some of the metal layers of the source and gate lines in Fig. 102 to show how individual fingers connect to the bus lines. 151

104. Shows a zoomed in picture of Fig. 103 as well the via stack which connects the drain lines of the MESFET fingers (M1) to the drain bus line (M2-M6). 152

CHAPTER 1

INTRODUCTION

Si-MESFETs from ASU show significant promise for a variety of analog circuit applications due to their ability to be easily fabricated and integrated with SOS and SOI CMOS without changing any of the steps in a process flow [1-3]. Different reports [4-6] have considered Si-MESFETs on SOI, SOS, and bulk CMOS processes but in each case none of them were able to use a standard CMOS process flow. When comparing them to GaAs MESFETs, the enhanced performance must be considered with the high cost it takes to fabricate them along with their inability to integrate well with other devices. While the ASU MESFETs cannot compete with GaAs MESFET at microwave frequencies they do appear to be a strong low cost contender for analog applications below 10 GHz. This chapter gives a brief introduction to PD-MESFETs with a discussion on their structure, fabrication, operation, and basic DC characteristics.

1.1. MESFET DEVICE STRUCTURE

PD-MESFETs, like the one shown in Fig. 1, are four terminal majority carrier devices. This is in contrast to GaAs MESFETs which are three terminal devices due to their much thicker insulating layer which shields the effects of biases applied to the substrate [7]. Also, by being a PD device, the thickness of the active silicon layer is greater than the depletion width under the gate [8].

Our most common layout approach differentiates itself from other Si-MESFETs [4-6, 9] in that it uses the self-aligned silicide (salicide) step to form a near ideal Schottky contact over the lightly doped region under the gate. The current flows from the drain to the source and is controlled by the width of the depletion layer under the Schottky contact which is dependent on the magnitude of the voltage applied at the gate and the substrate [10]. For an n-type MESFET, the channel is lightly n-doped and heavily n-doped at the source and drain. The distance between the two silicon dioxide (SiO_2) spacers defines the gate length, L_g, and the length of the spacer on the drain (L_{aD}) and source (L_{aS}) ends defines the access lengths. As will be shown in subsequent chapters, how L_{aD} and L_{aS} are sized and spaced will be one of the most important determinants in defining the MESFET's performance. FD-MESFETs incorporate a similar layout but orientate the gate differently to overcome having a much thinner silicon channel. Refer to Fig. 27 and Fig. 28 in Chapter 3 for their corresponding structure and operation.

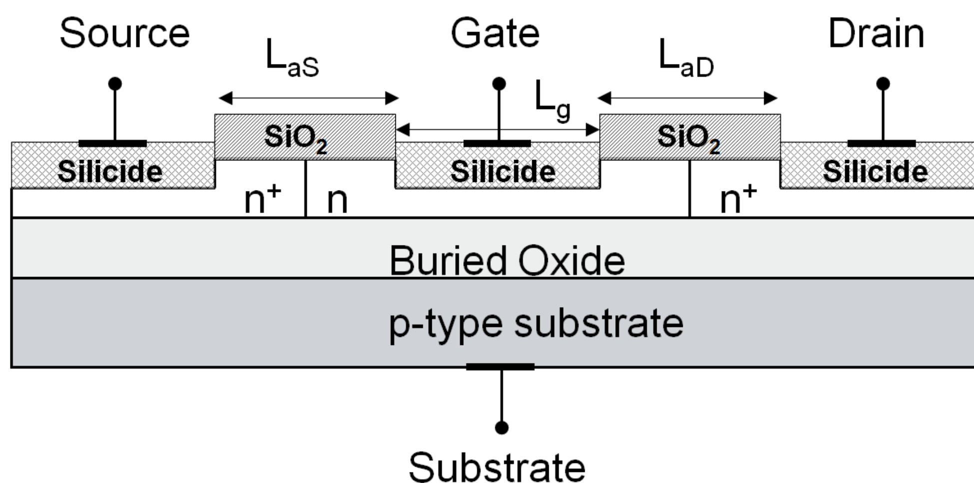

Fig. 1. Cross-sectional view of a PD-MESFET structure which uses silicide block to create the SiO_2 spacers.

Perhaps the most important parameter with respect to the MESFET's ability to operate is the thickness of the silicon channel. If the channel is too thin then the current drive is very low. On the other hand, if it is too thick, then the MESFET has little gate control and cannot pinch itself off. Based on a series of fabrication runs with various manufacturers, the ideal channel thickness for PD-MESFETs appears to be about 100 – 200 nm [2-3, 11]. That thickness in turn, usually corresponds to threshold voltages, V_t, somewhere in the manageable range of -0.5 to -1.5 V. Due to that channel thickness range, bulk CMOS technologies cannot be used for this type of MESFET fabrication. It is also why incorporating a technology with a thin silicon film on top of an insulting layer such as SOI or SOS is absolutely necessary. Refer to *Section 1.3* for more on the device operation.

Among other advantages of using an SOI or SOS technology over traditional bulk silicon is it provides higher frequency operation and lower power consumption. This is the result of the insulating layer reducing the overall parasitic capacitance and blocking the leakage path to the substrate. At higher temperatures, CMOS designed on bulk silicon can be limited by the large leakage current in the well junction which in turn can lead to latch-up [10]. Since MESFETs and CMOS alike are inherently insulated on SOI or SOS, they can be packed closer together in layout which helps offset some of the increased fabrication costs incurred by incorporating an insulating layer [8].

1.2. MESFET FABRICATION

The fabrication steps are exactly the same as the MOSFET's through the completion of the local oxidation of silicon (LOCOS) step (Fig. 2a). During the LOCOS step, the active layers of the MOSFETs and MESFETs are formed. Next, the gate stack of the MOSFET is patterned (Fig. 2b). In this stage, the silicon channel for the MESFET will be thinned slightly during the wafer cleaning. Afterwards, oxide is deposited across the entire wafer through plasma-enhanced chemical-vapor deposition (Fig. 2c). The MESFET then starts forming the Schottky gate by patterning silicon dioxide with the silicon block (SB) layer. This is the critical step in the MESFET process flow. The SB layer allows the MESFET to pattern oxide spacers and prevent shorting from the gate, drain, and source. Oxide not covered by the SB is then etched away leaving sidewall spacers for the MOSFET gate. Subsequently in (Fig. 2d), both the MESFET's and MOSFET's source and drain regions receive a highly doped implant. In this step a layer of photoresist is needed over the MESFET's channel region to keep it lightly doped. The photoresist is then removed and a layer of cobalt is deposited on the wafer. Areas of exposed silicon will react to form cobalt disilicide ($CoSi_2$) when annealed at a high temperature. This creates low resistive contacts for the gate, drain, and source (Fig. 2e). The silicon block layer prevents the oxide spacers from reacting with the cobalt. The unreacted cobalt is then removed and the MESFET continues through the rest of the back-end processing steps common to the CMOS [3]. Just to note, materials other than cobalt can be used for the

silicide step; however, it will affect the MESFET's work function and therefore its operation. Refer to [12] for an excellent discussion on different silicides with ASU's MESFETs.

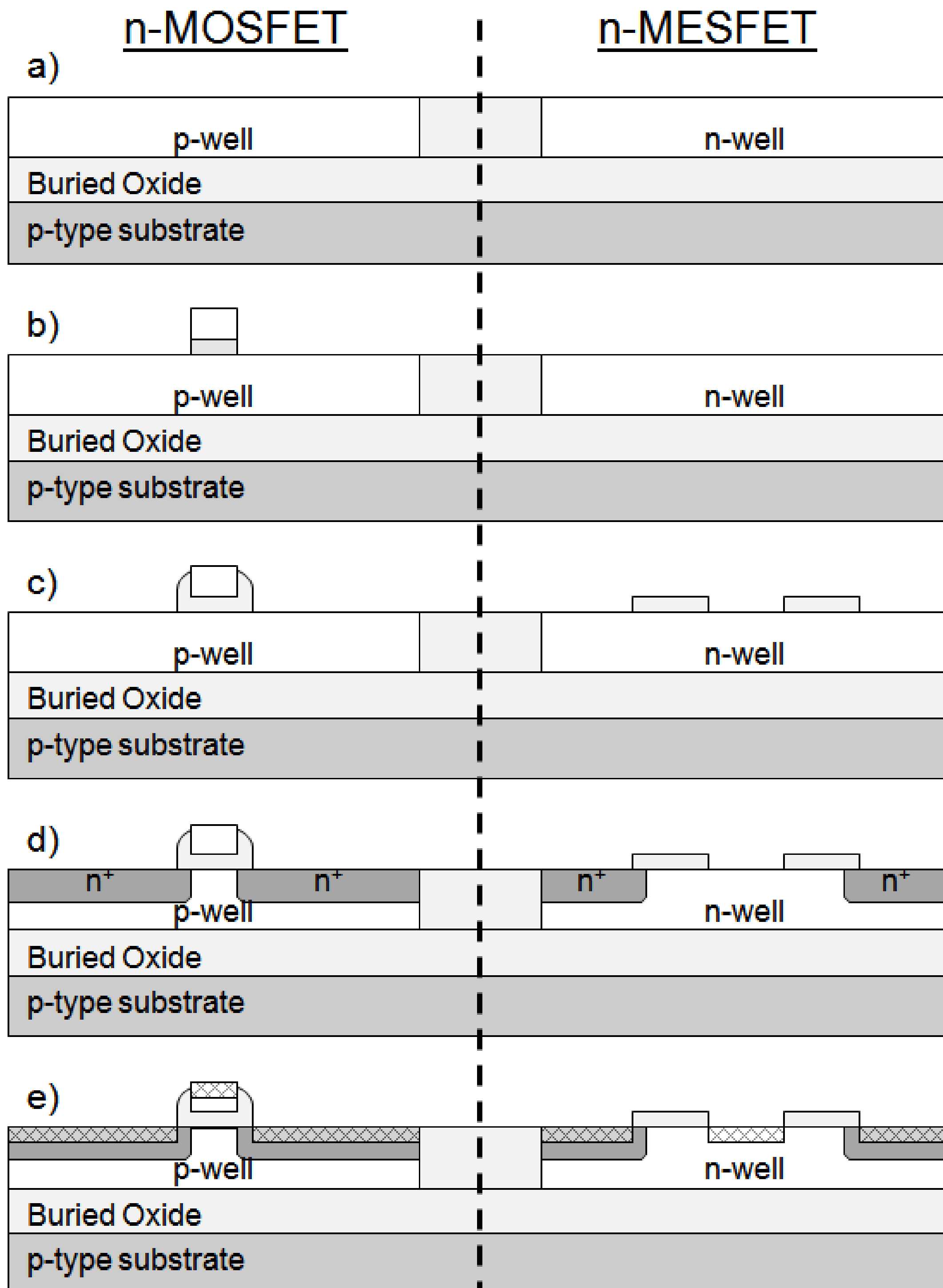

Fig. 2. Fabrication steps for n-type MOSFETs and MESFETs in typical SOS or SOI CMOS processes [3].

As shown in Fig. 1 and Fig. 2, the MESFET is not a self-aligned device. While the SiO_2 spacer patterned by the SB is called the access length, the true L_{aD} and L_{aS} is slightly shorter due to the lateral growth of silicide contacts at the drain, gate, and source and from the diffusion of the heavy source/drain implant (Fig. 3). Consequently, aside from the design rule that dictates the minimum width of the SB layer, these two issues impose a physical limit to the minimum size of the access region. Possible misalignment should also be taken into account when designing L_{aS} and L_{aD}. Also, the growth of the silicide at the gate contact results in the gate length being marginally larger than the spacing of the SB [3].

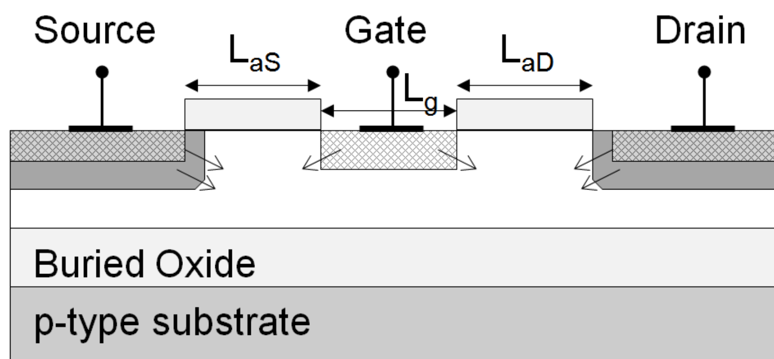

Fig. 3. Cross-section of MESFET showing the lateral growth of the silicide contacts and lateral diffusion of the source/drain implant [13].

1.3. DEVICE OPERATION

MESFETs are depletion mode devices which allows them to be turned on and saturated with a negative gate-to-source voltage, V_{GS}. Nevertheless, their drain current characteristics and regions of operation remain similar to MOSFETs. This can be seen in Equation 1.1 and Fig. 4 which shows the family of

curves (FOC) of one particular MESFET. Like a MOSFET, the MESFET follows a square law dependence above threshold and is affected by channel length modulation in the saturation region. The hyperbolic tangent function dominates in the linear region (Equation 1.2) when the drain-to-source voltages, V_{DS}, are small, but it quickly approaches unity. Thus, it can be neglected in the saturation region (Equation 1.3).

$$I_D \approx \beta(V_{GS} - V_t)^2(1 - \lambda V_{DS})\tanh(\alpha V_{DS}) \quad (1.1)$$

$$I_D \approx \beta(V_{GS} - V_t)^2 \tanh(\alpha V_{DS}) \quad (1.2)$$

$$I_D \approx \beta(V_{GS} - V_t)^2(1 - \lambda V_{DS}) \quad (1.3)$$

where

β = transconductance gain

λ = channel length modulation

α = saturation factor

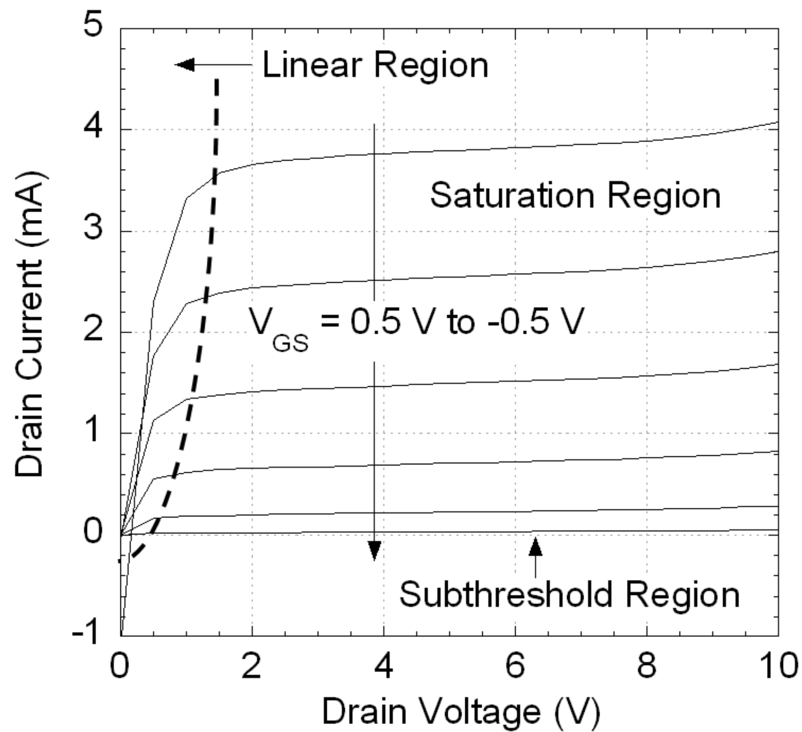

Fig. 4. Family of curves plot showing the different regions of operation for the MESFET. The device is from a 350 nm SOI CMOS process and has the following characteristics: W = 100 μm, L_g = 100 μm, and $L_{aS} = L_{aD}$ = 0.6 μm.

The way the MESFET operates is largely dictated by the depletion region under the gate which changes under different gate and drain biases. The depletion region can be seen in Fig. 5 for each region of operation characterized in Fig. 4. Due to the MESFET's relatively thin insulating layer, a depletion region controlled by the bulk-to-source voltage, V_{BS}, will also form at the bottom interface of the silicon channel. As V_{BS} becomes more negative, this depletion region grows causing the threshold voltage to become more positive and for the channel to pinch-off earlier [10].

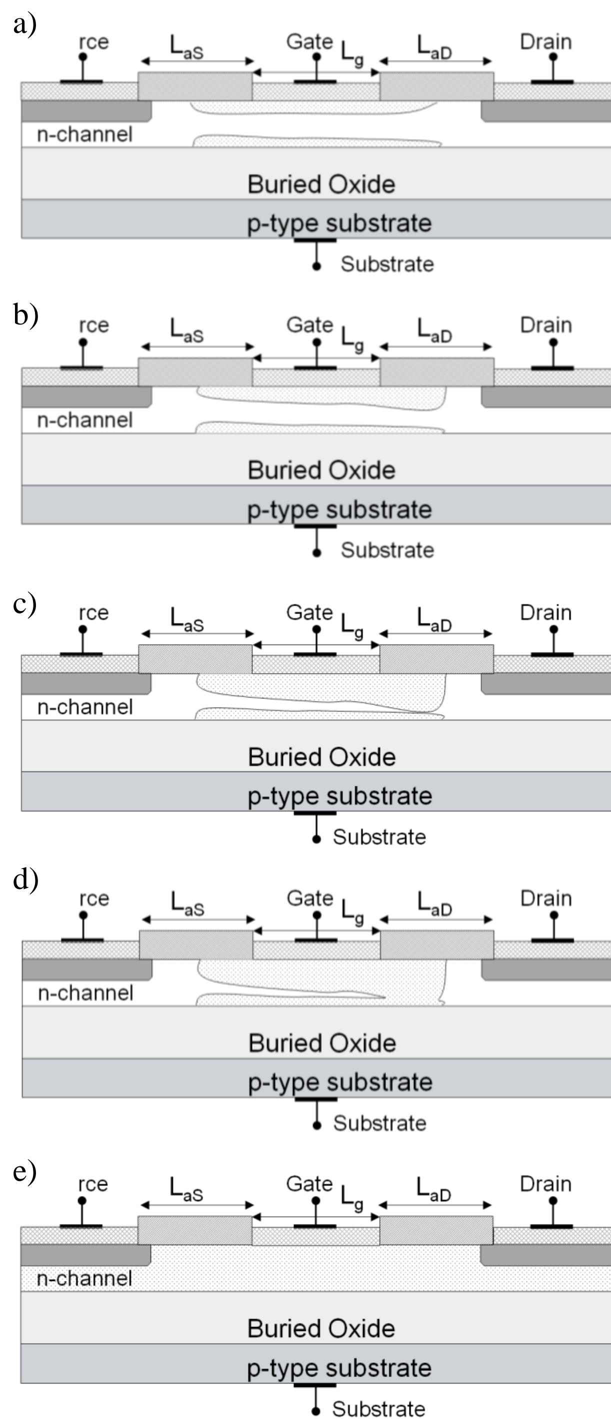

Fig. 5. Shows the variation of the depletion region under different regions of operation. a) $V_{GS} = 0$ V and $V_{DS} = 0$ V. b) Linear region: $V_{GS} = 0$ V and small V_{DS}. c) Pinch-off: $V_{GS} = 0$ V and $V_{DS} = V_{DSAT}$. d) Saturation region: $V_{GS} = 0$ V and $V_{DS} > V_{DSAT}$. e) Subthreshold region: $V_{GS} < V_t$ and $V_{DS} = 0$ V.

In the linear region which is characterized by low drain voltages and gate voltages above threshold, the drain current, I_D, increases proportionally with drain voltage at a fixed gate bias causing the MESFET to act like a resistor. As the drain voltage increases, the junction between the drain and the gate becomes more reversed biased causing the depletion region to widen faster towards the drain side. Consequently, the channel narrows at drain end and leads to the slope of the drain current rounding off (Fig. 4). The end of the linear region is marked by the touching of the top and bottom depletion regions. At that point the channel becomes pinched-off. Increasing the drain voltage any further saturates the current. Similarly to MOSFETs, the drain current in this region will increase slightly with drain voltage due to the effective channel length being reduced. As V_{GS} becomes more negative the depletion width increases due to the drain-gate junction becoming more reversed biased. This in turn causes the channel region to reduce, leads to smaller slopes of I_D in the linear region, and causes the MESFET to pinch-off at lower drain voltages [10, 14].

The last region of concern is the sub-threshold region. In this region the channel is fully depleted, but small amounts of current can still flow as a result of carriers in the space charge region [10]. As shown in Equation 1.4, the drain current varies exponentially with gate voltage. This region has been exploited by weakly inverted CMOS for ultra-low power applications, but due to the considerable reduction in drain current and transconductance gain, the operational frequency is usually limited to only a few MHz. On the other hand, the

MESFET's lightly doped channel leads to a larger mobility and cutoff frequencies 5-6 times larger than the weakly inverted CMOS with the same gate length and drain current [15]. Thus the MESFETs also show potential as micropower devices [16]. From the standpoint of the LDO, the MESFET pass transistor is a high power transistor and only enters the subthreshold region when the load is discounted or under very light load conditions. A subthreshold operated MESFET based error amplifier could be designed though for an ultra-low current LDO where power consumption considerably trumps transient line and load recovery speed.

$$I_D \approx \beta\left(e^{\frac{V_{GS} - V_t + \gamma V_{DS}}{2nU_T}}\right)^2 \tanh(\alpha V_{DS})(1 + \lambda V_{DS}) \quad (1.4)$$

where

γ = threshold-shifting parameter

n = ideality factor

U_T = thermal voltage (U_T = kT/q)

1.4. Threshold Voltage

Another interesting aspect of MESFETs is their well controlled but easy to adjust threshold voltage and the number of ways it can be accomplished. The first way involves biasing the substrate to purposely take advantage of the body effect PD-MESFETs are prone to seeing as a result of their relatively thin buried oxide layer. This option is not available in GaAs MESFETs since their insulting layer is

sufficiently thick [10]. The next option includes changing the thickness of the MESFET's silicon channel. The thicker the channel is, the more negative the gate-source bias needs to be to pinch the channel off. This of course might not be a desired route for PD-MESFETs since it involves the changing of process steps. Not only will that alter the operation of the CMOS devices on the die, but it could also add a physical cost to the fabrication. In the case of FD-MESFETs, the devices are laterally depleting so their channel thickness can easily be altered with no changes in the process. The last option comes about from the sizing of the gate length. As the gate length approaches the minimum feature size of the process, the MESFETs start to become heavily affected by short channel effects (SCE) (refer to Fig. 16). In Fig. 6, the effect of the gate length on four otherwise similar devices can be seen in the turn on of the drain current.

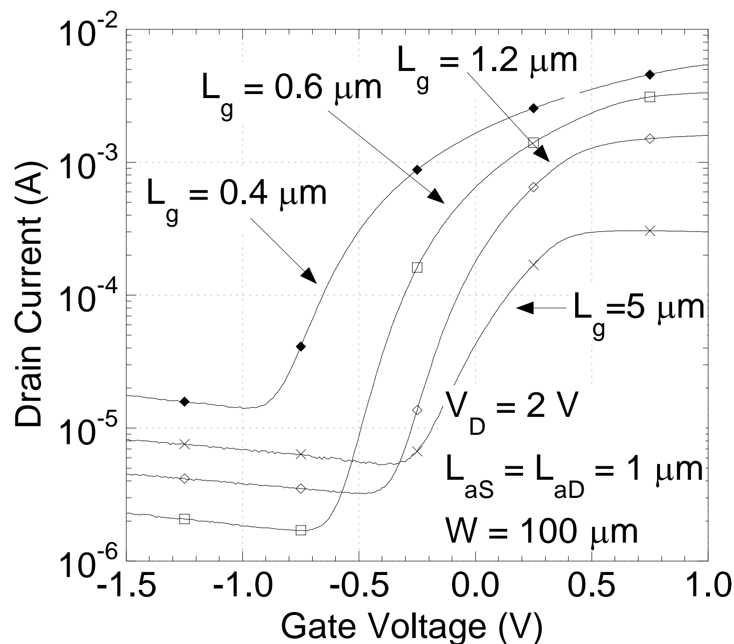

Fig. 6. From the drain current curves, it can be seen that the MESFET's threshold voltage is becoming more positive with increasing gate length. Devices are from a 350 nm SOI CMOS process.

The MESFET's ability to be able to easily generate large threshold voltage differences makes them potentially attractive for proportional to absolute temperature (PTAT) voltage references. PTATs can be difficult to design in standard CMOS processes since BJT and JFET transistors are generally not available and the threshold voltage difference in CMOS transistors is usually small. Alternatively, parasitic pn junctions can be used, but their electrical characteristics may not be controlled closely during fabrication [17].

In practice, PTATs are often matched with complementary to absolute temperature (CTAT) references in BGRs to cancel out the voltage drift in each reference to get a composite reference with very little drift [17-18]. With the

MESFET PTAT, a relatively low drift can be achieved without a CTAT. This is due to MESFETs seeing a very consistent threshold shift with respect to temperature. Fig. 7 shows how one device with a width (W) of 100 μm and L_g = 0.6 μm as it varies from -60 to 150 °C. While it is not shown here, MESFETs on the same 350 nm SOI CMOS process with gate lengths 0.4 – 1.2 μm showed almost the exact same shifts in drain current with respect to temperature.

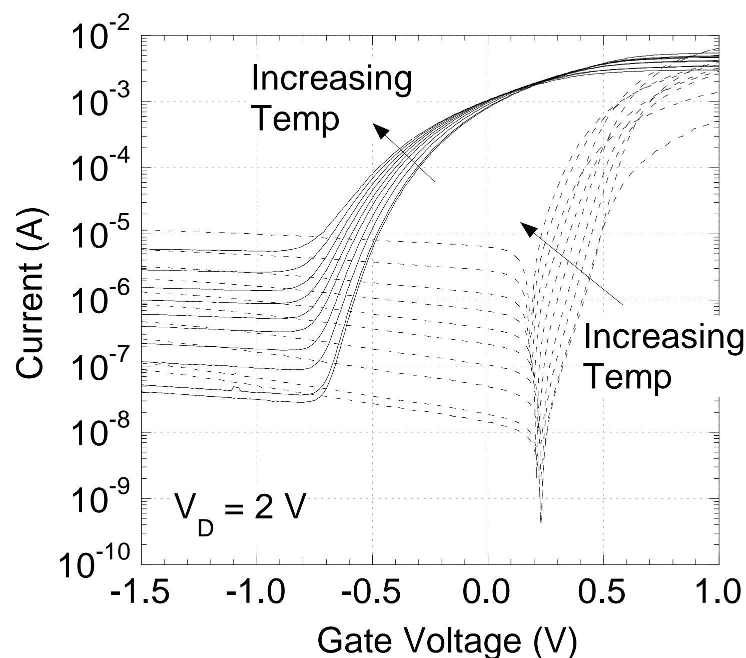

Fig. 7. The Gummel plot shows the changes in DC operation for a 100 μm device with $L_g = L_{aS} = L_{aD}$ = 0.6 μm between -60 to 150 ˚C. From -50 to 150 ˚C the temperature steps in 25 ˚C increments. The solid lines are I_D while the dotted lines are the magnitude of I_G. The device is from a 350 nm SOI CMOS process.

The limiting factor for the MESFET PTAT is the increasing gate leakage current, I_G, with respect to temperature. This is evident in Fig. 7 and in Equation 1.5. To minimize power consumption, the MESFETs in the PTAT should be biased at a drain current slightly above the gate leakage current at the highest

rated temperature. From Equation 1.5 it can be seen that the gate leakage current scales with the transistor's size so it can be reduced with smaller transistors. Unfortunately for the pass transistor of the LDO this means the gate leakage will be several magnitudes larger and can become very appreciable at high temperatures.

$$I_G \approx AA^*T^2 e^{\frac{-\phi_B}{U_T}} e^{\frac{V_{GS}}{nU_T}} \tag{1.5}$$

where

A = conducting area

A^* = Richardson constant

T = temperature

Φ_B = Schottky barrier

In [12], a relatively crude MESFET PTAT (Fig. 8) was built with the L_g = 0.6 and 1.2 µm devices from Fig. 6 to prove this concept. The two devices were both discrete and were wire-bonded to a single 16-pin DIP (dual in-line pin) socket. A circuit board was then designed with an off-the-shelf error amplifier to complete the design. Even with this simplistic design, the MESFET PTAT had a drift of only 11 ppm/^{o}C from 25 to 100°C when the bias current was set to 30 µA. While that would be unacceptable for a lot of applications, particularly because of the current consumption, the room for improvement is large. By integrating the two MESFETs together along with the error amplifier, needless resistance from the bond pads, wire bonds, and various wire connections which all have their own

temperature coefficient will go away. Furthermore, the two devices can be optimally sized and ratio-ed to lower the leakage current and so they both can operate at the same point on the drain curve to lower variation.

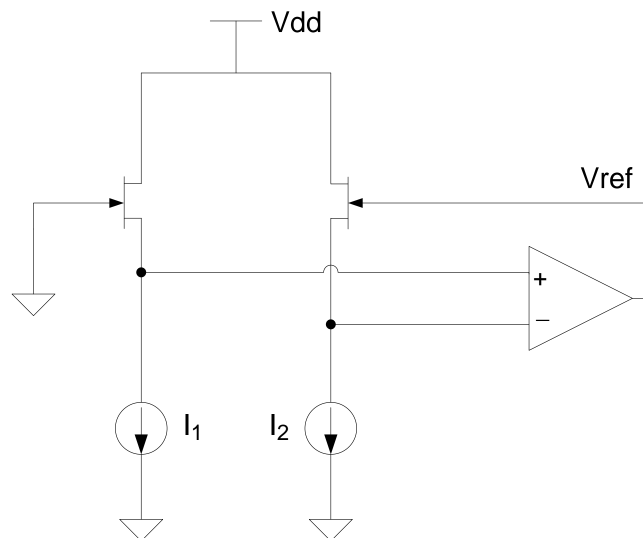

Fig. 8. Structure of the MESFET PTAT used in [12].

For an LDO, a voltage reference is an absolutely necessary building block and is needed for setting the output voltage. In the case of the fully integrated FD-MESFET LDO presented in Chapter 4, an all CMOS BGR was used since it was far less risky. Often manufacturers will alter process parameters from run-to-run to enhance the CMOS operation, but they do not always release that information for proprietary reasons. Without knowing these changes, variations in the MESFET operation can occur which makes designing a high precision reference difficult. Also the LDO's targeted output voltage, 2 V, and maximum input supply voltage, 3 V, were below the CMOS breakdown. Nevertheless, if a high voltage LDO is desired, an all or mostly all MESFET LDO can be designed.

1.5. Tradeoff Between Breakdown Voltage and Transconductance Gain

For most applications the biggest selling point of these MESFETs is they offer a cost free way to increase the operating voltage of the process beyond the capability of the CMOS transistors. From Fig. 9, it can be seen that MESFETs on a 350 nm and 3.3 V SOI CMOS process were able to obtain breakdown voltages in excess of 50 V. For the most part, this large breakdown voltage derives from the sizing of the access regions. The function of the access regions is similar to the drift region in a laterally depleted (LD) MOSFET which is to decrease the electric fields between the drain-gate and source-gate junctions [1]. Since the electric fields are disproportionate at the two junctions under most operating conditions, the access regions do not need to be or should not be sized the same unless L_{aS} and L_{aD} are sized at the minimum SB width. Increasing the access regions beyond what is needed for a given operating voltage only serves to degrade the performance of the device with respect to its transconductance gain, g_m, and peak cutoff frequency, f_T. The reason being is the access regions act like parasitic resistors in series with the channel and increase proportionately with size.

The critical access length is L_{aD} since the drain-gate junction becomes more strongly reverse biased as the drain voltage increases resulting in a higher electric field. As will be explained in detail in *Section 2.4*, there does appear to be a critical size for which L_{aS} needs to be to achieve high breakdowns, but after which it contributes very little to the overall breakdown. Similarly there exists a

certain L_{aD} where further gains in breakdown become negligible and the costs in terms of layout size and degradation in performance become prohibitive. For the 350 nm SOI CMOS process this L_{aD} is probably between 4 and 6 µm (Fig. 9). It is hard to determine the exact length since the only lengths fabricated with $L_{aD} > 2$ µm were 5, 10, and 15 µm.

The degradation from sizing L_{aS} is quite evident in Fig. 10 for the two devices with the L_{aD} of 10 µm. The peak transconductance decreases from ~27 mS/mm to ~9.2 mS/mm as L_{aS} increases from 2.2 to 10 µm even though both devices will have approximately the same breakdown. In contrast, if L_{aS} remains at 2.2 µm and just L_{aD} increases from 2.2 µm to 10 µm the peak transconductance will reduce only from ~32.4 mS/mm to 27 mS/mm, but the breakdown voltage increases from 38.5 to 52.4 V. The disproportionate effects of L_{aS} and L_{aD} can be attributed to L_{aS} also acting as a source degeneration resistor.

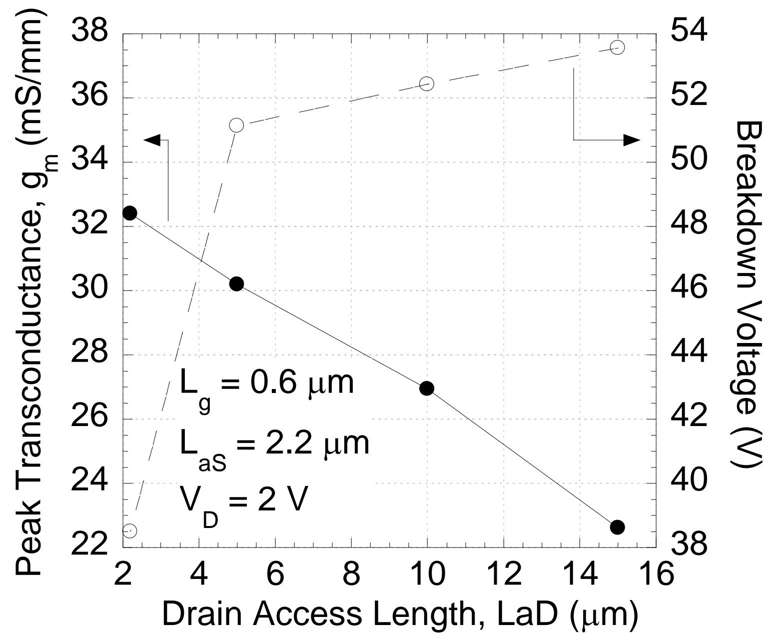

Fig. 9. The tradeoff of peak transconductance and breakdown voltage is shown as a function of L_{aD}. Devices are from a 350 nm SOI CMOS process.

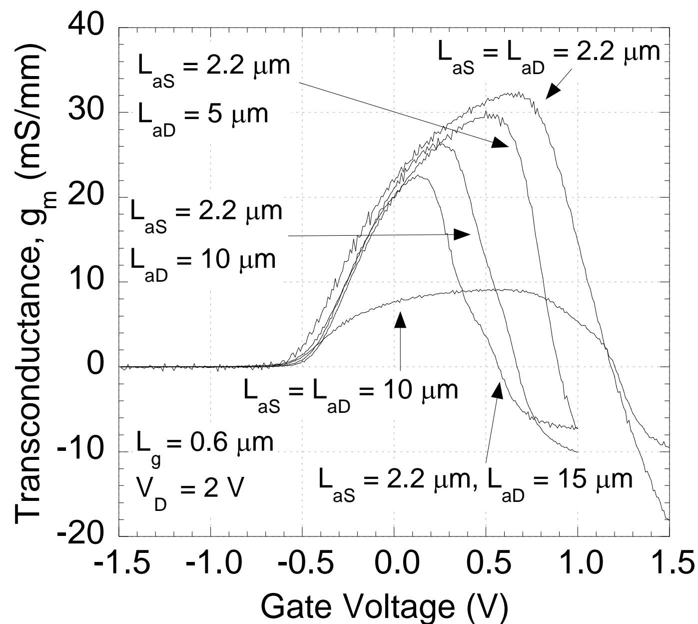

Fig. 10. The transconductance of the device is greatly affected by L_{aS}. The degregation in transconductance can be minimized by appropriately sizing L_{aS}. Devices are from a 350 nm SOI CMOS process.

1.6. CONCLUSION

As it was shown in this chapter, one of the main advantages of the MESFET is its ease to tailor it to different applications by appropriately sizing L_{aD}, L_{aS}, and L_g. The discussion and measured results were limited to only n-MESFETs, however, p-MESFETs can be fabricated in an analogous way to Fig. 2. In general though, the p-MESFETs that have been fabricated have suffered from higher gate leakage current and lower current drive, but having the availability of p-MESFETs makes these SOI and SOS MESFETs unique to GaAs MESFETs [19-20]. Hopefully with future research and subsequent fabrication runs ideal complementary transistor operation can be obtained. Nevertheless, the focus for this thesis will remain on optimizing n-MESFETs since p-MESFETs are not encompassed in the LDOs presented in Chapters 4 and 5.

CHAPTER 2

SCALING PD-SOI MESFETs

PD-MESFET demonstrations have been made with SOI technologies at the 600 nm [3] and 350 nm CMOS technology nodes [1]. This chapter presents the latest measured data taken from MESFETs fabricated using a 150 nm PD-SOI CMOS process from Honeywell. These devices represent the most aggressively scaled and highest performing Si-MESFETs to date with gate lengths as short as 150 nm. Where it is applicable, the results are compared to those from devices fabricated using the earlier 350 nm technology node which was also done at the same foundry. Since MESFETs will undoubtedly scale at a different rate than the MOSFETs due to the differences in device structure and layout layers used, this comparison provides a statistical based insight into the MESFET's performance improvement from one technology node to the next and sets possible future exceptions for Si-based MESFETs.

2.1. Optimizing FD-MESFET Layout

Like a CMOS transistor, the RF performance and current drive capability of a MESFET is highly dependent on the minimum gate length that can be achieved. In addition to the design rule that dictates the minimum spacing of the patterned silicide block layers, other possible limiting factors on gate length are as follows: the size of the contact layer which contacts the silicide layer at the gate to Metal 1 (first level of metal in the process), the required Metal 1 overlap of the contact, and the spacing between the contact layer and the spacer (Fig. 11).

Fortunately, the limitations imposed by these backend of line (BEOL) design rule constraints can be overcome by moving the gate contact outside the access regions. This is made possible by the PD-MESFET's continuous gate structure (Fig. 12) and is a critical layout tactic needed to achieve high performance MESFETs. It becomes particularly important in processes with large BEOL design rules.

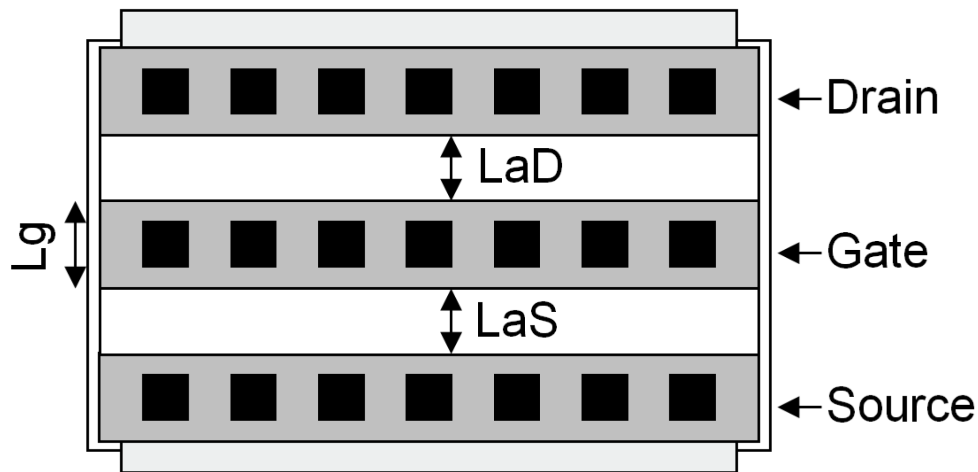

Fig. 11. Top-view of PD-MESFET layout with the gate contacted inside the access region (silicide block is used to create the SiO_2 spacers).

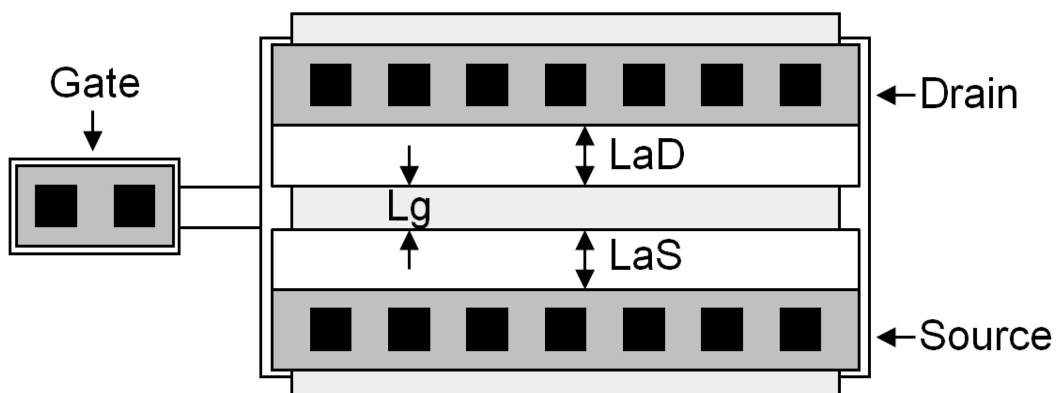

Fig. 12. Top-view of PD-MESFET layout with the gate contacted outside the access region to reduce L_g (silicide block is used to create the SiO_2 spacers).

BEOL rules, nevertheless, will still have an effect on the length of the drain and source lines which will consequently affect the MESFET in the form of current drive per area. The drain current per finger will roughly be the same no matter what the BEOLs are since it is mostly dictated by gate length (assuming the structure in Fig. 12 is used), but the length of the drain and source lines will affect how many fingers can fit into a given die area. This impact will be relatively small for applications using small width MESFETs, for example < 1 mm, but for an application such as the pass transistor of an LDO which can easily use MESFETs of several thousand fingers, the BEOLs rules can positively or negatively affect the LDO's commercial practicality. This subject will be further discussed in much more detail in Chapters 4 and 5.

It is expected, however, that the device in Fig. 12 will have a higher noise figure than the one in Fig. 11 due to it having a more resistive gate which is caused by the elongated gate finger, fewer gate contacts, and the contacts being placed at edge of the device. Thus in general, if the MESFET is going to be used in a low-noise application, Fig. 11 would probably be a more advisable layout option. In the 150 nm process, the drastic reduction in contact size and other BEOL rules allows for Fig. 11 to be used without significantly increasing the gate length. From Table 1, that was clearly not the case for the 350 nm process whose minimum L_g would be 1.1 μm with the layout structure in Fig. 11. In that process, even with the noise penalty of Fig. 12, the gains in current drive and RF performance make Fig. 12 clearly more advantageous.

In the 150 nm process, the layout structure was slightly altered from the typical PD-MESFET approach for the most aggressively scaled devices. Instead of creating the access regions with silicide block which has a minimum width of 0.6 μm (refer to Fig. 11 and Fig. 12 structures), a body-tie (BT) approach developed by Honeywell engineers was used. The BT-MESFET, shown in Fig. 13, surrounds the device with a body-tie. In regions where there is active silicon, it is silicided. Elsewhere, the process etches the silicon above the buried oxide down to about 45 nm and fills it with deposited oxide (Fig. 14). Therefore the BT over non-active silicon areas, in effect, acts similarly to the function of the silicide block; however, the rules that control the minimum separation and width of active silicon are much more controlled in this process allowing for much smaller values for L_{aS}, L_{aD}, and L_g. In fact, using this method allows for gate lengths as low as 150 nm and access lengths as small as 260 nm. The improvements between the two structures are shown in Table 2. As was the case with SB-MESFETs, the gate can be contacted both inside (not shown) and outside (Fig. 13) the oxide spacers for BT-MESFETs. If the equivalent structure to Fig. 11 is used then the minimum gate length becomes 340 nm.

Table 1: Scaling of Key Layout Rules for SB-MESFETs

Specification	*350 nm SOI CMOS*	*150 nm SOI CMOS*
Contact Size	300 x 300 nm	170 x 170 nm
M1 Overlap of Contact	225 nm	90 nm
Spacing of Contact and SB	400 nm	180 nm
Minimum L_g (Fig. 11)	1.1 µm	530 nm
Minimum L_g (Fig. 12)	400 nm	400 nm
Minimum L_{aS} & L_{aD}	600 nm	600 nm

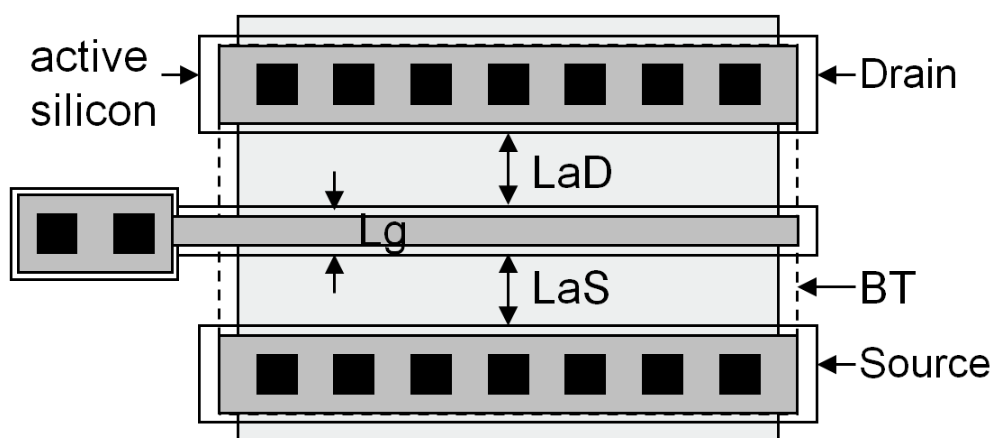

Fig. 13. Top-view of the BT PD-MESFET layout with the gate contacted outside the access region to reduce L_g.

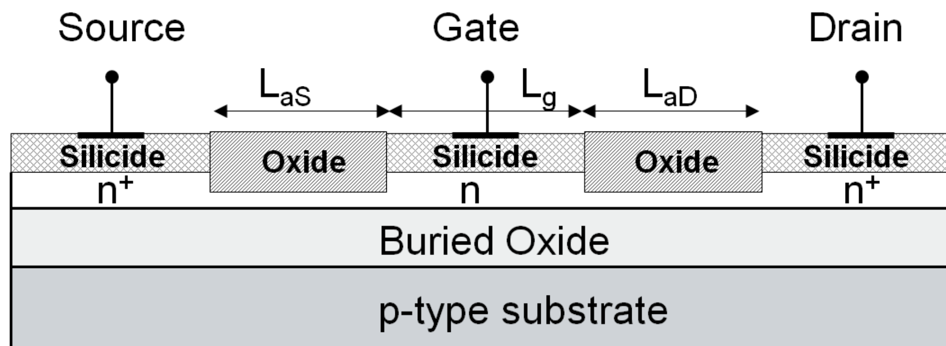

Fig. 14. Cross-sectional view of a PD-MESFET structure which uses the body-tie method to create oxide spacers.

Table 2: Comparison of SB and BT-MESFETs in the 150 nm SOI CMOS Process

Specification	*SB-MESFET*	*BT-MESFET*
Minimum L_g (Gate Outside Spacers)	400 nm	150 nm
Minimum L_g (Gate Inside Spacers)	530 nm	340 nm
Minimum L_{aS} & L_{aD}	600 nm	260 nm

2.2. *DC Characterization*

The Gummel plots in Fig. 15a-b show the drain and gate current (magnitude) for the most aggressively sized devices in both the 150 nm and 350 nm processes. As expected, significantly higher drain currents are possible on the 150 nm process as a result of the smaller achievable gate lengths. The L_g = 150 nm device, for example, shows excellent current drive, about 3x larger (at V_D = 2 V and V_{GS} = 0 V) then the highest current device from the 350 nm process (L_g = 400 nm), but it exhibits weak gate control and is very hard to turn off. Accordingly, its use in most circuit applications would probably be limited. Just

to note, each of the devices from Fig. 15 used the layout structure shown in Fig. 12 so that the performance of the devices with the same architecture could be compared.

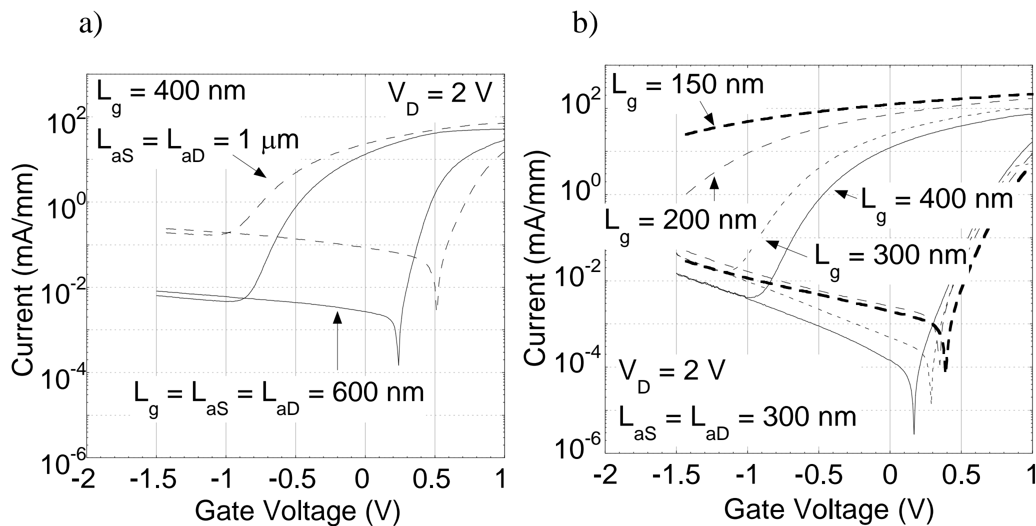

Fig. 15. Gummel plots for the smallest gate lengths fabricated on each process: a) 350 nm SOI CMOS and b) 150 nm SOI CMOS.

Interestingly, when the two devices in Fig. 15 with gate lengths of 400 nm are compared, the device on the 150 nm process has a noticebly smaller drain current. This might be particularly suprising since the device on the 150 nm has smaller access lengths which corresponds to a smaller parastic resistance in each access region. That should correlate in theory to a higher drain current; however, it does not account for threshold voltage difference in the two devices. The threshold of the device on the 350 nm process is more negative which allows the device to be turned on harder and have a higher drain current. Nevertheless, the current drive per die area will be significantly higher on the newer process due to the scaled BEOL rules and access legnths.

From Fig. 15b its evident that the most aggressively sized gate lengths on the 150 nm process were heavily affected by short channel effects. The gate length at which SCE ceases to be an issue becomes clearer in Fig. 16 which extracts the threshold voltage, V_t, for each of the MESFETs in Fig. 15a-b. From the figure we conclude that gate lengths ≥ 400 nm are required to avoid SCE altogether in the 150 nm technology, while $L_g \geq 600$ nm is required for the 350 nm process. Presumably, the SOI channel in the 150 nm technology is thinner and more heavily doped than in the older 350 nm technology allowing the 150 nm node MESFETs to be scaled to shorter gate lengths before SCE become significant. This observation is consistent with the threshold voltage model developed by Chiang *et al.* for short-channel SOI MESFETs [21] which shows the SCE becoming apparent as the gate length approaches the thickness of the silicon channel [9]. Based on measured results from five different commercial CMOS foundries [1-3], our MESFETs usually see SCE starting at 1.5 – 2x the minimum feature size of the process. It will vary slightly on different processes due to channel thickness, doping densities and the silicide step which consumes a portion of the silicon channel. By interpolating the data in Fig. 16, a MESFET with a gate length of 250 nm fabricated using the 150 nm node would have a threshold voltage of approximately -1 V and represents a good trade-off between high speed performance and practical depletion mode operation.

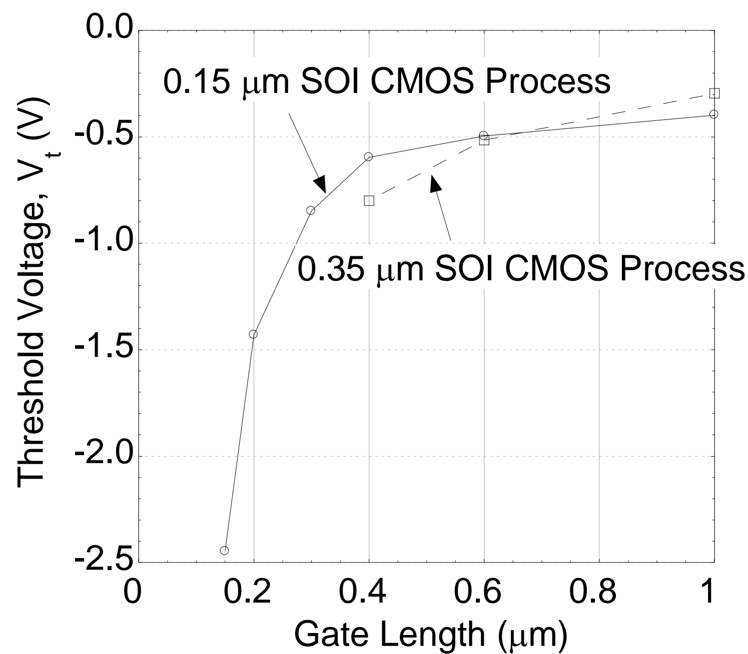

Fig. 16**.** Threshold voltage extracted for each of the devices plotted in Fig. 15a-b.

Pronounced SCE are also apparent in the family of curves plots in Fig. 17a-d. The slope of the drain current curves for the L_g = 150 nm MESFET in the saturation region is indicative of a device with low output resistance. Also, the requirement of a large drain voltage, ~2 V, before it reaches saturation suggests that it has a large negative threshold which is consistent with the data in Fig. 16. Fig. 18 plots the extracted output resistances of the devices considered in Fig. 17. Again it appears that an ideal gate length is probably between 200 and 300 nm.

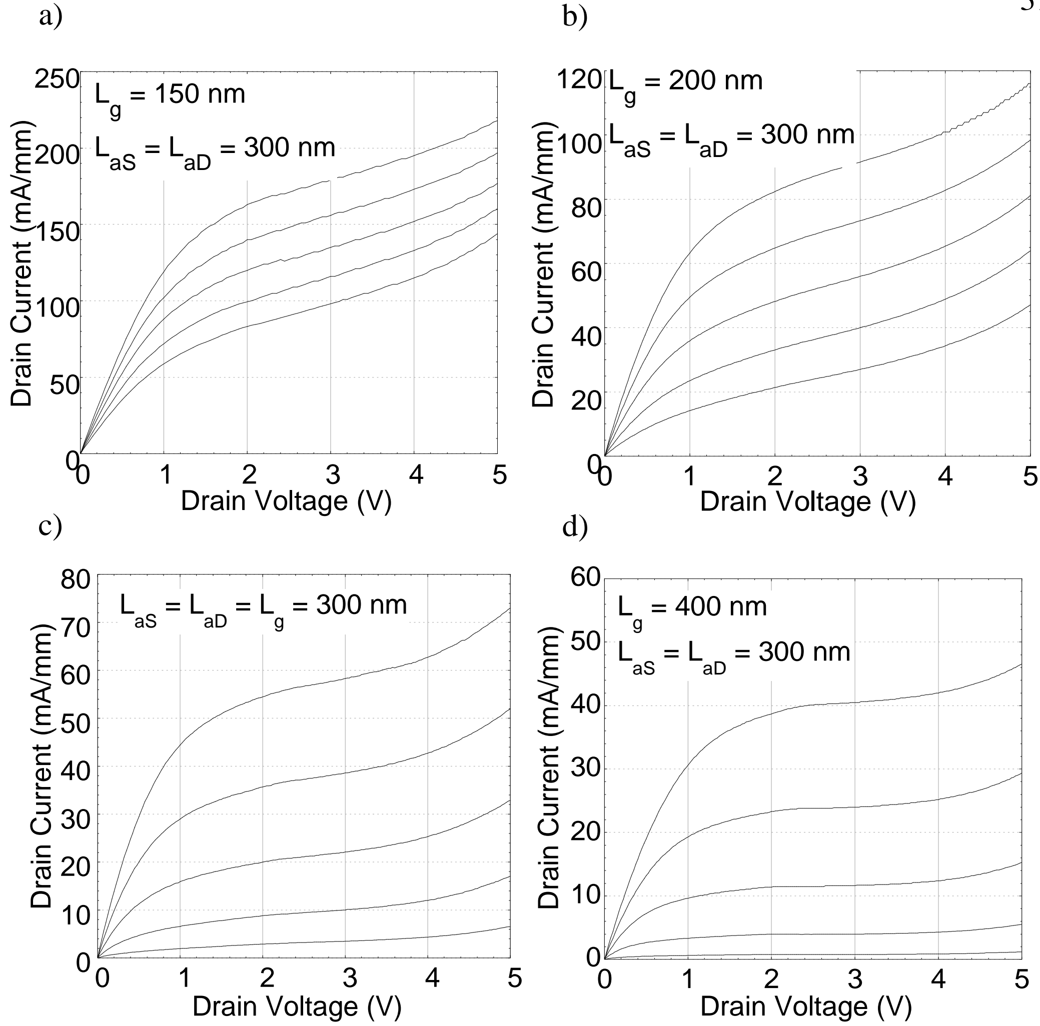

Fig. 17a-d). Measured family of curve plots corresponding to the four devices shown in Fig. 15b. In each graph the gate voltage is stepped from +0.5 V (uppermost curve) to -0.5 V in 0.25 V steps.

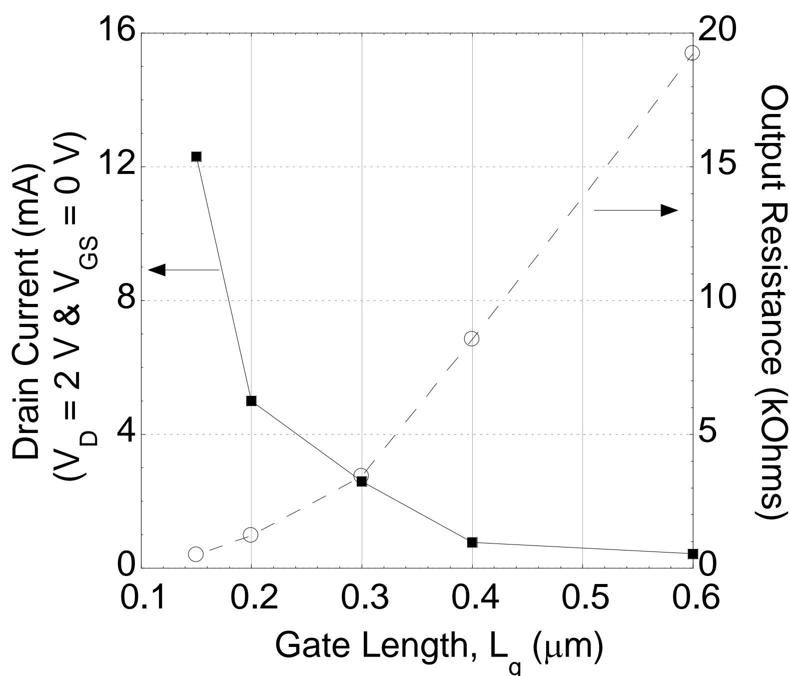

Fig. 18. Exhibits the trade-off in current drive and output resistance for the MESFETs in Fig. 17a-d.

2.3. *RF Characterization*

RF characterization was performed by on-wafer probing using select devices with ground-signal-ground (GSG) pad configurations (Fig. 19). Also included on the die was an accompanying set of open- and short-circuit test structures to de-embed the devices and remove the parasitics of the GSG pads. Measurements were taken by an Agilent 8510C vector network analyzer and a HP 8515a S-parameter test set. From the de-embedded S-parameters, WinCal [22] was used to extract the f_T of the MESFETs which was defined as the point where the current gain, $|h_{21}|^2$, equaled 0dB. Since the Agilent 8510C only had a measuring range of 0.45 – 20.3 GHz, devices with $|h_{21}|^2 > 0$ dB at 20.3 GHz had

to be carefully extrapolated to determine the f_T.

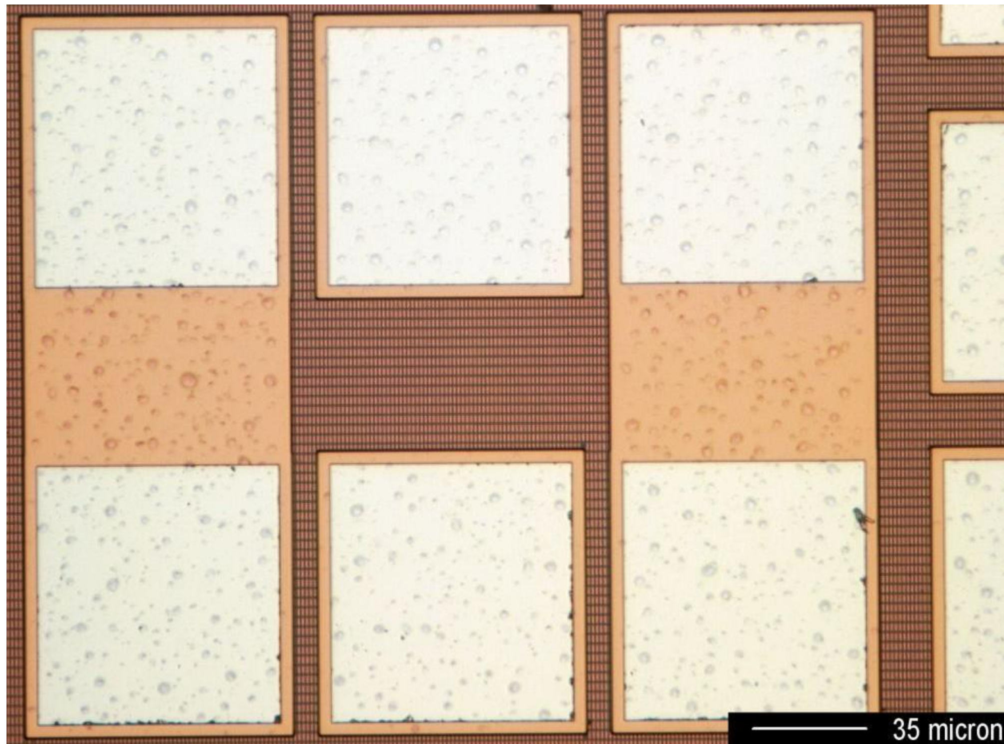

Fig. 19. The GSG structure used for RF characterization in the 150 nm process.

From a circuit perspective, L_{aS} and L_{aD} appear as parasitic resistors in series with the channel of the MESFET [23]. Fig. 20 shows the roll-off in peak transconductance gain, g_m, for a set of devices with L_g = 200 nm and L_{aS} = 300 nm as L_{aD} increases from 300 nm to 1 μm. It underlines the importance of appropriately sizing L_{aS} and L_{aD} and that overdesigning the MESFET for one specification can limit it in several others. As will be discussed in *Section 2.4*, all three devices in Fig. 20 will have a breakdown that is approximately the same due to L_{aS} being 300 nm. Therefore there is no reason not to size L_{aD} 300 nm. If the breakdown of these devices is insufficient for a particular application, L_{aS} should

be sized to the critical length discussed in *Section 2.4* and L_{aD} should be sized accordingly.

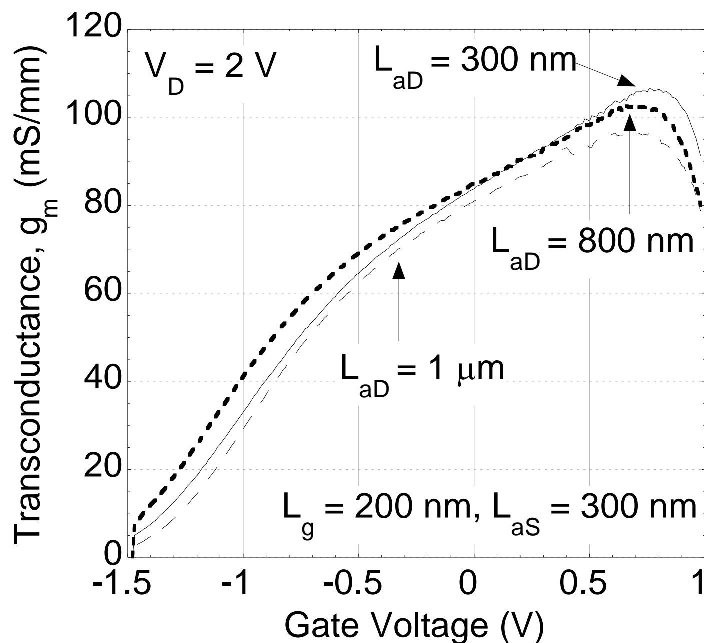

Fig. 20. Shows the roll-off in transconductance gain as L_{aD} increases from 300 nm to 1 μm on the 150 nm SOI CMOS process.

The cut-off frequencies of the devices in Fig. 15a-b are shown in Fig. 21. This figure also includes a device with L_g = 1.2 μm and L_{aS} = L_{aD} = 1 μm manufactured on the 350 nm process to show the trend in f_T for the 350 nm devices. It is encouraging that the exponential scaling with respect to gate length holds in each process. This bodes well for the next technology node. The main improvements can be traced to the reduction in the parasitic resistance of the access regions due to the scaling of L_{aD} and L_{aS} and the reduction of parasitic capacitance contributed by reduced size of the BEOL dimensions at the drain and source. It is clear from Fig. 21 that there is a ~3x increase in the corresponding f_T values for the MESFETs with L_g = 400 and 600 nm manufactured using the 150

nm process. The reduction in parasitics is evident in Fig. 22 which compares the f_T of a device from both processes with the same L_g, L_{aD}, and L_{aS}.

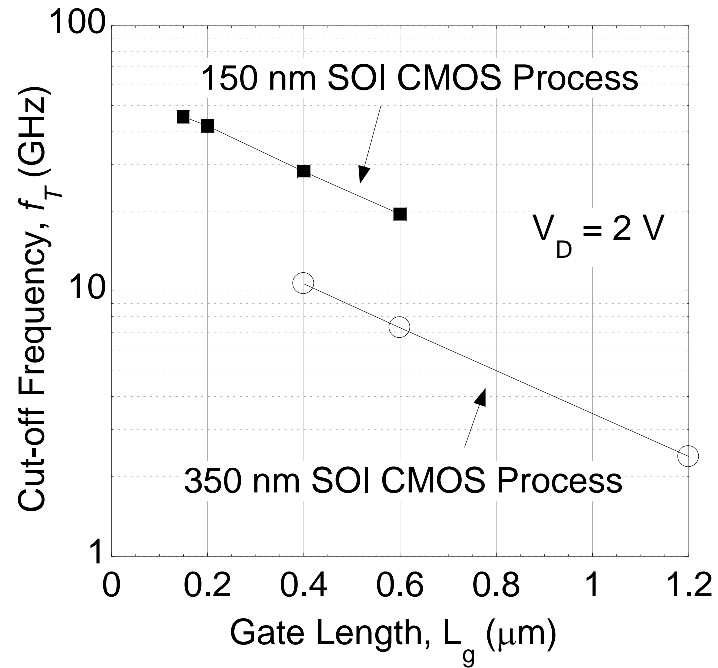

Fig. 21. Shows the exponential scaling of the peak cut-off frequencies for MESFETs manufactured on 150 and 350 nm SOI CMOS processes.

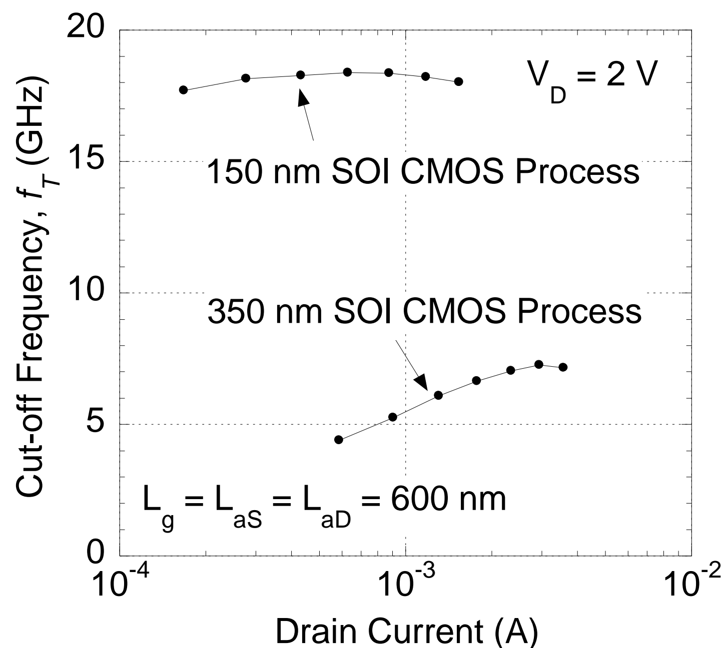

Fig. 22. A comparison of the f_T dependence on drain current for two MESFETs with nominally identical dimensions but fabricated using different SOI CMOS technology nodes.

Fig. 23 displays the f_T versus drain current for three devices that best summarize the range of performance on the 150 nm process. The L_g = 150 nm and $L_{aS} = L_{aD}$ = 260 nm MESFET represents the highest measured f_T device on the die. The L_g = 200 nm and $L_{aS} = L_{aD}$ = 300 nm MESFET has a lower f_T, but as it was shown in Fig. 15-Fig. 18, it balances the SCE shortcomings of the L_g = 150 nm device and still maintains a relatively high current drive. An argument could be made for the L_g = 300 nm device from Fig. 15b but it was not included with a GSG structure and could not be characterized in the RF domain. Based on an interpolation from Fig. 21, the f_T is estimated to be ~35 GHz. Lastly, the L_g = 400 nm MESFET was included to show a device that nicely balances high breakdown (~11 V) with peak f_T.

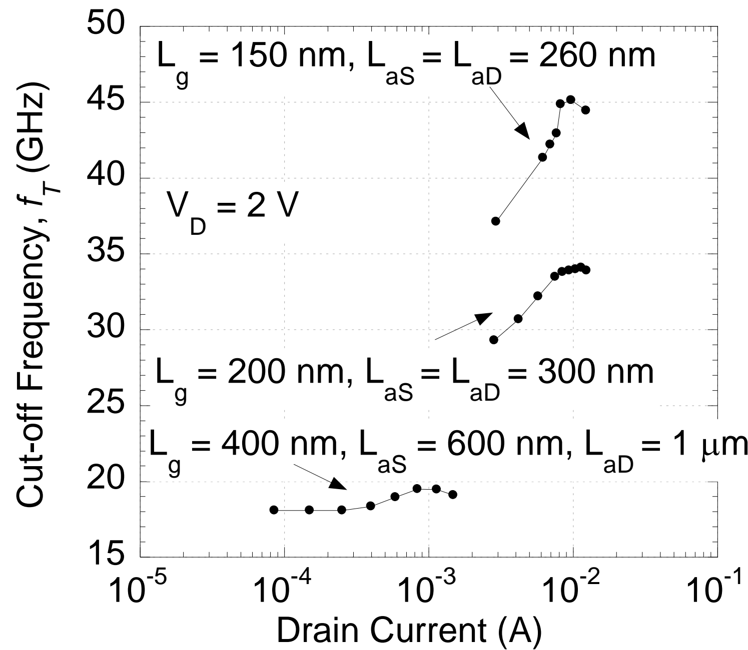

Fig. 23. Shows the cut-off frequencies versus drain current for select devices on the 150 nm SOI CMOS process.

2.4. *MESFET BREAKDOWN*

MESFETs naturally have a high breakdown ability due to their non-self aligned structure and Schottky gate which can tolerate high current flow. Furthermore, without a fragile thin gate oxide, MESFETs do not have some of the breakdown mechanisms seen in MOSFETs such as the electric field gate oxide breakdown and snapback. Breakdown in the MESFET is thought to be caused mostly by avalanche ionization and tunneling mechanisms. As the MESFET approaches soft breakdown, the surface electric field can become large enough to lower the barrier height at the gate and allow electrons to tunnel into the channel from the gate metal. Consequently this leads to an exponential increase in drain-

to-gate current [24]. If the drain voltage is further increased and/or the gate becomes more negatively biased the electric field will become even larger and avalanche ionization will begin to occur. Eventually this will lead to a non-reversible hard breakdown for the MESFET.

To be consistent with the breakdown measurements reported in [1] the drain-current-injection technique [25] was used to quantify the breakdown voltage of the MESFET. Once again, the biasing metric of 1 mA/mm was used as the constant current source forced into the drain. Since each MESFET presented in this chapter has a width of 100 μm this results in a drain biasing of 100 μA. Under these bias conditions the peak measured breakdown on the 150 nm process is ~12 V, as shown in Fig. 24. This is considerably lower than the ~55 V [1] achieved on the 350 nm process. As a reference, the maximum steady-state operating voltage of the CMOS devices is 1.95 V for the 150 nm technology and 3.5 V for the 350 nm technology.

The key factor in this variance probably lies in the difference in the doping densities of the two processes. While the exact doping profile is unknown in either process, it can be assumed that the 150 nm process had a higher doping level to combat the expected increase in short channel effects for a more scaled process. This would increase the electric field and enchance the avalanche phemonenon. Consequently, the devices would breakdown at a lower voltage. Secondly, the increased doping would reduce the depletion region at the n/n^+ junction between the gate and drain. That in turn would reduce the significance of

increasing L_{aD} which helps reduce the electric field at that junction and increase the point at which the device breaks down. In any process though, L_{aD} can only be increased so much before it no longer has an effect. In the 350 nm technology this roll-off occurs around L_{aD} = 5 μm [1] compared to the L_{aD} ~1 μm in the 150 nm process. Without the positive impact of L_{aD} beyond 1 μm, the 150 nm process cannot be expected to reach breakdown voltages anywhere close to the 350 nm process. For devices with $L_{aD} \leq 1$ μm it is expected that the breakdown voltage would only be moderately reduced by the higher doping. This is exactly what was observed in the measured results. Case in point, the MESFET with $L_g = L_{aS} = L_{aD}$ = 600 nm is ~8 V in the 150 nm process which is only a 4 V reduction from the 350 nm process [1].

It had been suggested in previous works [1-2] that the breakdown event happened almost exclusively at the drain end and was independent of the access region at the source side. Clearly this is not the case as shown in Fig. 24. The breakdown is about twice as large with L_{aS} = 600 nm as compared to L_{aS} = 300 nm for L_g = 600 nm and $L_{aD} > 1$ μm. Furthermore, for devices with L_{aS} = 300 nm the breakdown is essentially independent of L_{aD}. This suggests that there is another form of breakdown happening on the source side. Presumably the breakdown event is not the result of tunneling/avalanche breakdown since the electric field should be significantly lower as a result of the much smaller reverse biasing at that junction. In the worst case scenario the reverse bias would not exceed 1 to 1.5 V, whereas, on the drain side it will be 3.5 to 6 V. Thus, there

must be a critical length for L_{aS} greater than 300 nm, but less than 600 nm on the 150 nm process in which this new breakdown is no longer an issue. This issue was previously unseen before in other process runs since the lithography rules prevented the width of the spacers from being reduced below 600 nm. Since there are no devices with L_{aS} other than 260, 300 and 600 nm there is insufficient data to confirm this assumption.

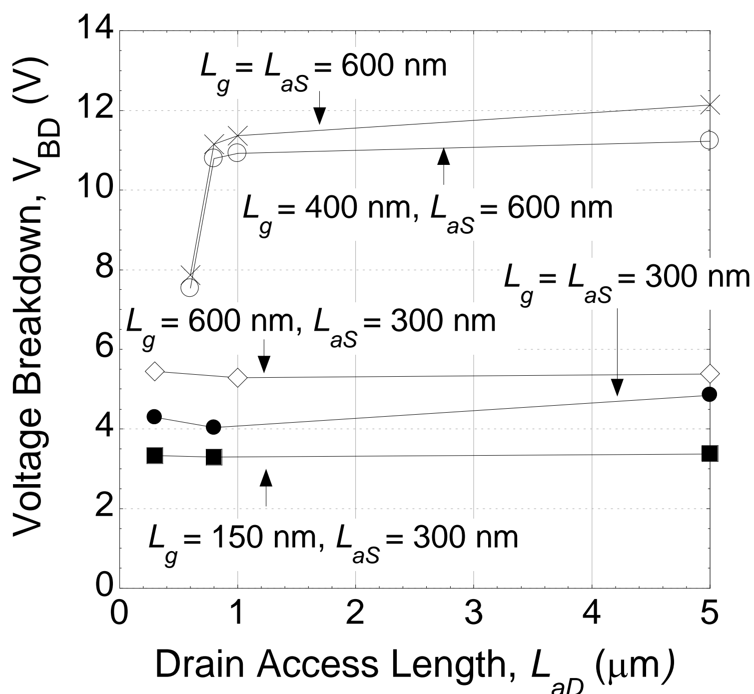

Fig. 24. Shows the breakdown voltage of various MESFET structures on the 150 nm SOI CMOS process.

To demonstrate the trade-off between current drive, breakdown voltage and RF performance we plot the family of curves for drain voltages up to 10 V for a device with L_g = 400 nm, L_{aS} = 600 nm and L_{aD} =1.0 μm in Fig. 25. This device is similar to the one used for Fig. 17d but the longer L_{aS} and L_{aD} gives it a higher breakdown voltage of ~11.5 V. Although the device has soft output saturation at

the higher gate voltages it shows good output characteristics up to 10 V when operated in depletion mode. The drive current is reduced compared to Fig. 17d, but with a peak f_T close to 20 GHz (see Fig. 23) the data in Fig. 24 demonstrates the enhanced voltage capability for GHz switching applications.

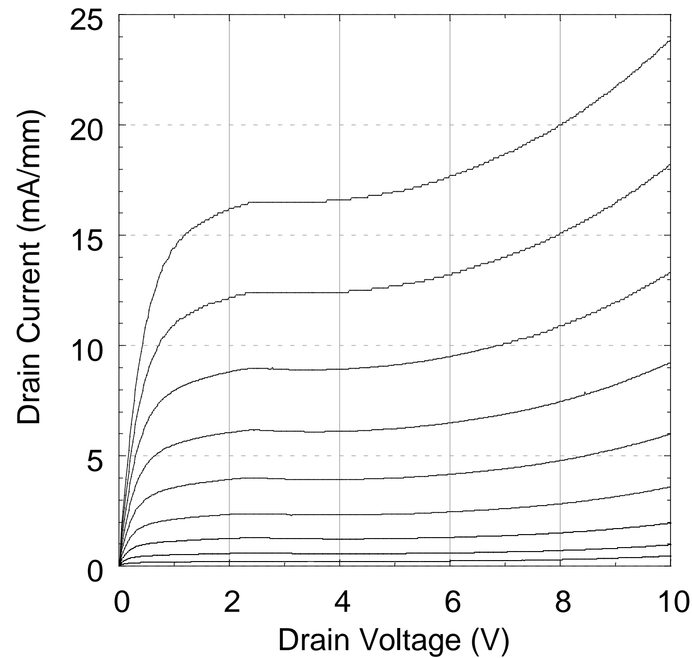

Fig. 25. The family of curves for a MESFET with L_g = 400 nm, L_{aS} = 600 nm and L_{aD} = 1 µm. The gate voltage is stepped from +0.4 V (uppermost curve) to -0.4 V in 0.1 V steps.

2.5. *Conclusion*

The tightening of design rules with respect to the patterned silicide layers in the 150 nm process, as well as the other rules highlighted in Table 1 and Table 2, led to significantly higher performing and more compact SOI MESFET devices than have been reported earlier. Encouragingly, devices in each process showed an exponential scaling of f_T with respect to the gate length leading to the belief

that > 100 GHz MESFETs might be possible at the next technology node. However it was shown that as MESFET gate lengths approach the limit of the technology node they become strongly affected by short channel effects. Thus the the future of MESFET scaling will depend largely on how the the width of the spacers and BEOL rules scale. If they continue to scale well, very high f_T MESFETs could be achieved with slightly larger gate lengths, mitigating some of the short channel effects. Granted, decreasing L_{aS} or L_{aD} will lower the breakdown voltage, but it is expected that these devices will nevertheless have breakdown voltages significantly higher than MOSFETs on the same process. Taking into account all the various metrics for DC and RF performance, the best all around device on this 150 nm process run would probably feature a gate length in the range of 200-300 nm.

Before declaring that, it is important to note there was a second fabrication run on the 150 nm process in which the focus was designing a very large MEFSET device for an LDO application (further details and measurements from that device are discussed in Chapter 5). Additionally a few other MESFETs including BT-MESFETs with gate lengths of 250 and 300 nm and widths of 100 μm were added to monitor the run-to-run variations as well as to figure out the optimum gate length. Unbeknowst to us at the time of the second fabrication, Honeywell changed the silicide step to be slightly thinner in an effort to enhance the performance of the MOSFETs. Consequently the thin silicon layer above the buried oxide was left about 20 nm thicker and resulted in a negative shift in the

threshold voltage; as seen in Fig. 26. This change can be expected since a larger negative voltage should now be needed at the gate-source junction to pinch off the thicker channel. If Honeywell decides to keep the thinner silicide step for this process, which it does appear to, then the ideal gate length for the MESFETs to avoid excessive short channel effects while maintaining high performance will be about 300 nm.

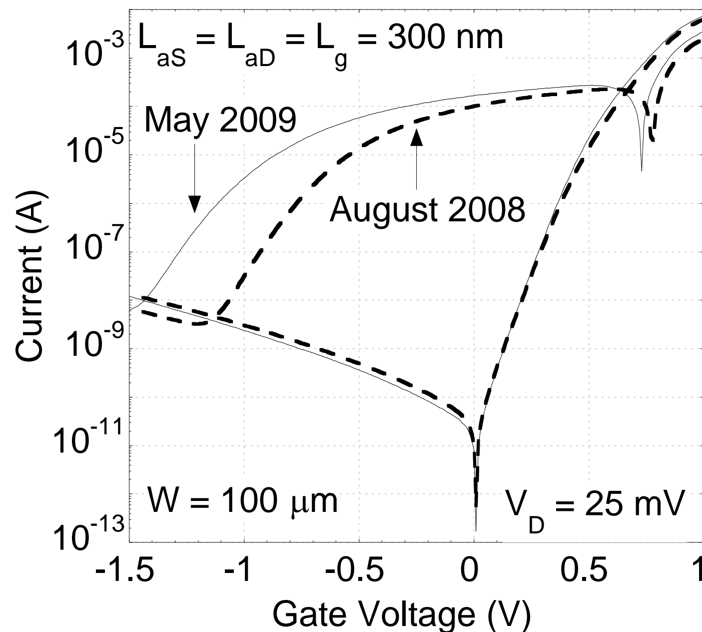

Fig. 26. Comparison of Gummel plots for nominally identical L_g = 300 nm devices fabricated on the 150 nm process in August 2008 and May 2009.

CHAPTER 3

FD-SOI & SOS MESFETS

While FD-SOI CMOS products are in the minority compared to those in traditional bulk or PD-CMOS processes it is used in many current applications due to its superior low power capability. In the future though, it is almost a certainty that FD-CMOS will gain in popularity since the thin silicon above the insulator has been trending downwards with each progressive process node. This scaling might ultimately lead to FD-CMOS supplanting PD-CMOS as an option all together. Furthermore, it is also a certainty that a high voltage transistor will be needed on those processes if certain analog applications are to be incorporated since state-of-the-art processes already have breakdown voltages < 1 V. This chapter proposes high voltage FD-MESFETs with breakdown voltages > 17 V developed on commercial SOS and SOI CMOS processes aimed to fix this issue. Additionally it will highlight some of the fundamental differences in operation and layout from the PD-MESFETs.

3.1. FD-MESFET ARCHITECTURE

The FD-MESFET bases its basic design structure after the PD-MESFET and has a similar fabrication flow as Fig. 2. Like the PD-MESFET, the Schottky gate of the FD-MESFET is formed from the $CoSi_2$ silicide layer in a lightly doped n-well resulting in nearly ideal Schottky diode behavior. The key process step once again is the patterning of the silicide block layer to form SiO_2 spacers

between the contacts of the drain, gate, and source. Lastly, the critical access length is at the drain (L_{aD}) and is one the primary reasons for the MESFET's high breakdown capability.

The fundamental difference between the two types of MESFETs is how the gate is oriented to conduct current. For PD-MESFETs, the silicon layer above the insulator is 140-200 nm thick. In the creation of the Schottky gate, only about 30-100 nm of that silicon is consumed in the formation of the metal silicide. The remaining silicon under the gate is sufficient enough to form a channel directly under the gate. On the other hand, for FD-MESFETs the silicon layer above the insulator is 50 nm or less. Most of this is then consumed during the formation of the silicide. Any remaining silicon under the Schottky gate is too thin to form the channel of the MESFET even under enhancement conditions because the forward bias required to turn on the device would lead to excessive gate conduction. As a result, conduction of the drain current does not occur directly under the gate. Instead the layout is slightly altered, as depicted in Fig. 27 and Fig. 28, to confine the current between islands of silicide that deplete the conducting channel in the lateral direction. The definitions of L_{aS}, L_{aD}, and L_g remain the same as the PD-MESFET. The new parameter of channel width denoted as L_{CW} is introduced and is the distance between the silicide islands. It is patterned in the same manner as L_{aS} and L_{aD}. Generally speaking, the current drive of the device will increase with an increase in L_{CW} [26-27].

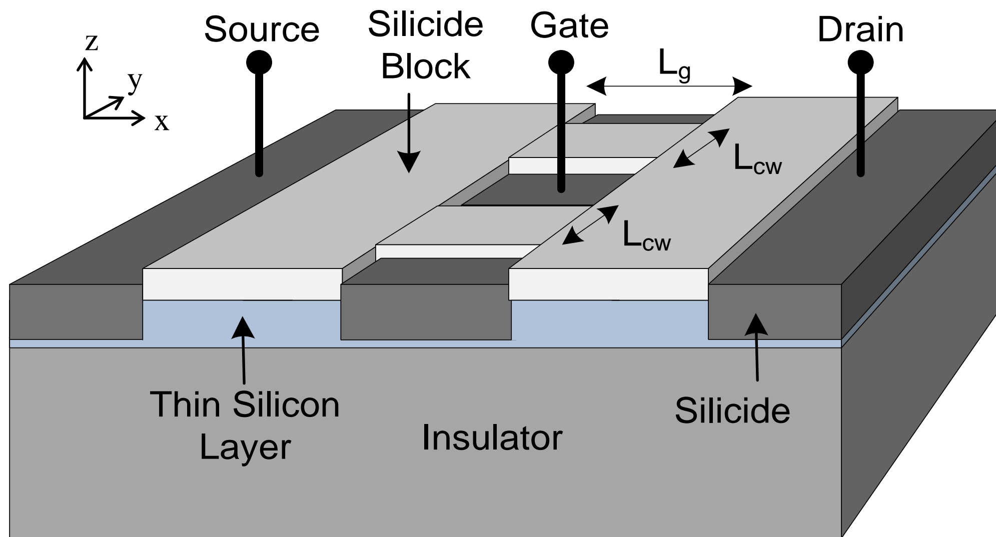

Fig. 27. 3-D rendering of the FD-SOI MESFET showing two conducting channels confined between islands of silicide. Electrical contact to each silicide island is provided by contacts to the first layer of metal interconnect (not shown) [27].

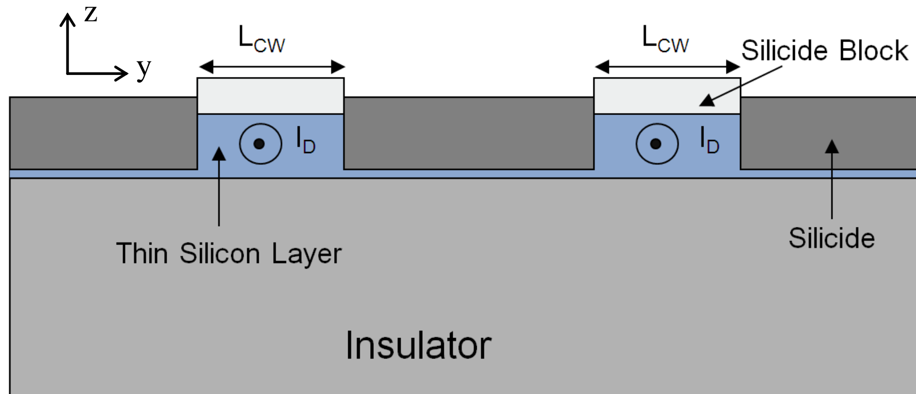

Fig. 28. Shows a cross-section in the y-z plane through the center of the device. The conducting channels are formed underneath the regions of silicide block. The current flows into the channels as indicated in the figure [27].

The FD-MESFETs were first fabricated on Peregrine's 0.25 µm SOS CMOS process and then on a 0.2 µm SOI CMOS process from MIT-Lincoln Labs (MIT-LL). Using the standard FD layout shown in Fig. 27, the minimum feature

sizes of the Peregrine technology limited the minimum channel lengths and widths to 1.8 µm and 0.25 µm respectively. The L_g limitation was the result of the large contact size as well as the spacing requirement between the contact and the silicide block layer. The PD-MESFET can overcome this layout limitation by simply adopting the Fig. 12 orientation and making the gate contact at the top and/or bottom of the device. In those devices the limitation then becomes the minimum separation of the silicide block. FD devices with multiple channels on a single finger conversely do not have a continuous gate. The gate between two adjacent channels is isolated from the gate between any other set of channels. Thus, a contact between each set of channels to a common metal line down the gate is needed for the gate to be at equal potential. Having multiple channels in a single finger is critical in minimizing the layout area and maximizing the current drive since each channel will only contribute a current in the few µA's range. Current per channel will be dependent on doping level, L_{CW}, L_g and other process parameters [26-27]. It is important to point out that the backend metals of the Peregrine process were that of a 0.6 µm process. If the Peregrine's backend metals were scaled to that of a typical 0.25 µm process the gate length using the Fig. 27 structure would no longer be limited by the contact size and contact to silicide block spacing but by the 1.2 µm minimum spacing of the silicide block.

MIT-LL's more stringent handle on process features allowed for gate lengths as small as 0.6 µm and channel widths of 0.2 µm with a layout similar to Fig. 27. The core objective for the SOS MESFETs was to gather an understanding

on the effects parameters such as doping concentration, L_{CW}, L_{aS}, and L_{aD} had on threshold voltage, leakage current, breakdown voltage, and current drive. On the ensuing run with MIT-LL, the most successful structures from the SOS MESFETs were then transferred over to equivalent SOI MESFET structures with smaller gate lengths and placed in GSG structures for high frequency parameter extraction. The amount of layout area dedicated to testing RF performance was limited for the Peregrine process since it would be admittedly poor with the large gate lengths. In both processes, each MESFET was designed to have multiple fingers having a number of nominally identical channels.

The ease of being able to control the threshold voltage is a distinct advantage of FD-MESFETs. Threshold voltage is dependent upon the separation of the silicide islands. For n-channel devices, the larger the separation, the more negative the threshold becomes due to the increased distance that needs to be overcome to fully deplete the channel and pinch it off. A comparable reasoning can be used to describe p-channel devices, except their threshold becomes more positive with increased separation. This is analogous to PD-MESFETs whose thresholds are directly related to vertical thickness of the channel. Vertical thickness however is not a parameter that can be changed without changing the CMOS process flow. Similarly, altering the doping concentration can be used to change the threshold but it also comes at the cost of changing the process flow [27].

Fig. 29 shows the threshold versus the channel width for both n-type and p-type devices on a FD-SOS MESFET process. Based on the linear fits which are represented by the dashed lines, it can be found that the threshold varies as -0.11 V/μm for n-MESFETs and +0.07 V/μm for p-MESFETs. Presumably the difference can be explained by the heavier doping in the n-well as compared to the p-well. These results suggest that complementary MESFET operation (i.e. $V_{tn} = -V_{tp}$ with similar saturated drain currents) could be achieved by optimizing the n- and p-well implants and the channel widths L_{CW}^{N} and L_{CW}^{P}, although that would require changes to the CMOS process flow itself as well [27].

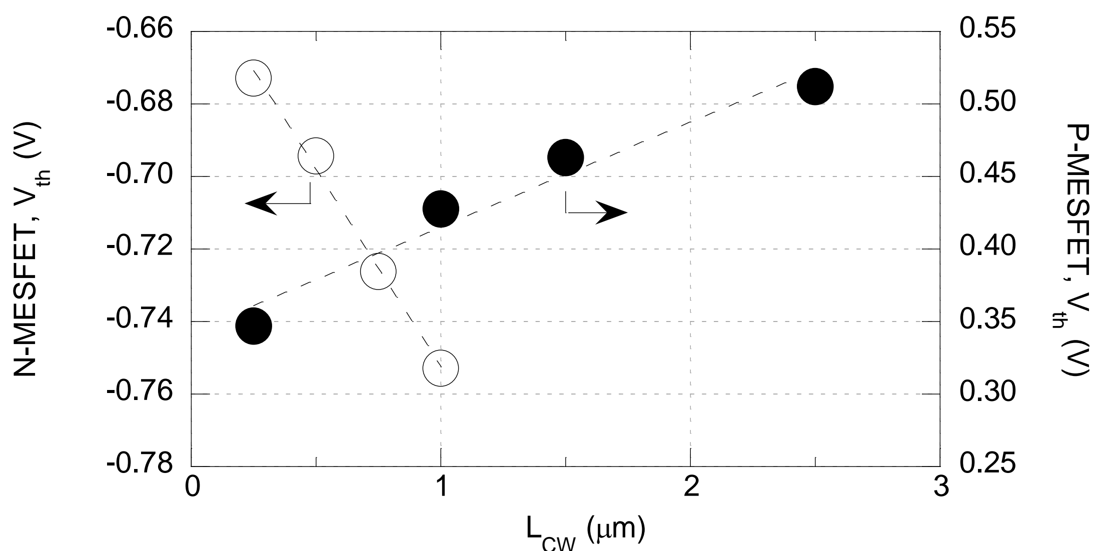

Fig. 29. Threshold voltage of SOS MESFETs as a function of the channel width. The dashed lines are linear fits to the data [27].

3.2. *Regions of Device Operation*

The regions of operation for this MESFET are illustrated by Fig. 30-Fig. 32. Fig. 30 is composed of 2-D drawings that show the lateral depletion growth

along a cross-section in the y-z plane as it expands from the edges of the silicide islands controlled by the gate. While the pinching off of the channel happens in the lateral direction, the depletion region will be unequal from the drain to the source as was the case for PD-MESFETs. Once again, above a few 10's of mV the depletion region will begin to favor the drain side of the device. Thus, Fig. 30 by itself is insufficient in describing the operation of FD-MESFET. Fig. 31 completes the description of the FD-MESFET with diagrams depicting the depletion region in a simplified top level view. This section is more or less a repeat of Section 1.3; nevertheless, due to the slight differences of the devices and depletion region growth in two planes it is useful to repeat.

At very low drain voltages and assuming $V_{GS} > V_t$, a current begins to flow in the channel created under L_{CW}. The depletion region starts to build up evenly along the silicide islands from the drain to the source. An electric field is established across the channel, resulting in a current flow that varies linearly with drain voltage. In this region of operation the channel operates as a resistor. The junction between the drain and the gate becomes more reversed biased with increasing drain voltage leading to the depletion region widening faster towards the drain side. The narrowing of the channel at the drain end leads to a decrease in the slope of I_D and the rounding off effect shown in Fig. 32 [14]. At a certain drain voltage the depletion width from each side of the silicide island touches and the channel becomes pinched off. Presumably, the pinch-off point will be closer to the drain side of the device. The region above the pinch-off point is the

saturation region. Theoretically, the slope of I_D becomes zero and the drain current becomes independent to further increases in drain voltage. Realistically, this is not the case due to channel length modulation effects. When V_{GS} becomes more negative the depletion width will see an increase due to the junction becoming more reversed biased. The reduced channel region leads to smaller slopes of I_D in the linear region; hence it is more resistive and pinches-off at lower drain voltages. Below $V_{GS} < V_t$, the channel becomes fully depleted and enters the subthreshold region. In this region small amounts of current flow still flow due to the diffusion of carriers in the space charge region [10].

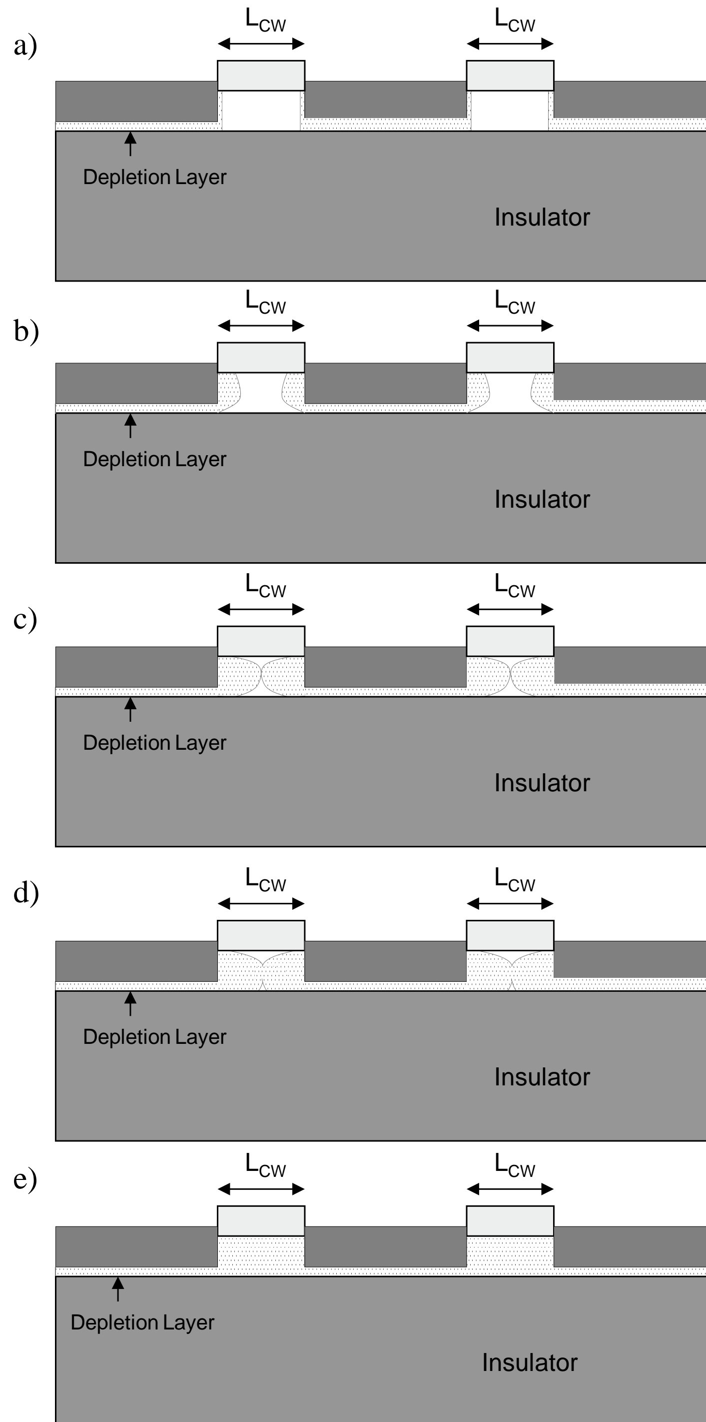

Fig. 30. Lateral depletion for various regions of device operation. a) $V_{GS} = 0$ V and $V_{DS} = 0$ V. b) Linear region: $V_{GS} = 0$ V and small V_{DS}. c) Pinch-off: $V_{GS} = 0$ V and $V_{DS} = V_{DSAT}$. d) Saturation region: $V_{GS} = 0$ V and $V_{DS} > V_{DSAT}$. e) Subthreshold region: $V_{GS} < V_t$ and $V_{DS} = 0$ V.

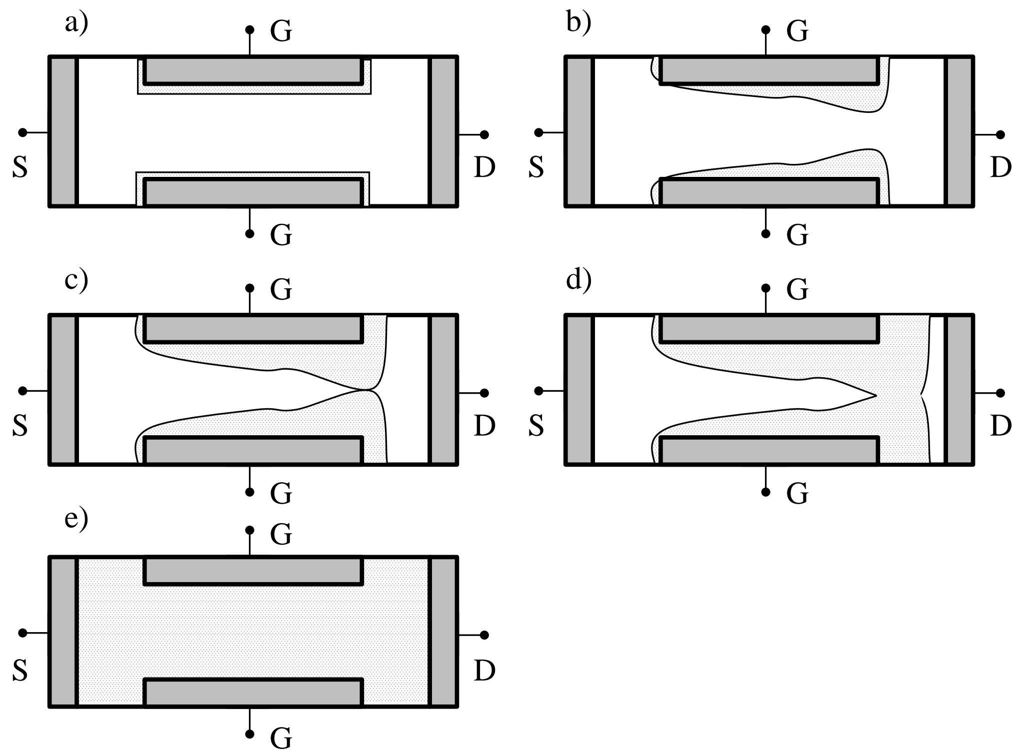

Fig. 31. Depletion growth from top view [14]. a) $V_{GS} = 0$ V and $V_{DS} = 0$ V. b) Linear region: $V_{GS} = 0$ V and small V_{DS}. c) Pinch-off: $V_{GS} = 0$ V and $V_{DS} = V_{DSAT}$. d) Saturation region: $V_{GS} = 0$ V and $V_{DS} > V_{DSAT}$. e) Subthreshold region: $V_{GS} < V_t$ and $V_{DS} = 0$ V.

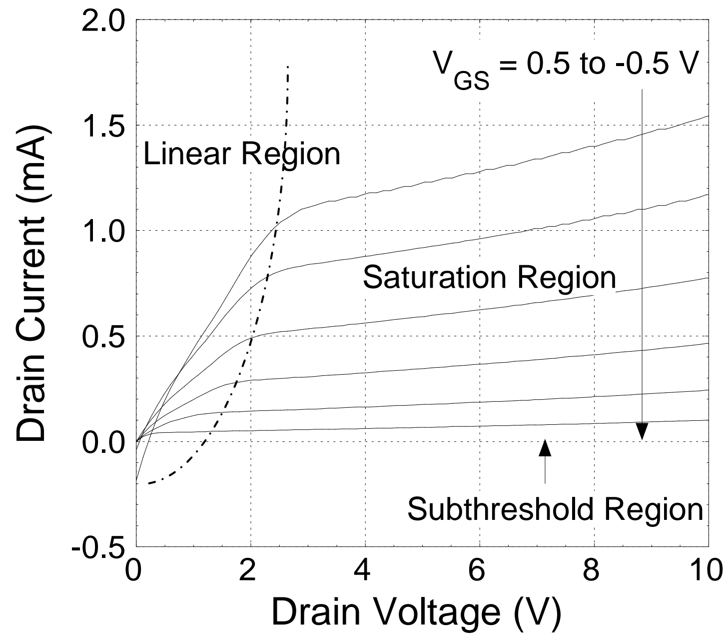

Fig. 32. Family of curves plot showing regions of MESFET operation.

3.3. *Turn-On Characteristics*

The turn-on characteristics of n- and p-channel MESFETs are shown in Fig. 33. For both types of devices the channel length was 1.8 µm with a total of 150 channels. The channel width was varied from 0.25 to 2.5 µm for the p-channel devices and in the range of 0.25 to 1 µm for the n-channel devices with all the devices operating in depletion mode. The inserts in Fig. 33 shows the I_G-V_{GS} data at the bias condition of $V_D = V_S = 0$ V for the $L_{CW} = 0.25$ µm devices. The dashed lines represent the fits to the exponential function.

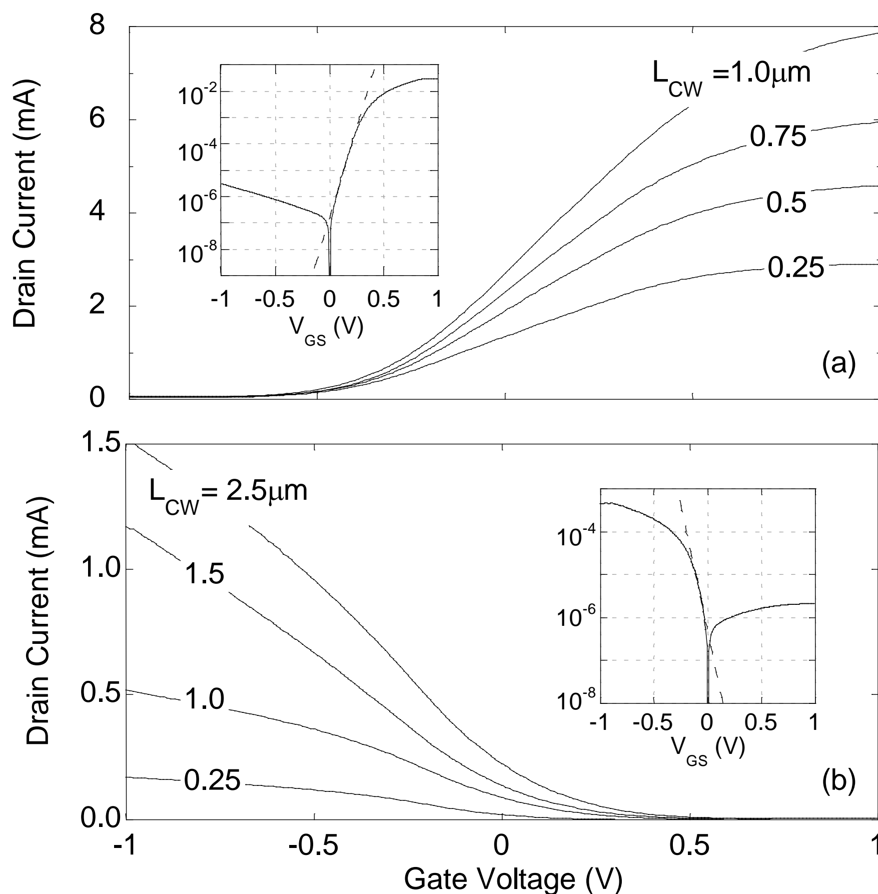

Fig. 33. The turn-on characteristics, I_D-V_{GS} for a) n-MESFETS (V_{DS} = 2 V) and b) p-MESFETs (V_{DS} = -2 V) for different channel widths. The insets show the magnitude of the gate current for L_{CW} = 0.25 μm.

From the fits an ideality factor of n = 1.24 for the n-MESFETs and n = 1.44 for the p-MESFETs can be extracted. The Schottky barrier can be also be extracted from the fit but this is complicated by the uncertainty in the conducting area of the MESFET gate. If the gate current at V_{DS} = 0 V flows predominantly out of the four vertical edges of the silicide gate islands then the total conducting gate area is given approximately by:

$$A = 4NL_gT_{Si} \tag{3.1}$$

where

N = number of channels

T_{Si} = thickness of Si channel.

For the SOS devices, $T_{Si} \approx 100$ nm [28] and the total gate area is ~$1.1\text{x}10^{-6}$ cm^2 for the devices with N = 150 channels. Assuming effective Richardson constants of 110 and 32 $A \cdot cm^{-2} \cdot K^{-2}$ [29], Equation 1.5 can be used to derive barrier heights of 0.48 and 0.41 eV respectively for the n- and p-channel MESFETs. The measured barrier height for the p-type MESFETs is in good agreement with the ~0.4 eV quoted in the literature for $CoSi_2$ on p-Si [30]. The value for the n-MESFETs is lower than the ~0.6 eV quoted for $CoSi_2$ on n-Si but is still reasonable given the uncertainty in the gate area.

3.4. BREAKDOWN MECHANISMS

The breakdown of the 0.25 μm FD-SOI CMOS was only 3.5 V which can be insufficient for certain analog circuit applications. In this same process, MESFETs with breakdowns exceeding 17 V were readily available without altering any of the process steps. Fig. 34a and b shows the family of curves plot for n-channel and p-channel devices which exhibited good output current saturation at drain voltages that greatly exceeded the CMOS breakdown. As was the case with PD-MESFETs, the high voltage capability of the FD-MESFETs is in large part due to the drift region between the ends of the channel and the drain contact and is a natural outcome of the non self-aligned MESFET geometry [1].

Extending the drift region helps reduce the electric field and increase the breakdown. Also contributing again is the Schottky gate of the MESFET which can tolerate high current flow and is much less fragile than a thin gate oxide.

As a side note in Fig. 34a and b, the saturated drain current of the n-MESFET is approximately 5x larger than the p-MESFET despite having an identical number of channels. This can be explained by the higher mobility expected for the n-channel device and the higher n-well doping.

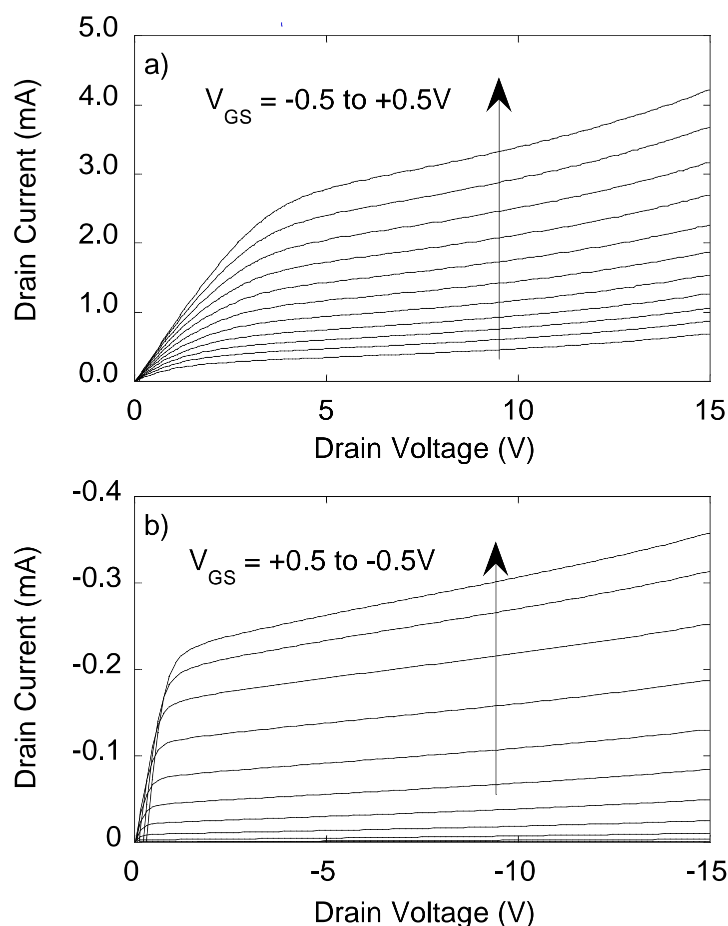

Fig. 34. The family of curves plot for a) the n-MESFET and b) the p-MESFET for gate voltages in the range of -0.5 to +0.5 V in 0.1 V steps. L_g^N = 1.8 µm, L_{CW}^N = 0.25 µm, L_g^P = 1.8 µm, and L_{CW}^P = 0.25 µm.

In order to reduce layout area and improve RF performance, polysilicon (poly) can be used to create the access region at the source. The access region created using the polysilicon is similar to a gate of MOSFET and will prevent the silicide step in the CMOS process from shorting the source to the gate. In the 0.25 μm FD-SOI CMOS process, the polysilicon can be patterned to be as small as 0.25 μm compared to 1.2 μm required for the silicide block. Polysilicon does break down at lower voltages then silicide block, but with the majority of the breakdown event taking place at the drain end, polysilicon can be substituted at the source end without dramatically affecting the breakdown of the device.

Doping levels can also alter the breakdown of the device. Similar to the case of MOSFETs, a higher doping implant will reduce the MESFETs depletion region at the n/n^+ junction from the gate to drain and reduce the breakdown of the device. In the Peregrine process, there were three different doping profiles available with the intention of having low and high threshold devices to go along with their standard PMOS and NMOS devices. Unfortunately, there was not a set of three MESFETs layouts with the exact same geometries with only the doping profile differing to physically test this theory. There is however two devices that can be compared, one with the standard implant and one with the heavy implant used for high threshold MOSFETs. Both MESFETs feature 150 channels, L_{CW} = 0.25 μm, L_g = 0.6 μm, L_{aS} = 0.6 μm (poly) and L_{aD} = 1.2 μm (SB). The device with the standard doping had a breakdown voltage of about 16 V while the high implant device was only 10.5 V. The breakdown was once again determined by

the Del Alamo drain-injection technique [25]. Fig. 35 compares the family of curves for each device and confirms that that the heavier doping will reduce its safe voltage range. While it reduced that specification, it did enhance the current drive and the output resistance of the device which would be beneficial for applications requiring higher gain. From here it can be concluded that if there was a similar device with the low implant doping it would have the best breakdown of the three devices but the worst current drive.

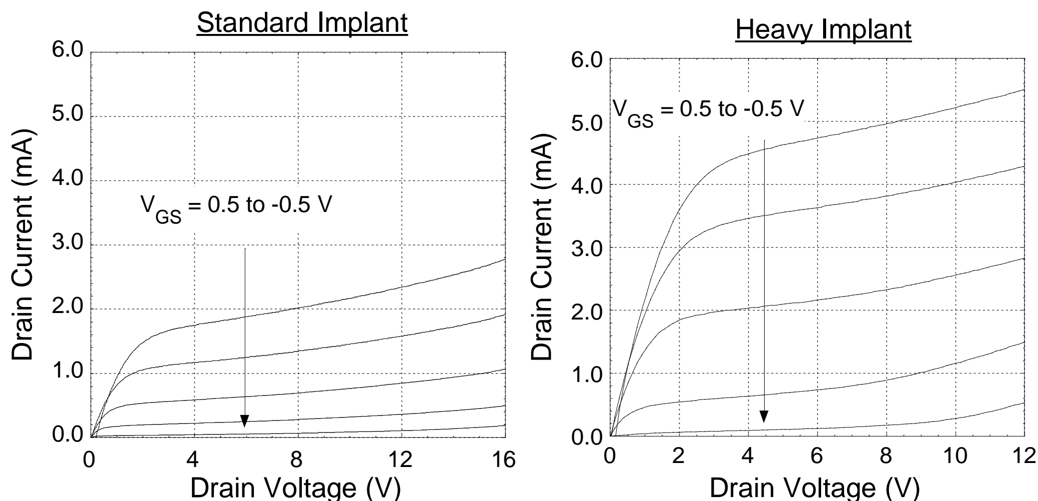

Fig. 35. Compares the FOC for two devices that are nominally the same but with different doping profiles. The heavier doping improved the current drive and output resistance, but reduced the breakdown voltage of the device.

3.5. *Layout Alternatives and Potential Improvements*

Fig. 27 is a straight forward way of laying out the FD-MESFET but it is certainly not the only solution. One way to reduce the effective gate length is to layout the device as shown in Fig. 36. As stated earlier in this chapter, the minimum gate length without breaking any layout rules with the Fig. 27 approach

is 1.8 µm. For the 0.25 µm FD-SOI CMOS process, 1.8 µm is not the minimum distance of poly to poly, SB to SB or even poly to SB. Therefore by extending the poly or SB used to create the access regions into the gate region the effective gate length can be reduced to 0.6 µm. Fig. 37a shows the improvement when the gate length is reduced from 1.8 µm to 0.6 µm for two devices that are nominally the same with respect to every other parameter including doping profile, number of channels, L_{CW}, L_{aS} and L_{aD}. These results however are slightly misleading due to the increased die area required to layout the structure in Fig. 36. There is a minimum width for both the poly and silicide block which is considerably larger than L_{CW} and the minimum distance between the contact and those two layers still needs to stay intact in order to not break design rules. Table 3 compares the area consumed by the two devices in Fig. 37a. Fig. 37b normalizes the data by showing current drive per unit area so that the two devices can be accurately compared. While the normalization has dampened some of the apparent current drive improvement, it can be expected that this device with an L_g = 0.6 µm will have a much more favorable RF performance. Additionally, these devices have a gate leakage current that is close to 3x less. This corresponds to the gate length which is one-third the size.

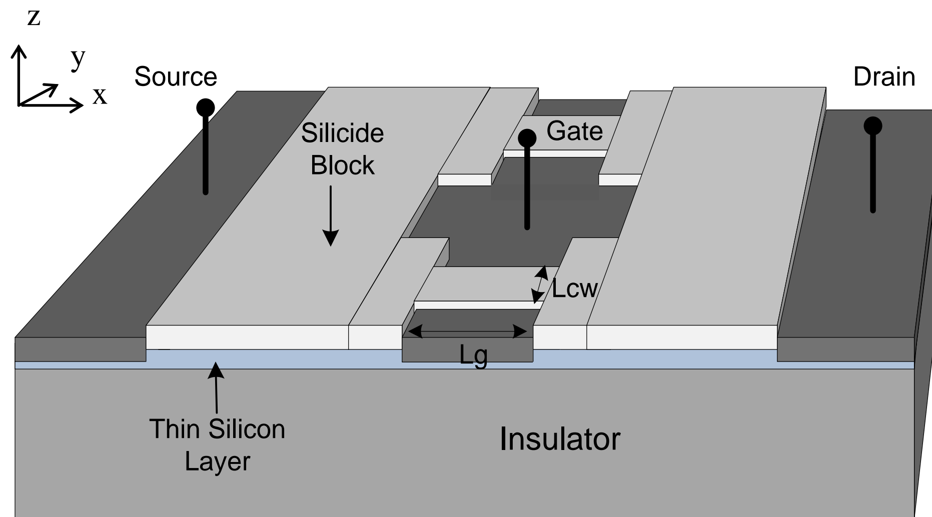

Fig. 36. 3-D rendering a FD-MESFET which extends silicide block into the gate region to reduce the effective gate length.

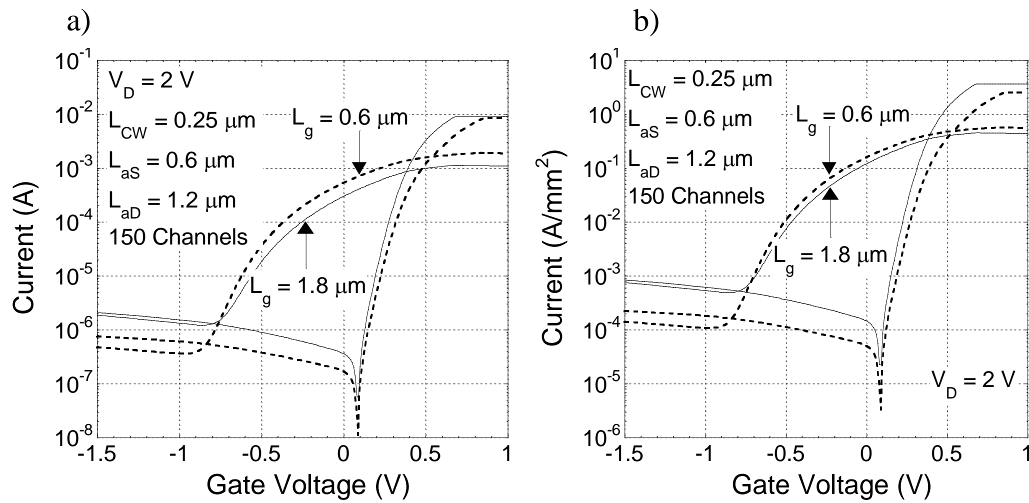

Fig. 37. a) Compares two devices, that are nominally similar expect one utilizes the structure in Fig. 27 (L_g = 1.8 μm--solid line) and the other uses Fig. 36 (L_g =0.6 μm--dashed line). b) Compares the two devices after they have been normalized to current per unit area.

Table 3: Area of MESFETs in Fig. 37a

Layout Structure	*Area*
Fig. 27	18.6 x 138 μm
Fig. 36	24.3 x 138 μm

Another possible architecture is shown in Fig. 38. This device is a combination of the ideas presented in Fig. 27 and Fig. 36. The basic principle is to extend the polysilicon or silicide block from the access region into gate region like in Fig. 36. Unlike Fig. 36 which put the extended pieces of the access region directly across from each other, this device offsets them. The effective gate length is now the distance between the pieces and can now be made less than 0.6 μm without breaking any layout rules. Theoretically this distance can approach zero, however as shown in Fig. 39, there is a limit to how much the effective gate length can be reduced. The devices in Fig. 39 are from the MIT-LL process since there was not a complete set of devices to compare on the Peregrine process. Nevertheless, the concept will still be the same. By offsetting the gate by half in Fig. 39a, a significant increase in drive current can be seen. While the threshold becomes more negative, the device still shows enough gate control to be useful in different circuit applications. The device designed with a full offset and theoretical $L_g = 0$ μm further increases the current drive but shows very little gate control and does not really ever shutoff. As was the case with Fig. 36, this layout will increase the die area slightly; refer to Table 4 for the different sizes. For each finger, the length in the x-direction would increase by the length of the added

access region. The rest of the dimensions would be the same as in Fig. 27. In devices with several channels per finger this device would have a smaller layout area than the one in Fig. 36.

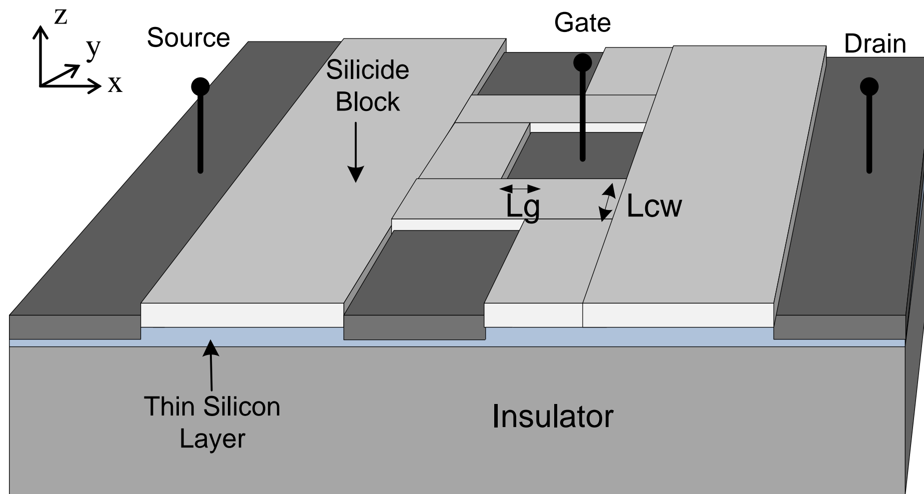

Fig. 38. 3-D rendering of a FD-MESFET showing silicide block being offset in order to reduce the effective gate length.

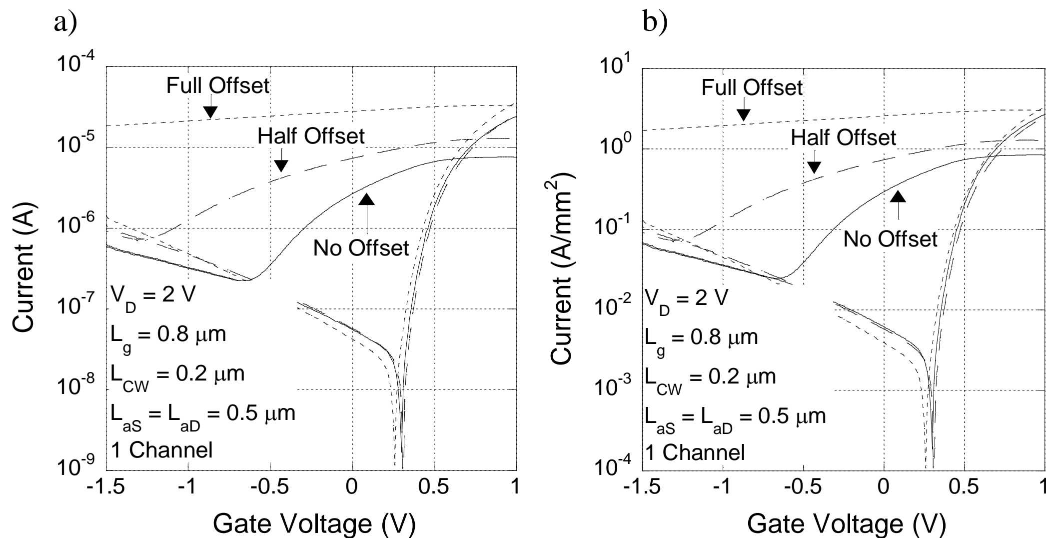

Fig. 39. a) Compares the Gummel plots of three devices with different gate offsets on the MIT-LL process. b) Compares the same devices after they have been normalized to current per unit area.

Table 4: Area of MESFETs in Fig. 39a

Offset	*Area*
No Offset	4.015 x 2.25 µm
Half Offset	4.415 x 2.25 µm
Full Offset	4.815 x 2.25 µm

3.6. MODELING

The FD-SOI MESFETs which are typically operated in depletion-mode can be modeled using the Triquint's Own Model (TOM3). The TOM3 is a three terminal SPICE based model originally developed for modeling the DC and RF characteristics of GaAs MESFETs as an extension to the Curtice-Statz model. The model encompasses an efficient large-signal model and uses charge parameters to represent the capacitance. With the thick semi-insulating substrate of GaAs MESFETs, the device is isolated from the effects of non-zero biases on the substrate [10]. For PD-SOI wafers, the buried oxide is relatively thin resulting in significant difference in device operation based on the bias on the substrate. As a result a four-terminal model is required for PD-SOI MESFETs. While the buried oxide layer is thin for FD-SOI wafers, FD-SOI MESFETs are effectively three terminal devices due to the thin layer of silicon not consumed by the formation of metal silicide of the Schottky gate being fully depleted under all operating conditions.

The TOM3 model itself though is insufficient in modeling the FD-SOI MESFET's soft and hard breakdown. Furthermore, the model has trouble matching the slope of the gate leakage current in the reverse biased region of the curve. If Cadence [31] is being used to simulate the circuit, there is an option in the Analog Design Environment under Simulation → Options → Analog which has the parameter g_{min} that can be adjusted to model the slope of the leakage current (Fig. 40). This method is only effective if the circuit being design is comprised of only MESFETs since g_{min} is also is common to the MOSFETs and will affect their operation. A better solution is to use the diode sub-circuits, marked by I_{BDS} and I_{BGD} in Fig. 41 which can be used to model both the breakdown and the reverse gate leakage.

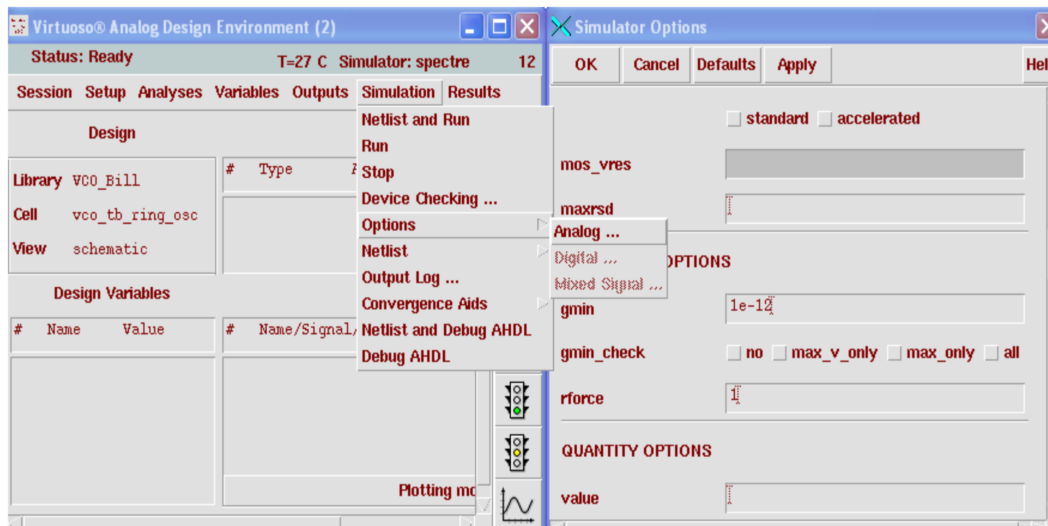

Fig. 40. Screen shot of how to change g_{min} in Cadence's Analog Design Environment.

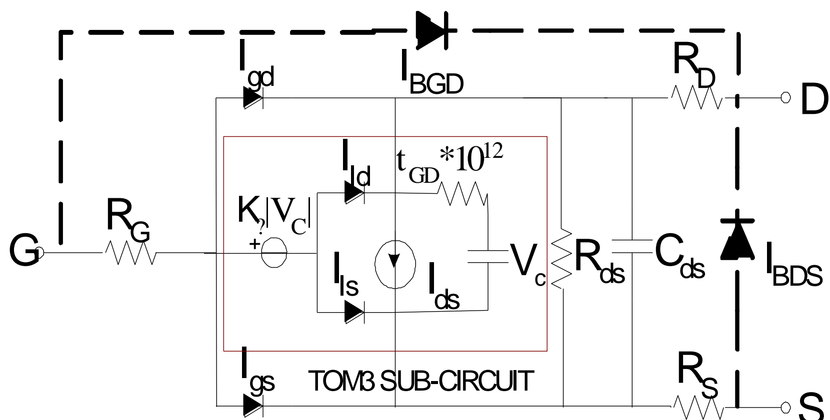

Fig. 41. Large signal model of a MESFET with the TOM3 sub-circuit. I_{BGD} and I_{BDS} are used to model the breakdown voltage in the circuit [23].

Aside from the sub-circuit diodes, the MESFET TOM3 model consists of parasitic resistances at the source (R_S), gate (R_G), and drain (R_D), a voltage-controlled current source (I_{ds}), and a drain-to-source capacitor (C_{ds}). The TOM3 model accounts for the gate-to-source capacitance, C_{gs}, in its charge based model which is described in detail in [23, 32]. The model also includes circuitry to model the drain dispersion and self-heating effects.

The modeling and extraction of FD-SOI MESFETs was based on an approach developed by Balijepalli for PD-SOI MESFETs [10]. Using her method, modeling of the DC operation was done for two different devices on the Peregrine process. Fig. 42-Fig. 45 show the modeling for one of those devices. The device features 300 channels, L_{CW} = 0.25 μm, L_g = 1.8 μm, L_{aS} = L_{aD} = 1.2 μm (poly), and the standard doping profile. In each figure the measured results are represented by the solid line and the simulated model is shown by the open circles.

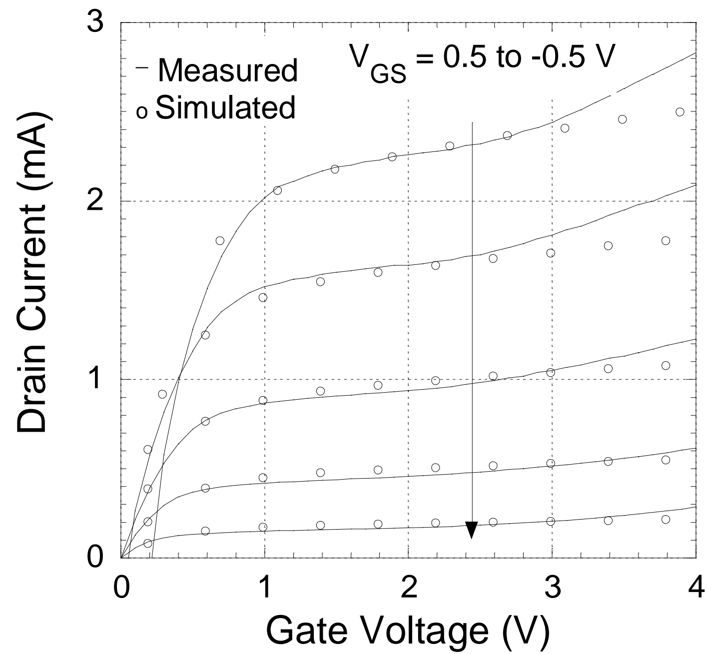

Fig. 42. Compares the measured results (solid line) to the simulated model (open circles) for the family of curves plot.

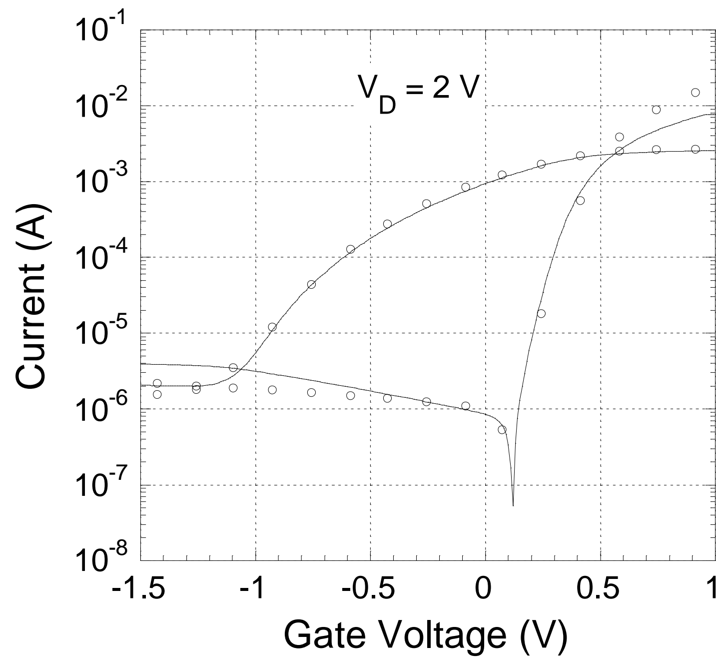

Fig. 43. Compares the Gummel plots of the measured results (solid line) to the simulated model (open circles).

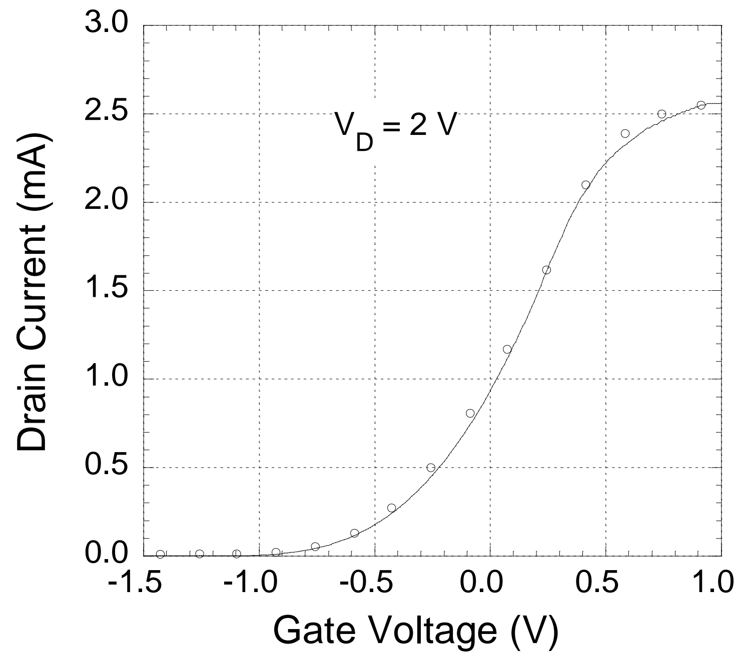

Fig. 44. Compares the measured results (solid line) to the simulated model (open circles) for the drain current vs. gate voltage at $V_D = 2$ V.

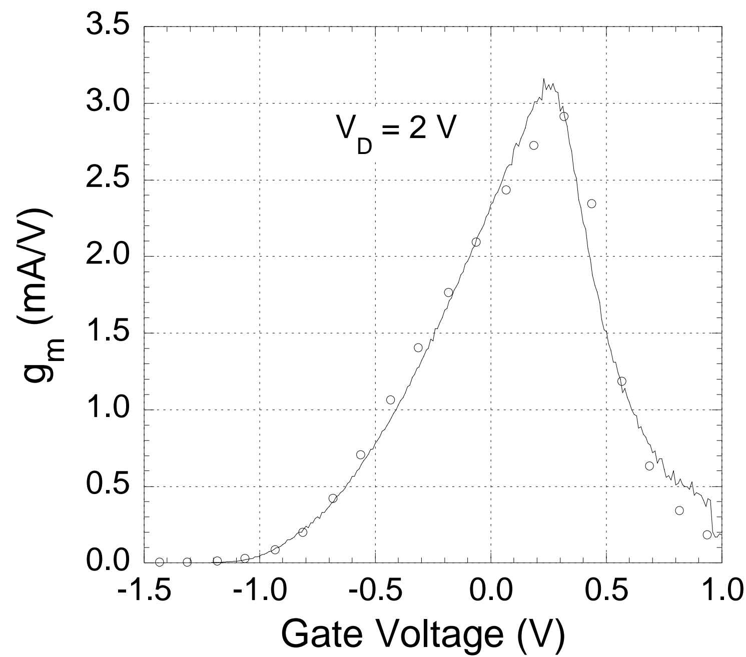

Fig. 45. Compares the g_m of the measured results (solid line) to the simulated model (open circles) at $V_D = 2$ V.

3.7. *CONCLUSION*

In this chapter it was shown how the MESFET concept can be applied to FD-CMOS technologies. Also, it was seen that the performance of the FD-MESFET is highly tied to the photolithography rules of the contact, silicide block, and/or polysilicon layers. The layout rules limited the FD-MESFET more so than the PD-MESFET which is only limited by the silicide block layer. To overcome these issues, different layout structures where presented as a way to improve the MESFET's overall performance [33].

CHAPTER 4

N-MESFET LDO

One of the primary concerns and key selling point for battery powered electronics is the design of the power management system. With consumer's continued expectation that products such as cell phones and laptops last longer and longer without recharging, power management systems can ill afford to waste any unnecessary power that will degrade battery lifetime and potential sales of the product. As such, most complex systems incorporate several voltage regulators to optimally supply the various components within the system. This as a result has driven the market for ultra low dropout LDOs. These LDOs can feature extremely high power efficiencies under certain line and load conditions.

LDOs are also particularly popular in applications that are sized constrained and/or noise sensitive. Commercial LDOs are available in extremely small packages and in general have superior noise performance and fewer required external components than switching regulators. The MESFET based LDO furthers this point by providing stable regulation independent of a charge pump and load capacitor across all line and load conditions. Having no external capacitance is particularly important in ultra-compact applications since the capacitor can be close to the size of the LDO itself. Furthermore, if a capacitor is present, additional real estate on the PCB board will be needed for added traces and spacing between the two components. Having no output capacitor is also important for system-on-chip designs since it will save the chip a pin that could be used elsewhere.

This chapter presents an LDO that was fabricated on the same 0.25 μm FD-SOS CMOS process discussed in Chapter 3 and is centered on a FD-MESFET pass device. As mentioned in the previous chapters, MESFETs can be integrated alongside the SOS CMOS devices at no additional cost or change to the process. This enables designs to take advantage of both technologies and yield the highest performance. The MESFET based LDO demonstrates this approach by implementing the rest of the LDO minus the pass transistor with SOS CMOS transistors.

4.1. PMOS LDO Overview

The most critical aspect of the LDO regulator design is in the implementation of the pass transistor. The choice of the pass transistor affects the LDO's stability, dropout voltage, transient response, ground current, and almost every other critical figure of merit. The most common implementation of LDOs employs a PMOS device as the pass transistor in a common-source (CS) configuration as shown in Fig. 46. The CS architecture is popular since it can produce very low dropout voltages that are theoretically dependent only on the on-resistance, R_{on}, of the pass transistor and the load current, I_{load} without a charge pump (Equation 4.1). In reality though, the dropout voltage also must include the parasitic voltage drops from the metal routing lines. These parasitic voltage drops can become significant at higher load currents.

$$V_{DO(PMOS-LDO)} = R_{on} I_{load} = V_{DSAT} \tag{4.1}$$

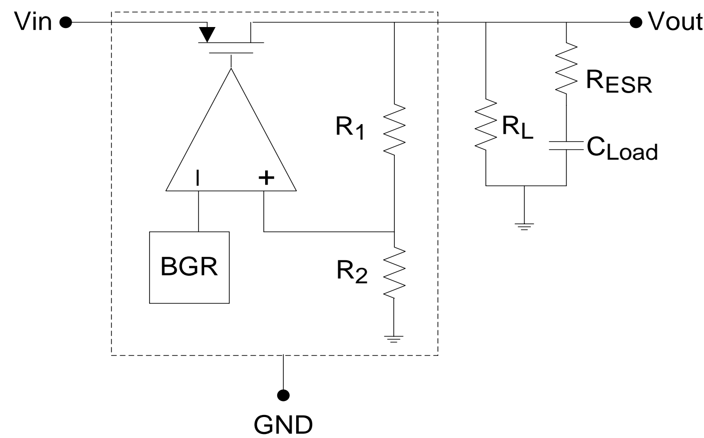

Fig. 46. Basic circuit schematic of a LDO using a P-channel pass transistor in a common source configuration. The LDO has been compensated through C_{Load} and R_{ESR} [26].

The downside of this topology is the mobility of the holes in a PMOS device is usually 2-3x lower than the mobility of electrons in NMOS transistors. Therefore to have a certain current drive for the pass transistor, the PMOS device needs to be 2-3x larger than a NMOS transistor. PMOS-based LDOs also have the propensity to oscillate without proper compensation. Essentially, the low dropout voltage is the only significant advantage to using this particular type of architecture; however, since power dissipation is such an important specification it has remained in the majority of LDOs.

The instability of PMOS-based LDOs is the result of the high output impedance caused by the CS architecture (Equation 4.2). Typically this issue is combated by the use of an external capacitor with some equivalent series resistance (ESR) value to create a zero in the compensation loop. In battery operated applications, ceramic and tantalum capacitors are usually the capacitors of choice with ceramic capacitors being preferred since they are cheaper and

come in small packages. For older LDOs, careful design was needed in choosing an appropriate load capacitor. If the ESR value associated with the capacitor was too small or too big, the LDO could oscillate. Companies simplified the process slightly for end users by including figures in datasheets like the one in Fig. 47 [34]. From the figure, it be can be determined that this particular LDO with a 4.7 µF load capacitor needs an ESR value between 0.3 and 8 Ω across all loads to guarantee stability. Based on that, a tantalum capacitor would probably be recommended for the simplest solution since it usually encompasses an ESR value that is not too high or too low as to cause instability. With a ceramic capacitor on the other hand, an additional external series resistor might be needed to meet the ESR requirement since they frequently have very low ESR values. Several new LDOs are now being designed to be stable with little to no ESR. This removes the previous concern with ceramics, but not the chief issue of needing an external capacitor.

$$R_{out} = r_{o(pmos)} // (R_1 + R_1) // R_L \approx r_{o(pmos)} \tag{4.2}$$

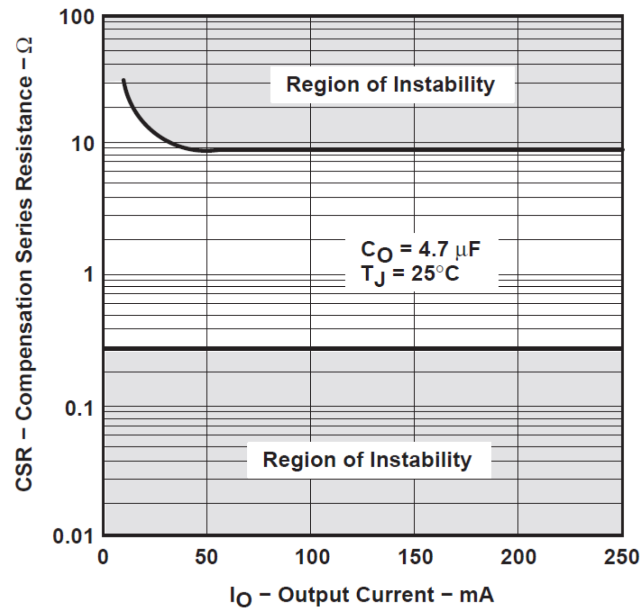

Fig. 47. Range of stability chart for the Texas Instruments TPS76301 LDO. CSR refers to the ESR from the capacitor plus any external resistor if applicable [34].

Fig. 48 illustrates the key internal parasitic sources as well as the added external components that affect the stability of the LDO system. Although it is not shown in Fig. 46, it can be assumed that the error amplifier is a single stage, one pole amplifier followed by a buffer. A buffer is needed to drive the large capacitive impedance created by the very large pass device. With the buffer now being accounted for, the corresponding close loop response is shown in Fig. 49. The first pole, P_1, (Equation 4.3) is determined by the load capacitor, C_{Load}, ESR value, and the resistance at the LDO's output which was found in Equation 4.2. The combination of the output impedance of the error amplifier represented by C_{O1} and R_{O1} and the input capacitance of the buffer, C_{I2}, forms the second pole, P_2, (Equation 4.4). In Equation 4.4, the combination of C_{O1} and C_{I2} is represented as C_{par1}. Depending on the C_{Load} selection, design of the buffer, and size of pass

transistor, P_1 and P_2 can be reversed [35-37]. Nevertheless, they are usually found at low frequencies. The placement of the zero, Z_1, (Equation 4.5) is determined by C_{Load} and its associated ESR. Lastly, P_3, (Equation 4.6) is the combination of the output resistance of the buffer, R_{O2}, its capacitance, C_{O2}, and the parasitic capacitance of the pass transistor, C_{pmos}. The combination of C_{O2} and C_{pmos} is represented by C_{par2} in Equation 4.6. Compensation is further complicated by the fact that P_1 will move under different load conditions with the worst case occurring when the load current is at its highest [37]. At that point $r_{o(pmos)}$ and consequently R_{out} is at its lowest which causes P_1 and the gain bandwidth (GBW) to be pushed to higher frequencies. This effect must be taken into account when determining Z_1 [35]. There are additional poles present in the LDO loop; however, since they occur at frequencies much higher than the GBW they were neglected from this discussion [36-37].

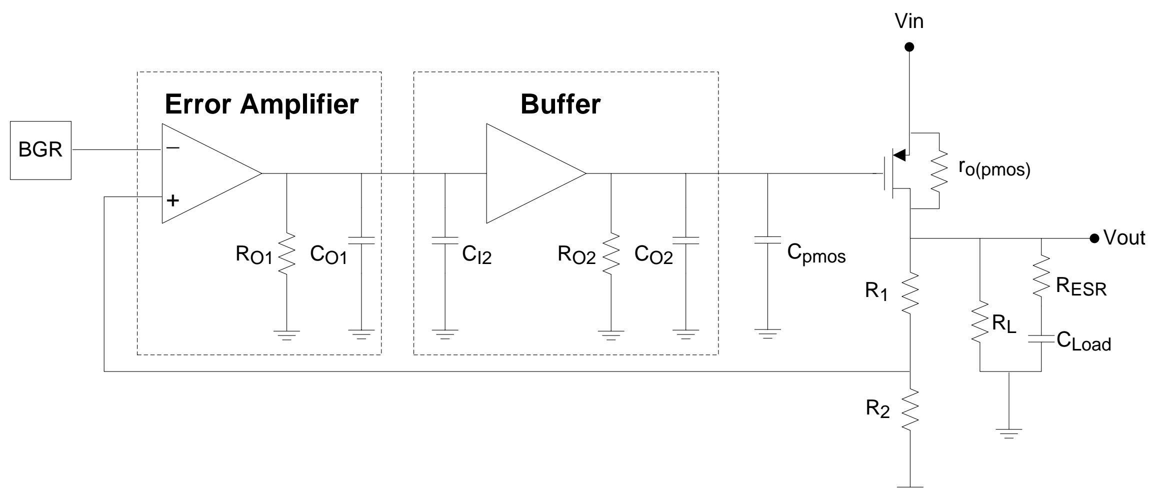

Fig. 48. Includes the key internal parasitic components as well as the added external components that affect the stability of the PMOS LDO system.

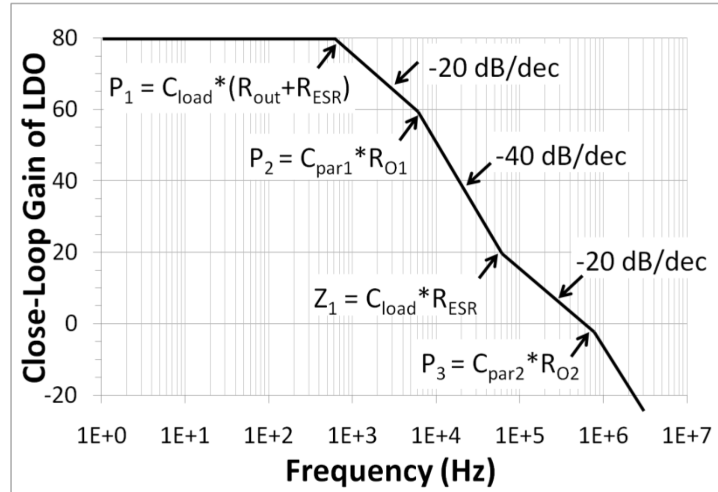

Fig. 49. Closed-loop gain response of a compensated LDO utilizing a PMOS pass transistor.

$$f_{P1} \approx \frac{1}{2\pi C_{Load}(R_{out} + R_{ESR})} \tag{4.3}$$

$$f_{P2} \approx \frac{1}{2\pi C_{par1} R_{O1}} \tag{4.4}$$

$$f_{Z1} \approx \frac{1}{2\pi C_{Load} R_{ESR}} \tag{4.5}$$

$$f_{P3} \approx \frac{1}{2\pi C_{par2} R_{O2}} \tag{4.6}$$

4.2. NMOS LDO OVERVIEW

NMOS (enhancement mode) linear regulators use the pass transistor of the LDO in a common drain configuration (CD) as shown in Fig. 50. For stability purposes, a CD configuration is highly desirable. By taking the output of the LDO at the source of the pass transistor, the equivalent resistance at the output node

now reduces to ≈ $1/g_m$ (Equation 4.7). This in turn pushes the pole created by capacitance seen at the source of the MESFET and whatever component it is driving to much higher frequencies.

The critical internal parasitic components that affect the stability of the NMOS LDO system are shown in

Fig. 51. The poles of the system can be found in an analogous manner to that of Fig. 48 with an NMOS pass transistor replacing the PMOS device. There is no C_{Load} or R_{ESR} since the system can be stable without external compensation. Again, it can be assumed that the error amplifier is a single stage, one pole amplifier followed by a buffer. The requirements on this buffer lessen though since the capacitive impedance, C_{NMOS}, at the input of the pass device decreases as result of a smaller sized transistor being able to achieve a given current rating. The dominant pole, P_1, is formed by the output impedance of the error amplifier (C_{O1} and R_{O1}) and the input capacitance of the buffer, C_{I2}. The combination of C_{O1} and C_{I2} form C_{par1} in Equation 4.8. The second pole, P_2, results from C_{par2} and the output resistance of the buffer, R_{O2} (Equation 4.9). C_{par2} consists of C_{NMOS} and the buffer's output capacitance, C_{O2}. As shown in Fig. 52, with an appropriate placement of the dominant pole, the closed-loop response can be treated as a single pole system [35] and be unconditional stability. Once again, there are poles present in the LDO loop; however, since they occur at frequencies much higher than the GBW they can also be neglected.

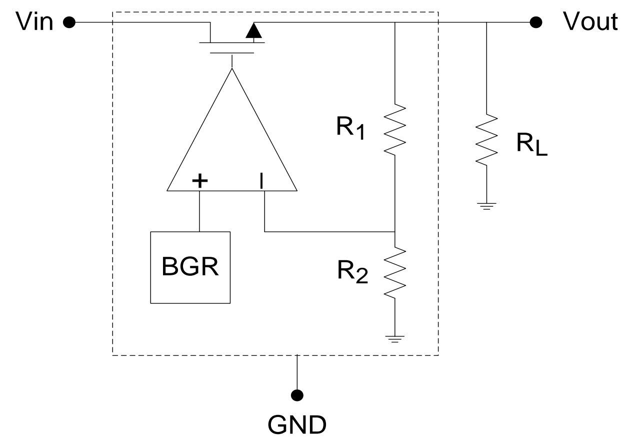

Fig. 50. Circuit schematic of an LDO using a NMOS pass transistor in a common drain configuration.

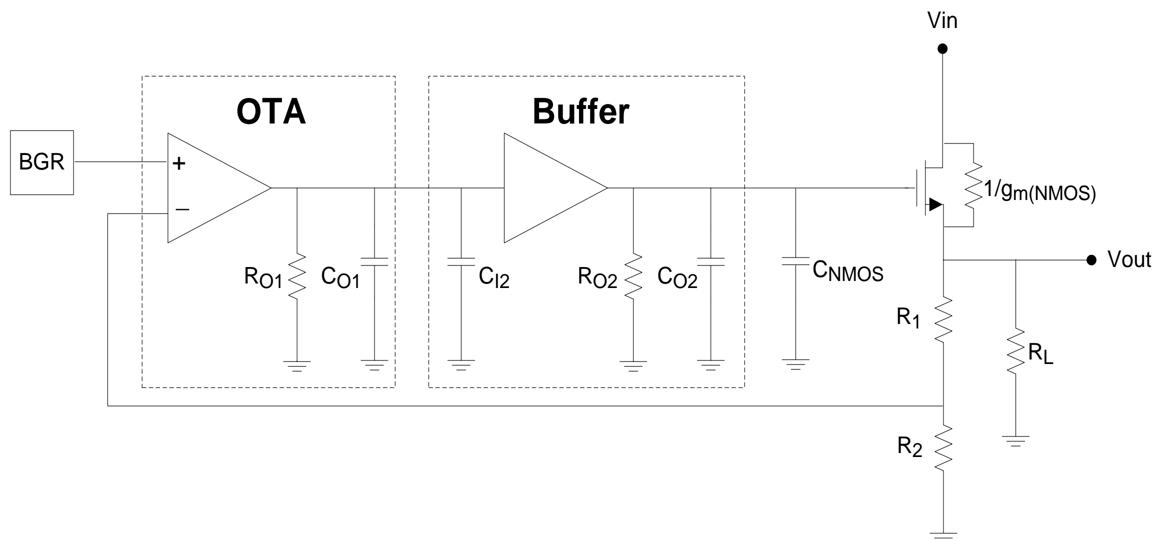

Fig. 51. Includes the key internal parasitic components that affect the stability of the NMOS LDO system.

$$R_{out} = \frac{1}{g_{m(NMOS)}} // (R_1 + R_1) // R_L \approx \frac{1}{g_{m(NMOS)}} \tag{4.7}$$

$$f_{P1} \approx \frac{1}{2\pi C_{par1} R_{O1}} \tag{4.8}$$

$$f_{P2} \approx \frac{1}{2\pi C_{par2} R_{O2}} \tag{4.9}$$

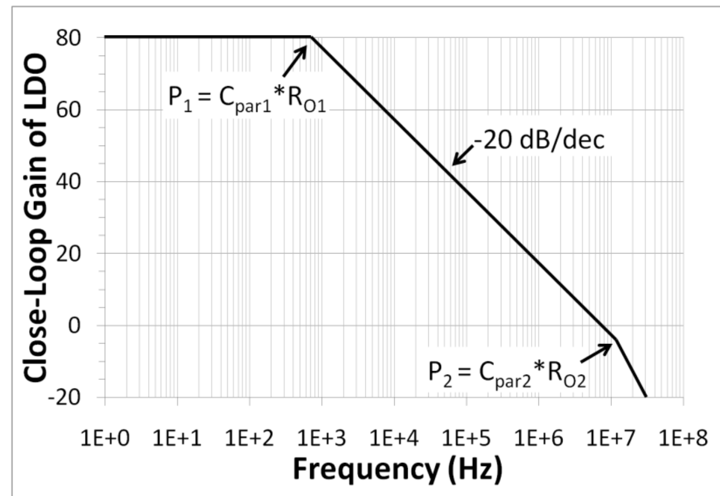

Fig. 52. Closed-loop gain response of an LDO utilizing a NMOS pass transistor.

Other advantages include a smaller pass transistor, as mentioned earlier due to the mobility of electrons, and enhanced transient results. The transient response of an LDO is limited by the bandwidth of the LDO system. The higher frequency placement of the pole from the pass transistor allows for an extended bandwidth while still maintaining a high degree of phase margin. Even with all those advantages, NMOS pass transistors are not too popular for implementing in LDOs. A source follower requires the voltage at the gate of the pass device to be a threshold voltage, V_t, higher than V_{out} at the source node. Consequently V_{DO} from Equation 4.1 increases by V_t leading to higher power dissipation. This was not an issue for PMOS-based LDOs since the gate of the PMOS transistor can be driven below its drain where the output is taken.

Charge pumps and servo-based control loops are common tactics used for removing V_t from V_{DO}. Their presence enables the gate of the NMOS device to be higher than the input voltage, V_{in}. While these may be good solutions for system-on-a-chip applications that provide modest point-of-load currents, usually less than 50 mA [38], they begin to add significant output noise and take up substantial die area for applications that require greater than 100 mA load currents. State-of-the-art technologies though have considerably reduced the area required for the charge pump leading to more LDOs employing this topology. Even so, NMOS-based LDOs are still in the minority.

$$V_{DO(NMOS)} = V_t + R_{on} * I_{load} = V_t + V_{DSAT} \tag{4.10}$$

4.3. N-MESFET LDO Overview

The key point to pull away from the previous section is the enhancement mode nature of NMOS devices requires the designer to either deal with a high dropout voltage, refer to Equation 4.10, or to incorporate a charge pump and accept all its unwanted side effects. N-MESFETs remove the charge pump dilemma by virtue of being a depletion mode device that can be almost fully turned on with a gate-to-source voltage, V_{GS}, equal to 0 V. It is this feature that allows the MESFET based LDO to be in the inherently stable source follower configuration of Fig. 53 and have a dropout voltage independent of the threshold voltage.

The key poles that affect the stability will be the same as

Fig. 51 and Equations 4.8 and 4.9. Consequently, it will have a single pole, closed-loop gain response like Fig. 52. The only difference of note between the standard NMOS LDO topology and the MESFET LDO in Fig. 53 is it includes an optional PMOS power down switch which will be explained more in *Section 4.5*. This will add some additional parasitic capacitance at the drain of the MESFET but the contribution will be relatively small since the switch is only a tenth of the size of the pass transistor. Plus the added parasitic capacitances will be at the MESFET's drain node and will be the PMOS's drain-to-gate and the drain-to-source capacitances. Both of these are relatively small, thus, the overall closed-loop response remains virtually unchanged.

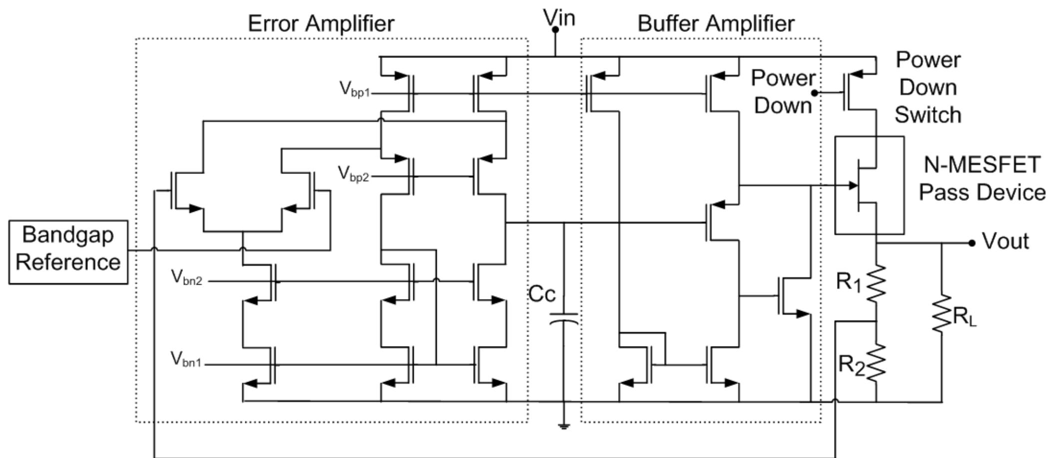

Fig. 53. Schematic of the LDO regulator using an N-MESFET pass transistor.

4.4. SELECTING N-MESFET PASS DEVICE

The N-MESFET LDO that was fabricated and tested was based on the FD-MESFET shown in Fig. 54. Fig. 54 shows the MESFET's measured and

simulated drain and gate current at a drain-to-source voltage equal to 25 mV. 25 mV was taken as the bias point since it represented the original goal for dropout voltage performance at a 50 mA load. The device encompasses the basic layout structure presented in Fig. 27. Its core characteristics are as follows: 150 channels, L_g = 1.8 μm, L_{CW} = 1 μm, L_{aS} = 0.6 μm (poly), L_{aD} = 1.2 μm (SB), $V_t \approx 0.8V$, and it was doped with the heavy implant (refer to Chapter 3 for more information on how these characteristics affect the FD-MESFET's operation). This particular device was fabricated on a process run that took place in 2007, about a year and a half before the LDO was fabricated. It was chosen from an assortment of other MESFETs for four primary reasons: current drive per die area, threshold voltage, expected RF performance, and die-to-die consistency in performance. The actual pass device was made with 103,680 channels and is approximately 691x larger. As mentioned in Chapters 1-3, MESFETs have a natural high breakdown capability. The breakdown of this MESFET is > 7 V which is about twice the breakdown of the SOS CMOS on the same process.

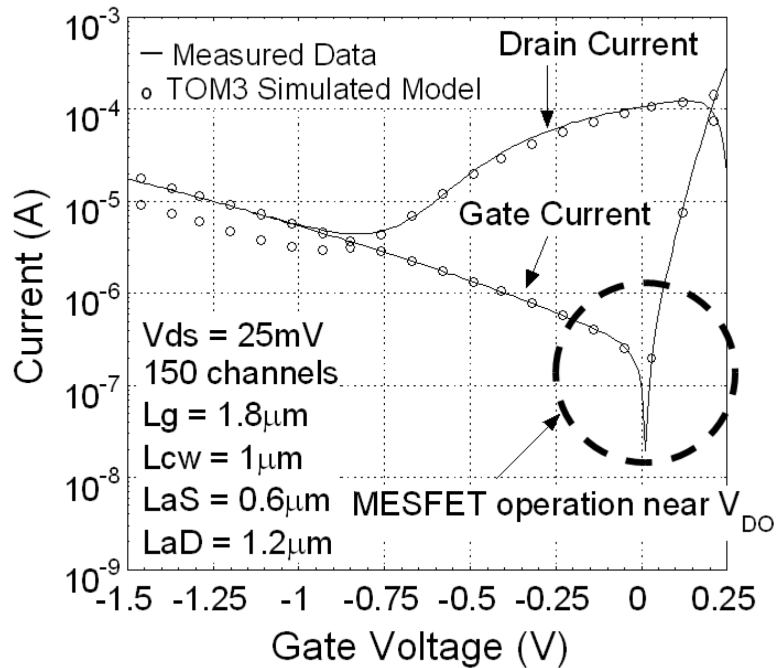

Fig. 54. Measured and simulated drain and gate current of the scaled down MESFET used in the LDO.

4.5. *N-MESFET LDO Issues*

Fig. 54 also exhibits two downsides of the MESFET compared to a CMOS transistor. First, the Schottky gate of the MESFET has appreciable current flowing under forward and reverse bias. Secondly, the MESFET cannot be switched off as hard as a MOSFET. Both of these issues represent an obvious problem if a complete power-down is desired to reduce the quiescent power dissipation during off-state operation. One solution is to use a PMOS switch in series with the MESFET which is shown in Fig. 53. The P-MOSFET isolates the MESFET from the input voltage and prevents it from conducting when needed. If the LDO does not require a power-down functionality, the PMOS device should

be removed since it will increase the dropout in accordance with Equation 4.11. However, since the PMOS device is driven hard (V_{GS} = $-V_{in}$), the $R_{on(PMOS)}$ is small and does not require substantial silicon area to reduce its resistance. In fact, the PMOS device only accounts for about 10% of the total die area and < 4% of the total dropout voltage at a load of 75 mA. Fig. 55 shows the complete effect of the PMOS switch across all loads.

$$V_{DO} = (R_{on(N-MES)} + R_{on(PMOS)}) * I_{load}$$
$$= V_{DSAT(N-MES)} + V_{DSAT(PMOS)} \tag{4.11}$$

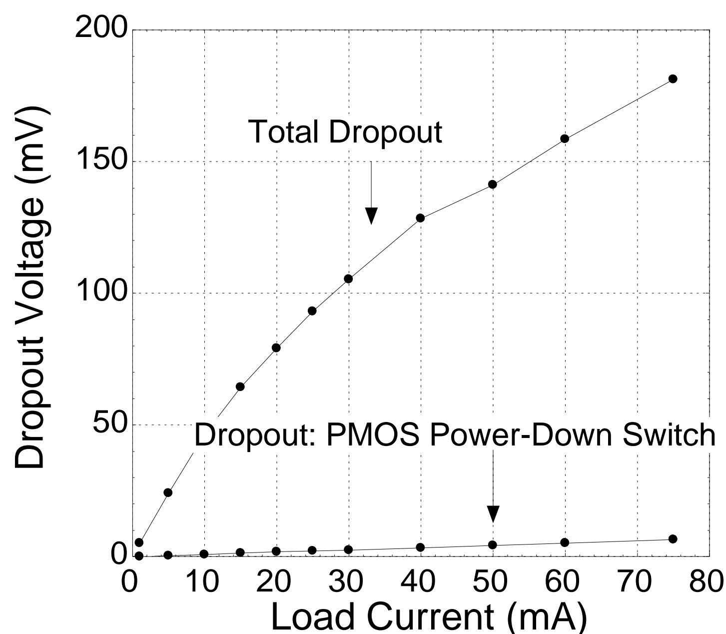

Fig. 55. Measured total dropout voltage resulting from the PMOS power-down switch and N-MESFET pass device. Also shown is the contribution from only the PMOS switch.

For most operating regimes, the Schottky gate of the MESFET will be reversed biased. This causes the gate current to flow away from the load, out of the gate, and contribute to the ground current, I_{gnd}. Near the dropout voltage

though, the MESFET operates around the inflection point, marked by the dotted circle in Fig. 54 and will have gate currents of a few magnitudes lower. Consequently, it is in this region where the MESFET based LDO sees its highest current (Equation 4.12) and power efficiency (Equation 4.13). In Fig. 56, it can be seen that the MESFET based LDO would not be ideal for light loads since the ground current is on par with the load current. On the other hand, for heavier loads, the ground current only marginally increases and the current efficiency approaches 99%.

$$I_{efficiency} = \frac{I_{in} - I_{gnd}}{I_{in}} = \frac{I_{load}}{I_{in}} \tag{4.12}$$

$$P_{efficiency} = \frac{I_{load} * V_{out}}{(I_{load} + I_{gnd}) * V_{in}} \tag{4.13}$$

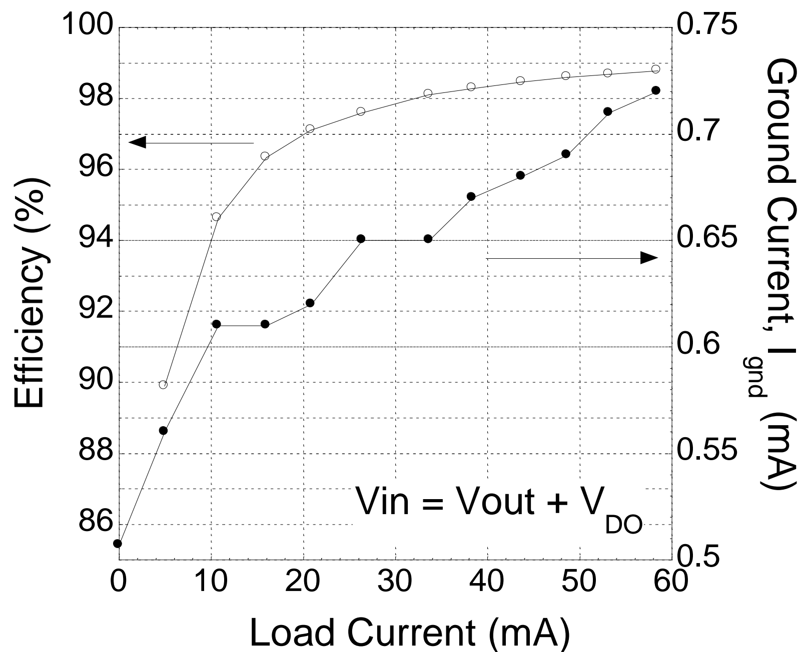

Fig. 56. Measured ground current and current efficiency versus load current. At higher loads the current efficiency approaches 99%.

Another problematic issue with ground current arises from the steep negative slope of the reverse bias gate leakage; see Fig. 54. As the input voltage increases, the V_{DS} across the pass transistor increases making it easier for the LDO to supply the load current. In order to maintain regulation, the negative feedback of the LDO loop responds by driving the V_{GS} of the MESFET more negative. This not only drives the operating point away from the point of inflection where the gate current is the lowest but further up the gate leakage curve. Under very light or no load conditions the gate bias point will approach the MESFET's pinch-off point which is where the gate and drain currents meet. Due to this, the threshold voltage plays an important role in the overall ground current of the LDO since the pinch-off point will be related to it. The threshold voltage

also determines how hard the device turns on at V_{GS} = 0 V so there is a tradeoff that exists.

4.6. *MEASUREMENT SETUP & PCB BOARD DESIGN*

The PCB test board in Fig. 57 was schematically designed in National Instrument's (NI) Multisim program and exported to NI's Ultiboard for layout. The board incorporated several test points through the use of 2 x 1 headers to measure node voltages and currents (the headers are the components labeled with J in Fig. 57). The headers also enabled the board to only connect components that were necessary for each particular test. Below is a list of the different measurements included in this thesis as well as a brief description of how the PCB was configured to perform the measurements.

1. Ground Current: The input current was measured through J2 and was compared to the load current measured through J16 (Fig. 56).
2. Dropout Voltage: V_{in} was swept with a HP 4155B semiconductor parameter analyzer. The dropout voltage was measured at the point where V_{out} dipped to 98% of its nominal output voltage. Through different combinations of J7-J9 (Fig. 55), the LDO could measure the dropout voltage at eight different current loads.
3. Transient Line Regulation: A HP 8110A pulse generator was used to quickly step V_{in} from a voltage comfortably above dropout to a voltage

100-200 mV above that (Fig. 59). V_{in} and V_{out} were captured with an Agilent 54832D oscilloscope and HP 10073A scope probes.

4. Transient Load Regulation: The same HP 8110A was used to quickly switch the gate of a 2N3904 BJT. When the BJT was turned on, ~10 mA was added to the load through R2. V_{in} and V_{out} were also captured with the Agilent 54832D oscilloscope and HP 10073A scope probes.
5. PSRR: The input ripple (50 mV_{pp}) was created with a HP33120A waveform generator. The small V_{out} ripple was then measured with a SR844 RF lock in amplifier.

Other notes: The PMOS switch could be switched on and off through J12. J13 allowed an off-chip capacitor to be connected at the output of the bandgap gap reference to suppress noise. J14 was connected at the drain of the PMOS switch as a way to measure the dropout contribution from only the PMOS switch (Fig. 55).

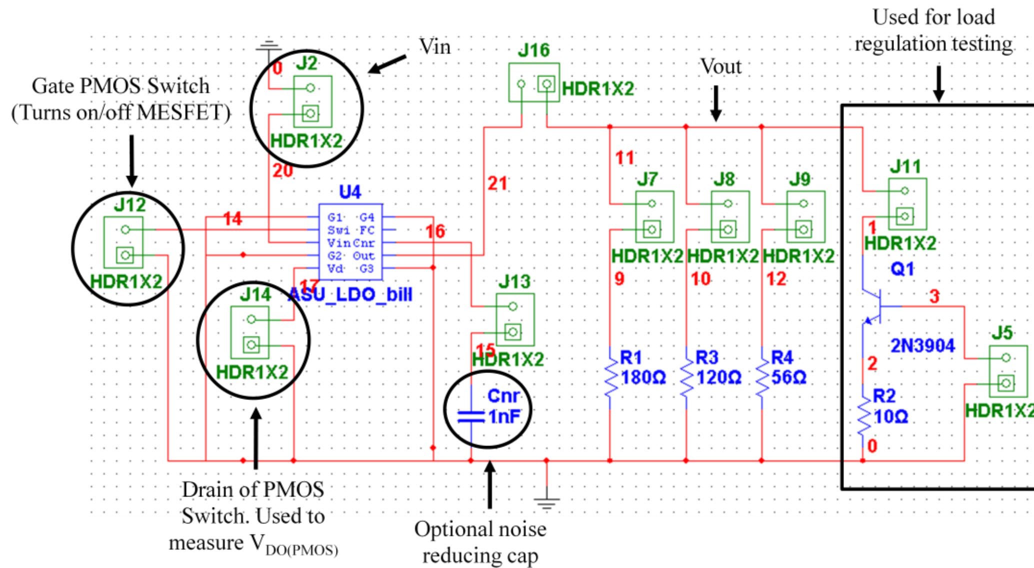

Fig. 57. Multisim schematic of the PCB test board.

A die micrograph of the LDO and PCB is shown in Fig. 58a and b respectively. The area of the layout, omitting the pads, is approximately 2.8 x 1 mm with the MESFET pass transistor contributing ~ 85% of the area. The PCB was two sided, 2” x 2,” and plated with gold. The bond wires were also gold and were in the range of about 2 to 3 mm. To minimize the dropout contributed by the bond wires, about 20 bond wires were each used for V_{in} and V_{out}. The resistors and the noise reducing capacitor soldered to the board were surface mount components in either 0805 or 0603 packages while the 2N3904 BJT was in a TO-92 package. The 2N3904 BJT was chosen for its very low input capacitance; ~8 pF. With it, the load contributed by R2 (Fig. 57) could be switched on and off in about 100 ns. Refer to Appendix A for a table of the 2N3904’s electrical characteristics. Lastly, an epoxy coating was placed over the die and the bond wires for the sole purpose of protecting it. It did not aid or alter its operation.

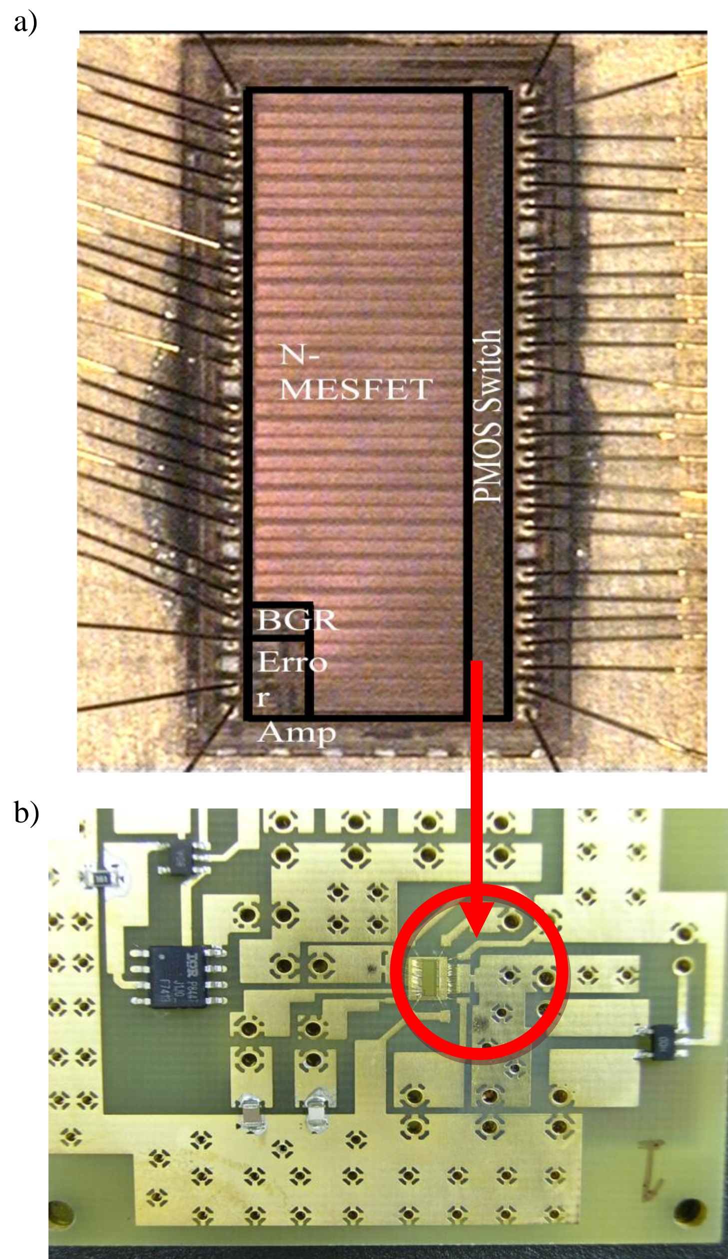

Fig. 58. a) Die micrograph of the LDO. b) Picture of the bonded LDO on a gold-plated PCB.

4.7. *BUFFER DESIGN AND TRANSIENT RESULTS*

As mentioned earlier, one of the main benefits of using an N-channel pass transistor in a source follower configuration is it allows for a much higher system bandwidth and enhanced transient operation. The MESFET based LDO designed in Fig. 53 took advantage of this by incorporating a wideband error amplifier based on a folded cascode structure. Bandwidth was further improved through the buffer which utilized shunt feedback at the output of the buffer's source follower to lower its output resistance and push its contributing pole to higher frequency. Equally as important, the shunt feedback enabled the buffer to be built with small transistors while still maintaining its low output resistance [39]. The largest transistor in the buffer was the shunt feedback transistor which had to be big enough to handle the reverse bias leakage current of the MESFET under all line and load conditions. Even so, its total width was only 105 μm. Not only did that save die space, but it lowered the input capacitance seen at the output of the folded-cascode. As a result, the dominant pole of the LDO which is at the -3 dB frequency (Equation 4.14) of the folded cascade also benefits.

$$f_{-3dB_Folded-cascode} = \frac{1}{2\pi C_L R_{out}}$$

(4.14)

With its large loop bandwidth, the MESFET LDO regulator was able to exhibit fast line and load regulation. During line regulation, the output voltage settled in ~800 ns with a critically damped response for both the low-to-high and

high-to-low transitions (Fig. 59). Slight overshoot was observed in the presence of a 12 pF parasitic output capacitance created by the HP 10073A scope probe. Similarly for the low-to-high transition of the load regulation, V_{out} quickly settled with a critically damped response in ~800 ns (Fig. 60). The high-to-low transition on the other hand had one large overshoot and one large undershoot before settling. Part of the over and undershoot is a response to the undershoot in the load step caused by the 2N3904 BJT quickly discharging and not just the LDO itself.

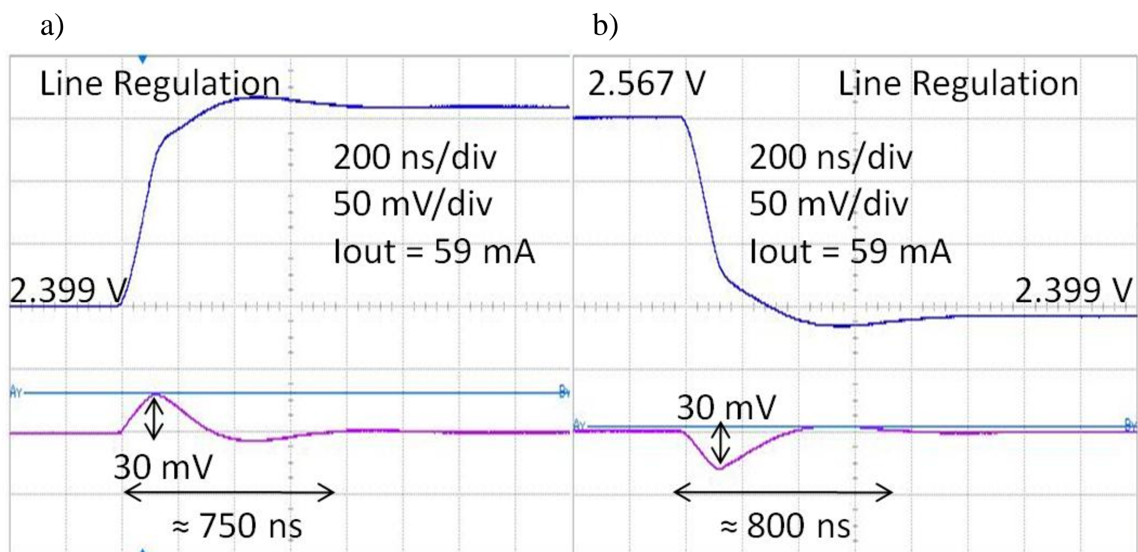

Fig. 59. Measured line regulation for both the low-to-high, a), and high-to-low transitions, b). The output voltage settles in less than ≤ 800 ns.

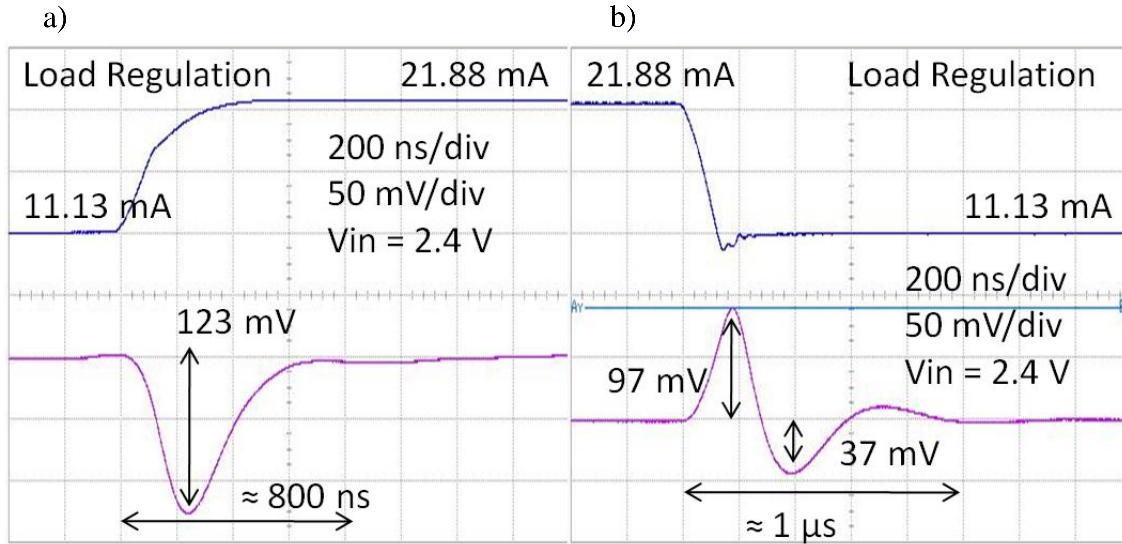

Fig. 60. Measured load regulation for both the low-to-high, a), and high-to-low transitions, b). The output voltage settles in less than ≤ 1 µs.

4.8. *PSRR Results*

The PSRR is a figure of merit of how well a LDO can suppress disturbances at the input (Equation 4.15) and is a function of the error amplifier, pass transistor, and feedback resistors. For noise sensitive RF applications, like cell phones, it is absolutely necessary to have a high PSRR. The roll off in PSRR was around 10 kHz in this case (Fig. 61) and was set by the dominant pole found in Equation 4.8. The rest of the degradation in PSRR with respect to frequency coincides with the loop bandwidth of the LDO. There are number of ways to improve the PSRR including improving the gain of the error amplifier and/or adding a cascode structure between the pass transistor and supply [36, 40]. For this LDO, the PSRR was about 45 dB for frequencies less than 10 kHz at loads of 10.8 mA and 34 mA (Fig. 61).

$$PSRR = 20\log_{10}\frac{V_{in,ripple}}{V_{out,ripple}} \tag{4.15}$$

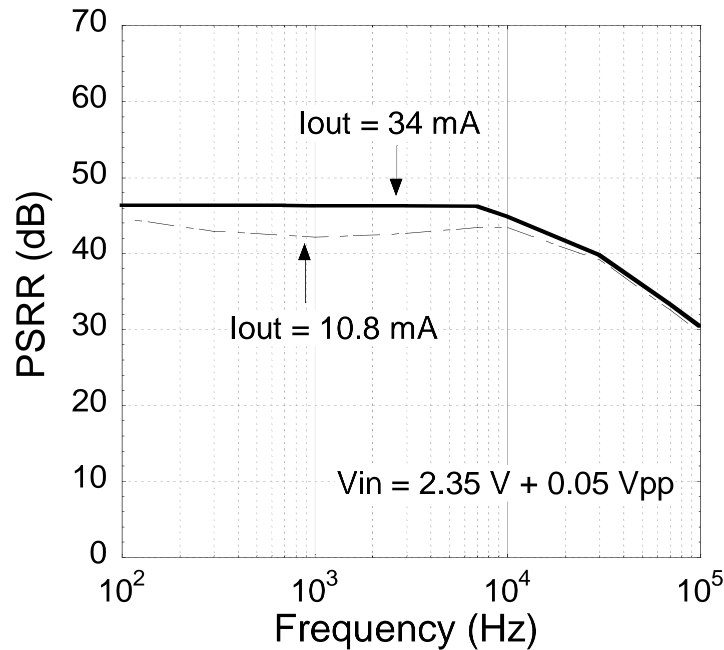

Fig. 61. PSRR for loads of 10.8 and 34 mA.

4.9. *Improving FD-MESFET LDOs*

One way to improve the performance of the LDO is to design the MESFET with the same characteristics listed in *Section 4.4* but with the structure in Fig. 36. As shown in Fig. 37, both the current drive and gate current improved in their respective matter. This type of device was not chosen for this particular LDO since the device was not fabricated on the 2007 process run. Without having the MESFET to characterize, there was no way to accurately model the device. There were other similar MESFETs which could have been used to approximate its operation, but if the estimated model was off, particularly with respect to the

RF parameters, it ran the risk that the final LDO would not be stable without an external load capacitor. There was also the risk that the device would not work. That risk is relatively small though since the majority of the MESFETs fabricated with Peregrine have worked in some capacity including those that are similar to the one being proposed. Nevertheless, the most conservative route was chosen for the first design run.

Another option for improving the LDO would be to use a more state-of-the-art FD-CMOS process or having a 0.25 μm FD technology that is more aggressively scaled with respect to the backend metal layers. In this particular process the backend metals were similar to that of 0.6 μm process. Even slight reductions in layout rules will lead to sizable savings in die space due to the sheer number of channels. For example, if the layout was done on Peregrine's new 0.25 μm process with everything in the layout exactly the same expect for the MESFET, the LDO die area would be 511 x 195.7 μm smaller. That is equates to about a 35% reduction. The new process would also shrink the gate length from 1.8 μm to 1.15 μm. If previous MESFET performance with respect to gate length holds true, a 25-35% increase in current drive can be also be expected. Likewise there should be a similar reduction in gate current. Table 5 summarizes the layout rules that affect the MESFET. The GC process was the process used for this LDO and the Px process is Peregrine's newer process.

Table 5: Improvements in Peregrine's Newer Process

Parameter	*GC Process*	*Px Process*
Contact	0.6 x 0.6 μm	0.4 x 0.4 μm
Contact to Contact	0.8 μm	0.35 μm
Contact to Poly	0.6 μm	0.4 μm
Contact to SB	0.6 μm	0.6 μm
Metal1 to Metal1	0.8 μm	0.4 μm

4.10. Conclusions

The final results of the LDO are summarized in Table 6. The LDO featured fast responses, < 1 μs, to changes in line and load and was stable under all conditions without an external capacitor. It proved MESFETs can work effectively as a pass transistor and be easily integrated with a complex analog circuit. While the MESFET does require a large die size to achieve its dropout voltage and current rating, it is important to consider that it is performing on a FD-CMOS process and the gate length was limited to 1.8 μm by the layout rules. Significant improvements can be achieved though on FD-CMOS processes with a different MESFET layout structure such as Fig. 36 and/or a slightly more advantageous process with smaller BEOL design rules such as the Px process from Peregrine.

Table 6: LDO Performance Summary

Process	*0.25μm SOS CMOS*
V_{in}	2-3V
V_{out}	2.0V
C_{Load}	N/A
Peak PSRR (V_{in} = 2.36V + 0.05V_{pp})	48dB
V_{DO} (I_{out} = 75mA)	180mV
Current Efficiency ($V_{in} = V_{out} + V_{DO}$ & I_{out} > 20mA)	97%
Line Regulation (L-H & I_{out} = 59mA)	ΔV = 30mV, Δt = 750ns
Line Regulation (H-L & I_{out} = 59mA)	ΔV = 30 mV, Δt = 800ns
Load Regulation (L-H & V_{in} = 2.4V)	ΔV = 123mV, Δt = 800ns
Load Regulation (H-L & V_{in} = 2.4V)	ΔV_1 = 97mV, ΔV_2 = 37mV, Δt = 1μs

CHAPTER 5

PD SOI MESFET LDOs

The FD-MESFET LDO from Chapter 4 presented a unique yet simple solution for an n-channel LDO. Due to a few key design rules though which adversely affected the layout size of the MESFET and consequently its current drive, that LDO was not a practical solution. As will be shown in this chapter, better and possibly state-of-the-art performance can be obtained by switching to a PD-CMOS process and using a PD-MESFET as the pass transistor. With fewer layout rules restricting their design, the gate length and device structure can be made much more compact. This is evident with the PD-MESFETs fabricated on the Honeywell 0.15 µm PD-SOI CMOS process in Chapter 2. While gate lengths on that process were conceivably able to scale down to 0.15 µm, good depletion mode behavior combined with good output resistance characteristics was not seen until L_g ~0.3 µm. Still using that L_g = 0.3 µm device converts to a current drive per die area that is more than 20x greater than the one chosen in Chapter 4 and a gate leakage current that is over 100x smaller (Fig. 62 and Table 7). From a design perspective, the reduced leakage current lessens the constraints on the buffer and allows for a simpler architecture to be used.

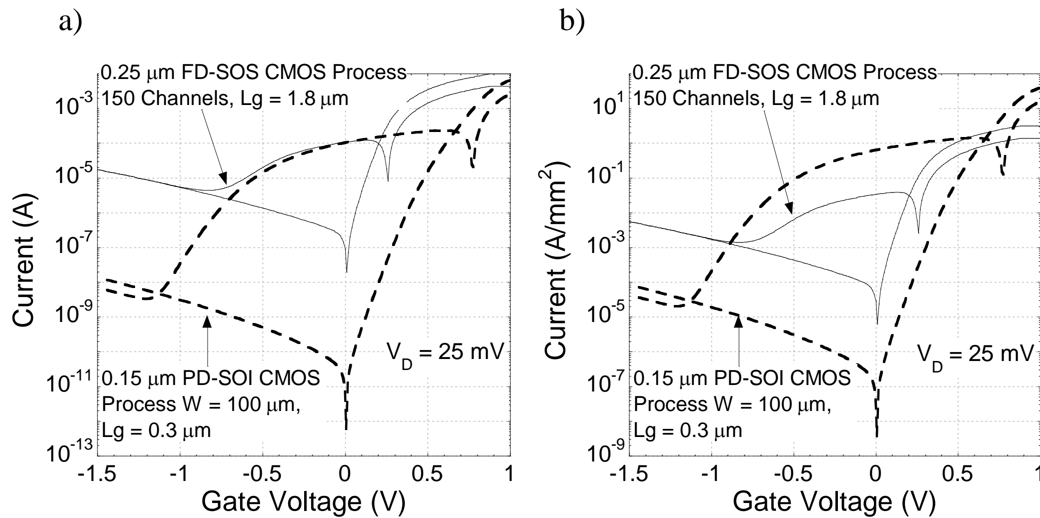

Fig. 62. a) Compares MESFETs from FD and PD technologies to exhibit the gain in current drive and reduction in gate current with PD-MESFETs. b) Compares the two in Part a) after they have been normalized.

Table 7: Area of MESFETs in Fig. 62

Process	*Area*
PD-SOI MESFET (L_g = 0.3 μm)	12.34 x 13.21 μm
FD-SOS MESFET (L_g = 1.8 μm)	22.8 x 138 μm

5.1. *PD-MESFET LDO Overview*

With a very short lead time preceding the process run a fully integrated PD-MESFET LDO was not fabricated. Instead, only a large discrete pass device based on the one in Fig. 62 with a width of 119.28 mm and dimensions of 0.73 x 0.55 mm excluding the pads was included. The device was then bonded in a DIP-8 package (Fig. 63) and mounted on a PCB board. The rest of the LDO's building blocks except for the voltage reference (V_{ref}) were composed of surface mount

components. To show the versatility of the PD-MESFET LDO, two different flavors of error amplifiers were used in measurements. One exhibited very low quiescent current, I_q, while the other had a moderate I_q, but a much larger bandwidth (refer to Appendix A for the datasheets of both devices). All the voltages including V_{ref} was supplied and monitored by an HP4155B parameter analyzer. Lastly, R_1 and R_2 were chosen so V_{out} was 1.8 V and DC measurements were limited to 100mA due the compliance of the HP4155B.

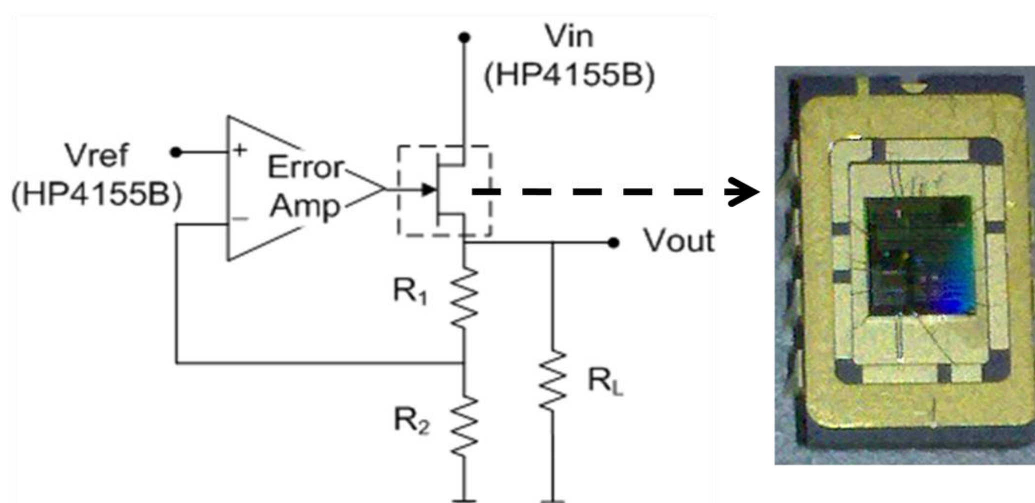

Fig. 63. Simple circuit schematic of the board level LDO design with a picture of the bonded out die. The device excluding pads is 0.73 x 0.55 mm while the cavity of the DIP-8 package is 7.37 x 4.32 mm.

The design of the PCB board (Fig. 64) was very similar to the one in Chapter 4. Once again, a 2N3904 BJT was included to conduct load transient measurements and a series of 2 x 1 headers were added to enable the board to connect only the necessary components for each particular test. The only major difference was electing to use a DIP-8 package instead of bonding the bare die directly to the board. This dramatically increased the flexibility for testing and

helped lower costs. On the downside, the dropout voltage now also includes the leads from the DIP package and the socket. A schematic of the board is shown in Fig. 65. A zoomed in picture of an unbonded bare die can be found in Fig. 86 in Appendix B.

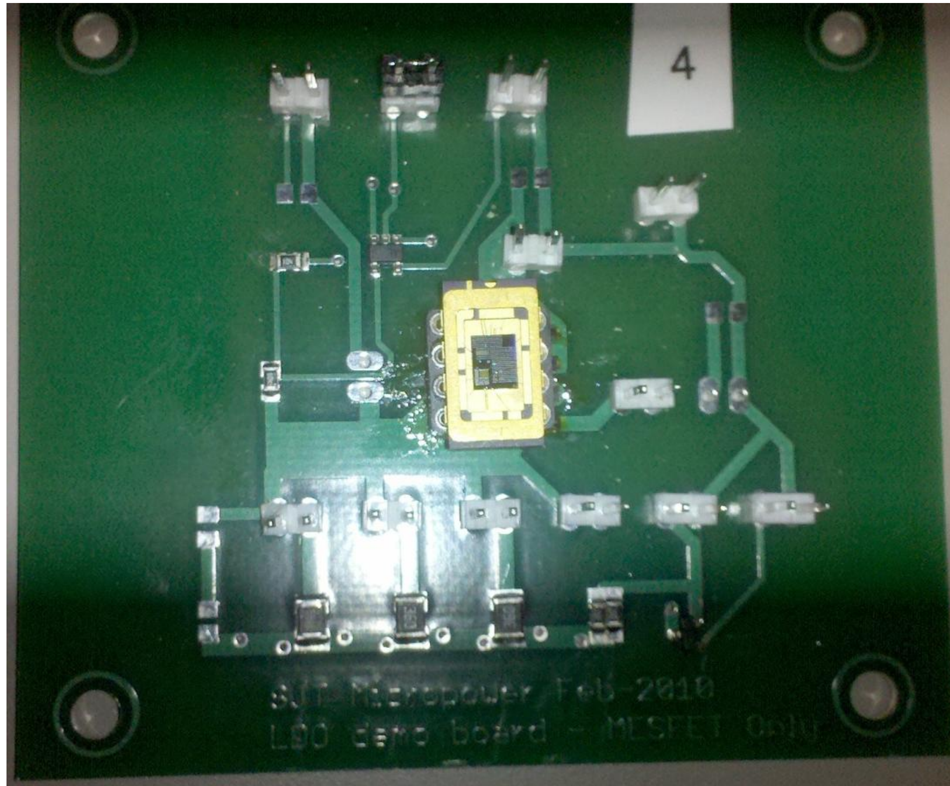

Fig. 64. PCB test board for the PD-MESFET LDO.

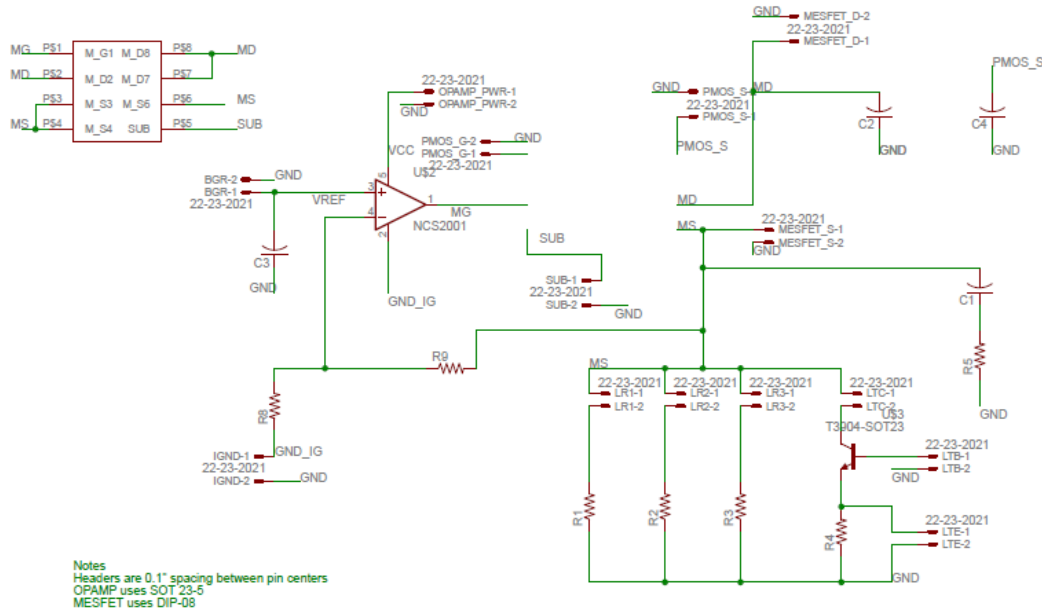

Fig. 65. Schematic of PCB board used to test the PD-MESFET LDO.

5.2. *MESFET Pass Transistor Characteristics*

The potential of the PD-MESFET to the LDO is evident in the Gummel plot shown in Fig. 66. At a drain bias of 20 mV this particular device can produce over 80 mA at $V_{GS} = 0$ V and will contribute < 8 μA to the ground current under its worst operating condition at room temperature. Since the device is well within its linear region, the drain current will continue to grow linearly with drain voltage. Gate leakage current will also grow, but at a drain bias of 500 mV the current will still be < 20 μA (not shown).

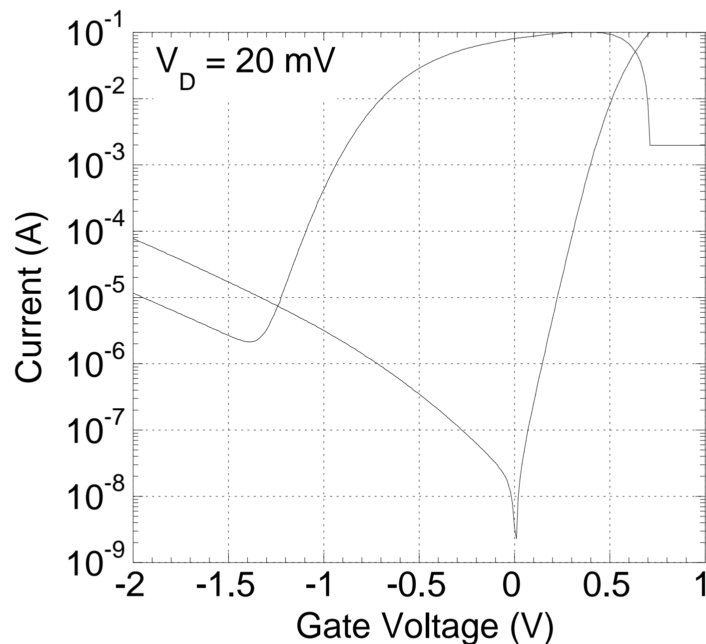

Fig. 66. Gummel plot of bonded out PD-MESFET pass transistor.

With the FOC plot hitting the HP4155B's compliance fairly quickly (Fig. 67a), the output characteristics of the pass transistor cannot be seen, however, the on resistance, R_{on}, can still be extracted. At V_{GS} = 0 V, R_{on} is ~240 mΩ which corresponds to ~96 mΩ/mm^2. In reality R_{on} is less than 240 mΩ since that figure includes the resistance of the DIP-8 package leads and the long bondwires. These parasitics are unavoidable for all LDOs, but with an appropriately sized package, the bondwires could be made a fraction of their current size.

Fig. 67b shows the FOC out to 5 V for a MESFET exactly 1/28 the size (W = 4.26 mm) of the pass transistor. A soft breakdown begins to appear at ~4V which is more than twice the maximum safe operating voltage of the SOI CMOS (1.95V). Neglecting the parasitic resistances from the long metal lines of the pass transistor and the corresponding voltage drops, it can be expected that the pass

transistor will have a drain current roughly 28x larger than Fig. 67b. The gate current should also scale proportionately.

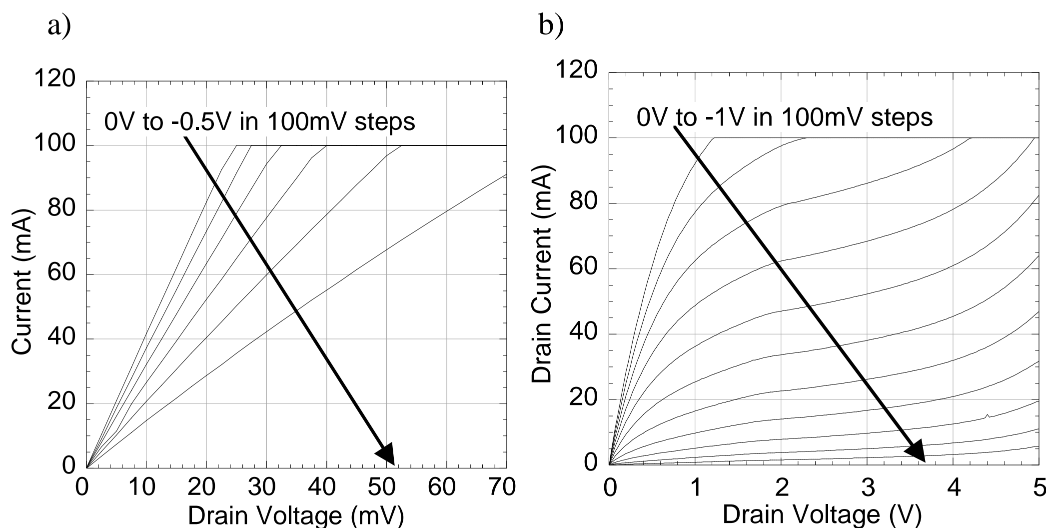

Fig. 67. a) FOC for MESFET pass transistor. b) FOC of MESFET that is 1/28 the size of the pass transistor.

5.3. PD-MESFET LDO RESULTS

Unlike the FD-MOSFET LDO in Chapter 4 (Fig. 56), the worst case ground current for this LDO occurs at no load. This will generally be the case for FD or PD-MESFET LDOs. In each type of MESFET the slope of the Schottky gate leakage curve increases with decreasing V_{GS}. As the load becomes easier for the MESFET to the drive, the feedback of the LDO will begin to shut the MESFET off and push the bias point of the MESFET to higher position on the gate leakage curve. This is analogous to the effect that increasing input voltage has on the LDO (explained in *Section 4.5*).

The LDO in Chapter 4 is more the exception due to the configuration of the shunt feedback buffer that it employs. The buffer began to dominate the ground current as load current became larger. It needed a special buffer like that to drive the large gate leakage of the FD-MESFET. With the gate leakage current of the PD-MESFET in Fig. 66 contributing less than 10 μA for drain voltages less than 200 mV it can use a more simple and traditional buffer. In fact, for load and line conditions which bias the MESFET with a V_{GS} between -0.5 and 0 V, the gate current becomes < 1 μA and is essentially negligible compared to the other components which contribute to the ground current. This is evident in Fig. 68 which shows the ground current peaking at a load current of 0 mA and essentially becoming constant after the load becomes greater 5 mA at 25°C. The capacitive constraints on the buffer are also significantly reduced for the PD-MESFET since a much smaller transistor is needed to achieve the same current drive.

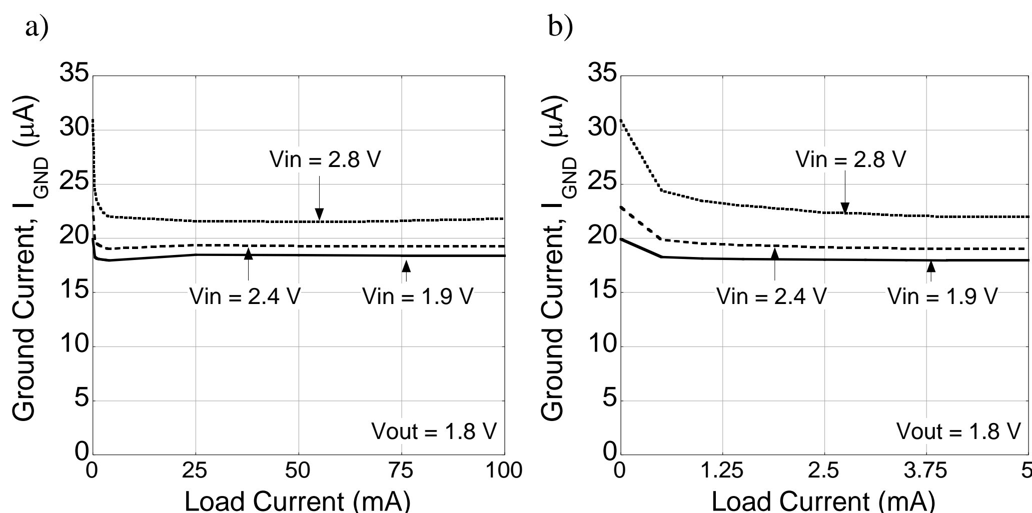

Fig. 68. a) Ground current with the low I_q error amplifier. b) Ground current with the low I_q error amplifier at light loads.

As was the case for the LDO in Chapter 4, this LDO shows fast and stable recovery for both the line and load transient response (Fig. 69-Fig. 72) without an output capacitor. The line and load for the low I_q error amplifier recovers in < 15 μs while the moderate I_q error amplifier's expanded gain bandwidth allows it to recover in 2 μs or less. The larger transient spikes in the low I_q error amplifier design can be attributed to the error amplifier's slower slew rate. This can be expected given its much lower I_q. The slew rate issue becomes very evident in capacitor less LDO regulators particularly at fast transients [40].

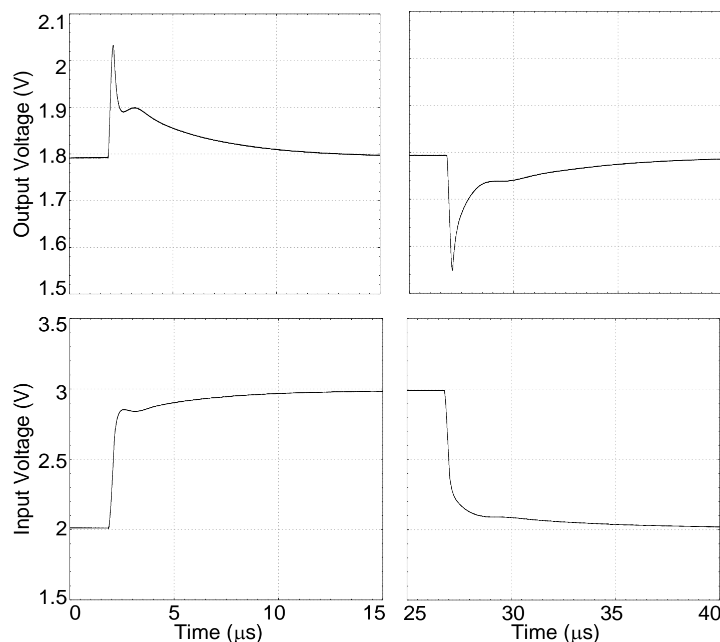

Fig. 69. Transient line regulation with the low I_q error amplifier. I_{out} = 50 mA, $t_r = t_f$ = 200 ns and T = 50 μs.

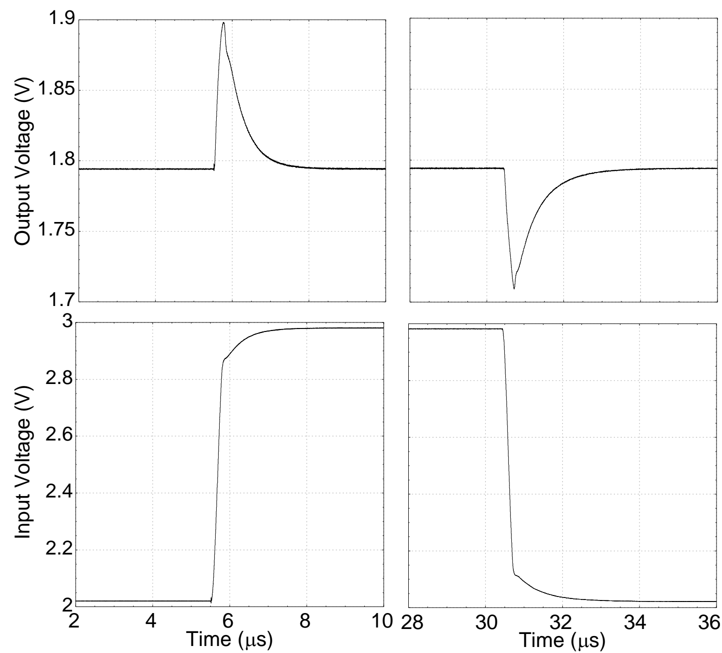

Fig. 70. Transient line regulation with the moderate I_q error amplifier. I_{out} = 50 mA, $t_r = t_f$ = 200 ns and T = 50 μs.

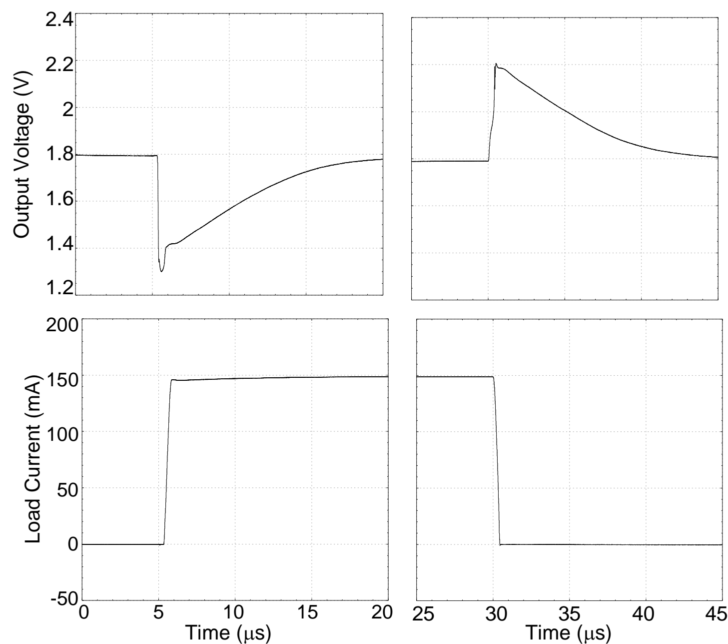

Fig. 71. Transient load regulation with the low I_q error amplifier. V_{in} = 2.4 V, t_r = t_f = 500 ns and T = 50 μs.

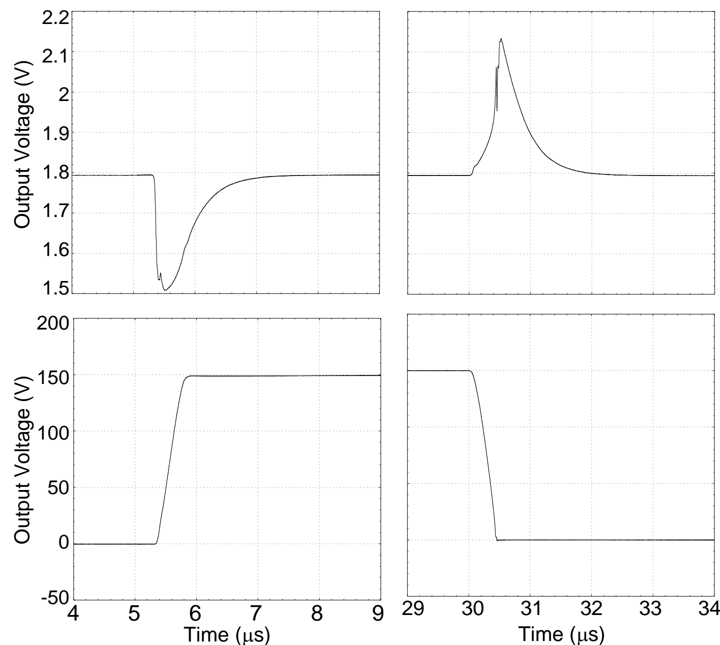

Fig. 72. Transient load regulation with the moderate I_q error amplifier. V_{in} = 2.4 V, $t_r = t_f$ = 500 ns and T = 50 μs.

5.4. *PD-MESFET LDO RESULTS ACROSS TEMPERATURE*

The PD-MESFET LDO was measured from -50 to +150°C and showed excellent characteristics across the entire range. A temperature controlled oven provided the measurements between 25 and 150°C while a probe station with a cooled stage was used for the -50°C measurement. As shown in Fig. 73, Fig. 74, and Fig. 87-Fig. 89 (refer to Appendix C) the output voltage changed only minimally under different line, load, and temperature conditions. It should be noted though, these numbers are extremely overly optimistic since the voltage reference was a precision voltage source that was maintained at room temperature. If this were an integrated LDO with a finely designed voltage

reference, 1 to 2% accuracy would be much realistic across this temperature range.

Other characters including the dropout voltage (Fig. 75) and the transient line and load (Fig. 90-Fig. 93 in Appendix C) stayed roughly the same at -50, 25, and +150°C. The only major difference was the ground current (Fig. 76). This comes as no surprise since the Schottky gate structure of the MESFET has a temperature dependence (refer to Equation 1.5 and Fig. 7). From Fig. 76 it can seen that a reasonable ground current can still be maintained if the input voltage is close to the output voltage; however, it does increase significantly as the input voltage increases which also expected based on the discussion in *Section 5.3*.

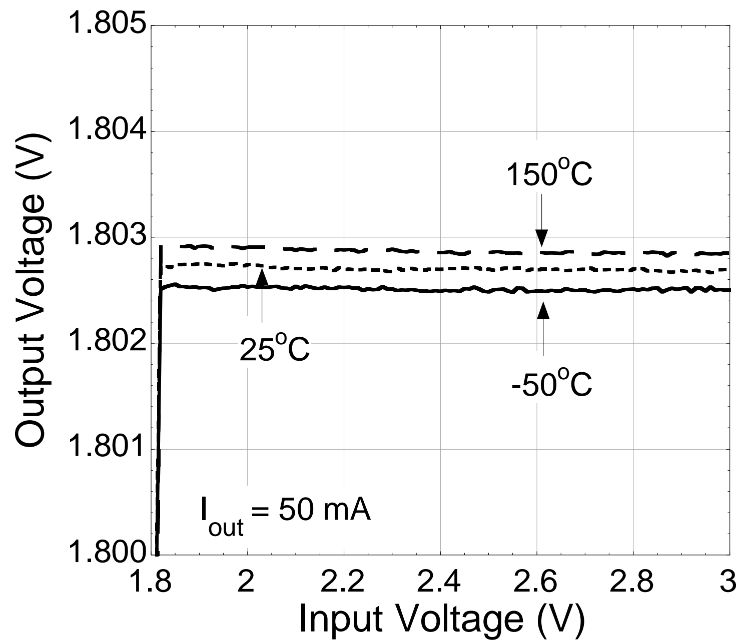

Fig. 73. Line regulation at -50, 25, and +150°C at a load of 50 mA.

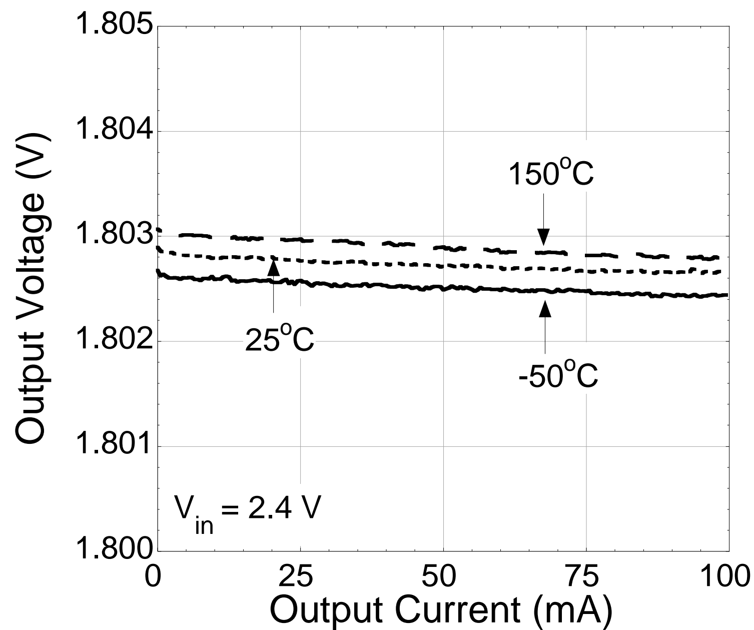

Fig. 74. Load regulation at -50, 25, and +150°C at a V_{in} = 2.4 V.

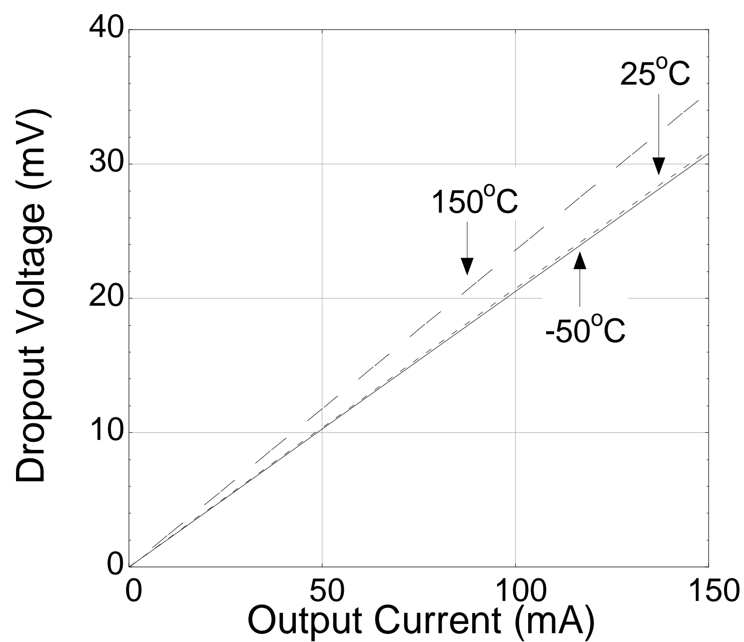

Fig. 75. The dropout voltage was measured up to 100 mA for -50, 25, and +150°C and extrapolated from 100 to 150 mA.

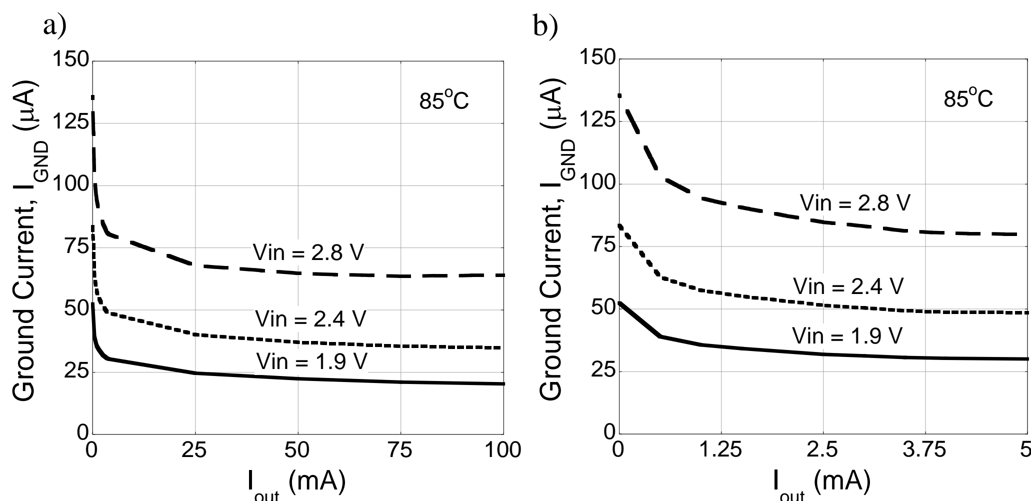

Fig. 76. a) Ground current at 85°C with the low I_q error amplifier. b) Ground current at 85°C with the low I_q error amplifier at light loads.

5.4. *Low Voltage Opportunities and Body Bias Effects*

With the goal of lowering the overall power consumption of power management systems, industry has been pushing for LDOs with lower dropout and output voltages. For PMOS LDOs this brings up a challenge. Typically their dropout voltage becomes noticeably worse as the output voltage scales below 1.5 V [41-42]. That is a result of the error amplifier running out of headroom to drive the gate of the PMOS, which in turn causes an increase in the on resistance and consequently a rise in the dropout voltage. Thus this counteracts some of the benefits of moving down to lower voltages.

For a PD N-MESFET pass device, the performance should improve since lowering the output voltage will decrease the body effect on the transistor. This is evident in Fig. 77 which compares a MESFET pass device under zero body effect

(V_{BS} = 0 V) and at V_{BS} = -1.8 V. The latter is the equivalent to what the MESFET sees when the LDO is at an output of 1.8 V. Without the body effect it is clear the device turns on earlier and has a higher drive current at V_{GS} = 0 V. Using this idea, it is possible to improve the performance of the dropout by tying the source (V_{out}) to the substrate. From Fig. 78 it can be seen that this leads to roughly a 10% improvement. The amount of improvement will be dependent on the MESFET's sensitivity to body effect which is related to the thickness of the insulating layer. On the Honeywell 150 nm process, the oxide was about 1 μm. It should be noted though that biasing the substrate might affect the operation of the CMOS. Also the dropout results are slightly different in Fig. 78 and Fig. 75 since a different bonded MESFET pass device was used. Lastly, while this might be an effective method for PD-MESFETs, FD-MESFETs cannot be improved in this manner since the silicon channel below the gate is fully depleted under all biasing conditions and is unaffected by body effect.

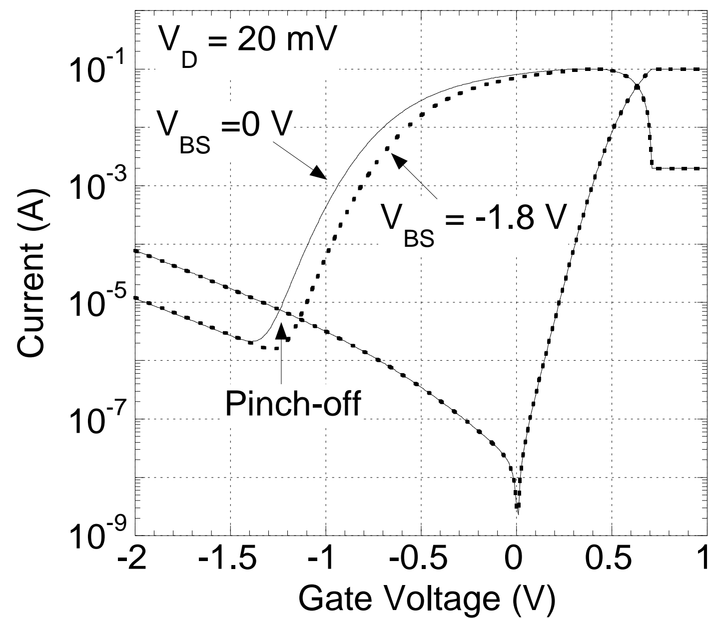

Fig. 77. Compares the MESFET pass transistor at two different bulk-to-source voltages.

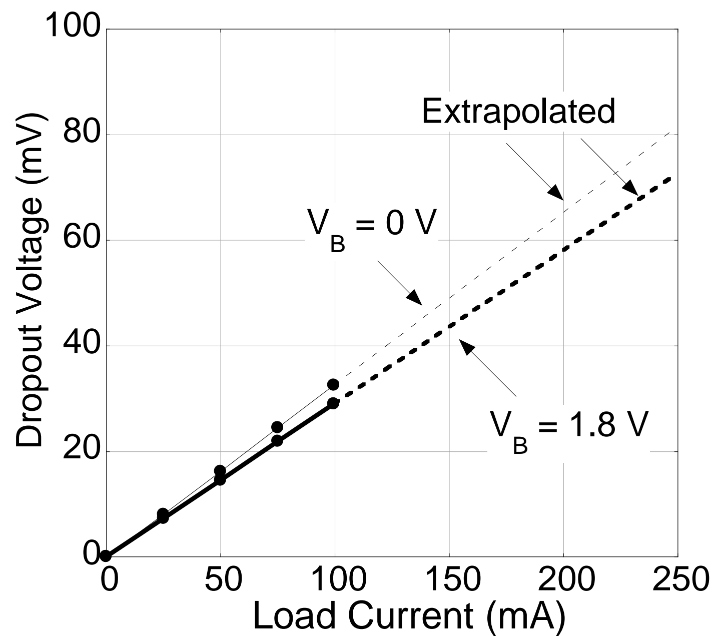

Fig. 78. Compares the dropout voltage when the substrate of the MESFET is biased at 0 V and 1.8 V.

Although the drive current improves as the output voltage scales there is a practical limitation on how low it can it go. That value is determined by the MESFET's pinch-off voltage. In order to limit the amount of conducting current during no load or very light load conditions, enough headroom needs to be allocated so that a large enough negative V_{GS} can be generated across the MESFET's gate-to-source junction to pinch it off. Based on that, the lowest output voltage for this particular MESFET would be ~1.25 V. However if a lower output voltage is needed, a MESFET with a slightly larger gate length and one which is less affected by short channel effects can be used. In Fig. 16 it can be seen that MESFETs on the same process had threshold voltage as low as -0.4 V. The other option would be to reduce the thickness of the thin silicon channel (Fig. 26). Both these options though would depress the pass transistor's current drive per die area and lead to a higher dropout voltage. Nevertheless, either option might be more attractive for very low voltage applications than the traditional PMOS LDO topology.

5.5. Radiation Effects On MESFET LDO

The MESFET has a natural tolerance to radiation due to its Schottky gate structure which is less susceptible to radiation damage than the MOS gate of a CMOS transistor. Unfortunately, while the gate can avoid significant damage, the spacers used for the access regions and the buried oxide layer will be affected in the form of induced positive trapped charge. This as result will cause an influx of

electrons to travel away from the heavily doped source and drain regions and into the channel region to balance out the positive trapped charge. Consequently, the device sees a negative threshold shift since a more negative gate bias is now needed to fully deplete the channel and pinch it off [43]. This is confirmed in Fig. 79 which shows the Gummel plot of the MESFET before and after radiation. An unintended yet positive consequence of this is the dropout voltage (Fig. 94 in Appendix D) will drop slightly with the device being able to be turned on harder at V_{GS} = 0 V. Predictably the increased leakage can be attributed to the extra electrons in the silicon channel after radiation.

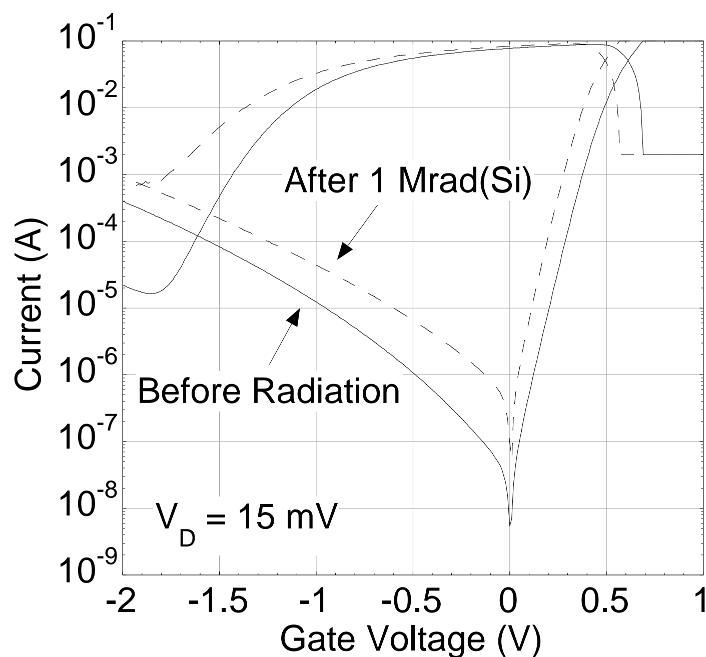

Fig. 79. Compares the Gummel plot of MESFET pass device after an exposure dose of 1 Mrad(Si).

With the expectation of the ground current incrementally rising with exposure dose, the operation of the PD-MESFET LDO was fairly constant

through 100 krad(Si) (Fig. 80-Fig. 82). For 200 krad(Si) and up, the LDO continued to regulate but showed noticeable degradation at higher input voltages and light loads. The transient line and load regulation (Fig. 95-Fig. 96 in Appendix D shown at 1 Mrad(Si)) was measured at each dose with biases of V_{in} = 2.4 V and I_{out} = 50mA respectively and showed minimal change. Based on the results from the DC line and load regulation in Fig. 80 and Fig. 81 this is not too surprising. After one week of annealing at room temperature the LDO showed little affect from the radiation exposure other than the elevated ground current (Fig. 97-Fig. 98).

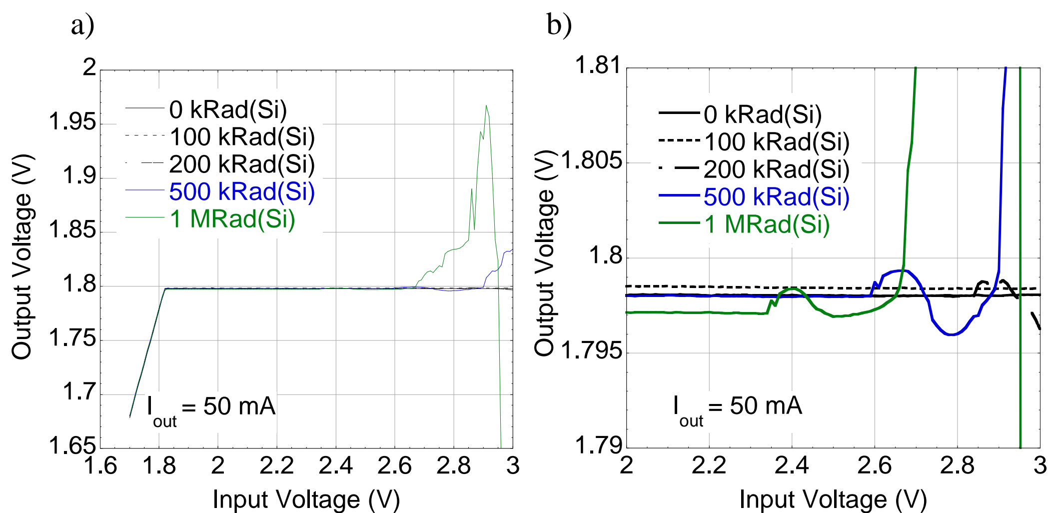

Fig. 80. a) DC line regulation at various cumulative radiation exposures. b) Zoom in of Part a).

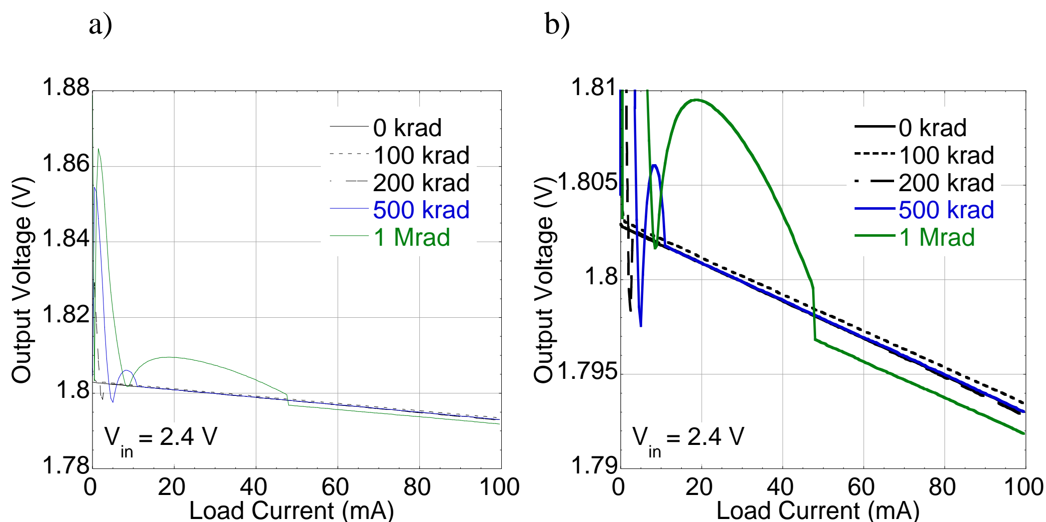

Fig. 81. a) DC load regulation at various cumulative radiation exposures. b) Zoom in of Part a).

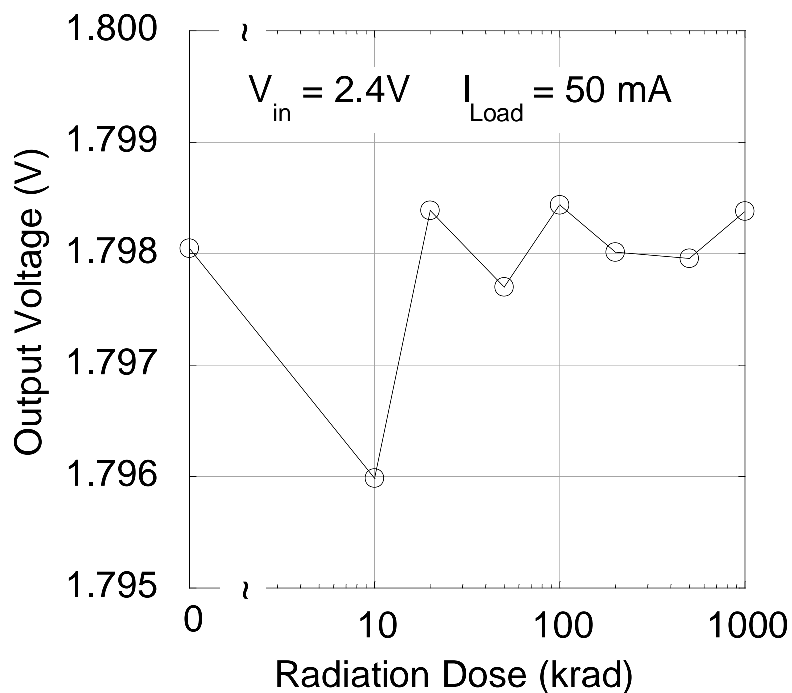

Fig. 82. The output voltage of the PD-MESFET LDO at cumulative radiation doses of 10, 20, 50, 100, 200, 500, and 1000 krad(Si).

For background purposes a MDS Nordion Gammacell 220 Co^{60} source was used to conduct the radiation tests. Tests took place over a two day period and the dose rate was approximately 0.9 krad(Si/minute). Measurements for DC line and load regulation, transient line and load regulation, and noise were taken after cumulative doses of 10, 20, 50, 100, 200, 500, and 1000 krad(Si). Each set of tests lasted roughly one hour. Upon completion, the MESFET was immediately put back in the Co^{60} source to mitigate the effects of room temperature annealing. Since the LDO was a board level design filled with non-radiation hardened surface mount components, only the MESFET was exposed. The DIP-8 package was left without a protective lid or epoxy coating as to not block or absorb the radiation dose and each pin was grounded during exposure. It should be noted that the radiation results for this particular MESFET should be further enhanced since the 150 nm SOI Honeywell process is a radiation hard process. Radiation tests were also performed on the FD-MESFET LDO from Chapter 4 but due to a confidentiality agreement with Peregrine Semiconductor those results cannot be made public. It can be said though that the LDO was still regulating after 1 Mrad(Si). For more radiation results on ASU MESFETs please refer to [43-44].

5.6. CONCLUSION

With these promising preliminary results, the next phase for the PD-MESFET is to complete a fully integrated design similar to the one in Chapter 4 on the Honeywell 150nm SOI CMOS process. Ideally the performance will

improve with respect to the transient responses and ground current since the error amplifier can be optimally designed to meet the needs of the MESFET LDO. Moreover with its ultra-low dropout voltage and capacitor free operation, this LDO appears to be a good fit for high current system-on-chip designs where the LDO consumes considerable die space and applications where very low dropout is needed to preserve battery lifetime. Additionally the LDO shows excellent promise for extreme environment electronics.

CHAPTER 6

CONCLUSION

As it was shown in the first four chapters, MESFETs can be integrated on commercial SOI or SOS CMOS processes without altering the fabrication flow or adding additional process steps. Thus, they are available to these processes free of cost. As evident by the LDO examples in Chapter 4 and 5, their unique characteristics can make them a very effective complement to CMOS technologies to increase performance and/or lower costs for certain analog circuits. The LDO benefited from the MESFET's depletion mode operation as it allowed it to implement an n-channel pass transistor without allocating precious die space for a charge pump. Meanwhile with the MESFET's seamless ability to integrate with CMOS it allowed for the rest of the building blocks to be designed with the low power CMOS.

6.1. Optimizing MESFET Pass Transistor

Moving forward, a key to widening the appeal of the N-MESFET LDO will be to reduce the gate leakage current. While it was not mentioned in Chapter 2, one of the small improvements made on the 150 nm Honeywell process was leaving the active silicon under the extended gate region and the edges of the MESFET for the structure in Fig. 13 at the intrinsic doping level to limit leakage paths. The reduction in gate current is evident in Fig. 15a and b particularly for the two L_g = 400 nm devices.

Another key will be minimizing parasitics to lower the dropout voltage. This is particularly important for high current applications where the voltage drops from the parasitics can dominate the dropout of the MESFET pass transistor. One mistake that was made for the MESFET pass transistor in Chapter 5 was using only a single via per finger on the drain end to bring the current up to the higher metal layers (refer to Appendix E for 3-D pictures of the PD-MESFET layout). Putting multiple vias down the entire finger would have expanded the drain metal line slightly, but it mostly likely would have been offset by the lower resistance of the finger. Moreover having additional vias should improve the reliability of the device since all the current for each finger as it is now flows through a single via stack.

Finding the optimal finger length and metal bus lines will also be important in reducing parasitics. For this layout, fingers of 10 µm were used since that was the finger size of the devices in Chapter 2. Once again, that was left unchanged to minimize risk. The drain bus line was then run over the device and a source line of about equal size was run below the device. This more than likely is not an efficient use of die space. Probably a better solution is to increase the finger lengths somewhere between 25 and 100 µm and stack the first 2 or 3 metals layers with minimally spaced vias on each of the source and drain fingers. Then with the area above the MESFET, source and drain bus lines can be routed with the top 3 or 4 metal layers. With this method, almost all of the die would be allocated to the pass device instead of about half of it. To optimally design the

MESFET though, a model of the interconnects would eventually need to be developed. Depending on the current rating of the LDO, the optimal routing scheme may differ especially at high currents where the pass transistor can become very large.

6.2. Future LDO Opportunities

Assuming a Phase 2 project is approved by NASA, two fully integrated LDOs based on the MESFET in Chapter 5 will be designed for current ratings of 100 mA and 1 A. While these designs will hopefully have results that will rival start-of-art LDOs, the potential end customers will likely be limited to NASA and other government agencies or suppliers who are willing to spend a premium for Honeywell's radiation hardened process. To expand the N-MESFET LDO concept to commercial consumers, plans are on order for a design on IBM's 180 nm SOI CMOS process. Since this process has not yet been used for the ASU MESFETs it is likely that an array of marginally sized MESFETs with varying access and gate lengths will be laid out on the first design run to figure out the optimal structure. With the lithography rules being more stringent towards the silicide block layer, devices might include access regions created by the polysilicon layer (refer to *Section 3.4*) to reduce the gate and access lengths. If all goes well, a fully integrated design would be made on an ensuing run. Lastly there is a possibility for the MESFET to be on the IBM 45 nm SOI CMOS process.

6.3. *Other Potential Applications For MESFETs*

While the MESFET used as a pass transistor and configured in a source follower has significant commercial appeal for LDOs, its potential for other military or space related electronics may be even more. From *Sections 5.4 and 5.5* and Appendix C and D the MESFET was shown to still operate for the LDO in harsh environment conditions ranging from -50 to 150°C (eventually though the goal is to expand the temperature range to -150 to +150°C which appears to be very achievable based on previous MESFET measurements on other processes) and radiation doses up to 1 Mrad(Si). Moreover, with the low volume numbers and tight restrictions required for both military and space circuits, agencies such as NASA and DARPA are limited in the number of government approved fabrication suppliers they can go to. They are furthered limited by the available options for high voltage transistors. MESFETs offer one such solution to this issue by providing a cost free way to fabricate high voltage devices on commercial SOI and SOS CMOS processes. Chapter 1 shows the best example of this with MESFETs achieving breakdowns in excess of 50 V on a 350 nm PD-SOI CMOS process (Fig. 9). More recently it was shown in Chapter 2 that MESFETs with the same device structure achieved up to 12 V breakdowns from the same supplier on their 150 nm process (Fig. 24). In each case the maximum steady-state operating voltage rating was 3.5 and 1.95 V respectively. Lastly, the highest measured breakdown on the FD-SOS Peregrine process was 17 V; however, little effort was made with varying the access lengths to achieve the

highest possible breakdown leading to the belief that much higher breakdowns are possible.

One such application that will be looked at in the future work is incorporating the MESFET as a switching transistor in buck and boost regulators for space applications. MESFETs like the one in Fig. 25 seem ideal for those applications with its good combination in breakdown, peak f_T, and current drive. As was the case with the N-MESFET LDO, a very simple switching architecture will mostly likely be chosen first with most of the design focused on modeling and optimizing the MESFET for this particular application. Other possibilities include using the MESFET in a high voltage cascaded power amplifier or low noise amplifier.

6.4. CONCLUSION

This thesis has shown that while the current MESFETs and their corresponding models are advanced enough to design MESFET based circuits; there is still a long ways to go in optimizing their design and layout. Continued research and ensuing fabrication runs are still needed to thoroughly test new structures like those presented in Fig. 36 and Fig. 38. It should be noted again that while those structures appear to improve the overall performance on Peregrine's GC process they may not be the most appropriate structure for their latest process line. This nicely brings up a critical issue in MESFET design which is the fabrication steps, layers, and layout rules are generally centered on improving the

performance of the CMOS. A pivotal layer to the MESFET like the silicide block for example has no effect on standard CMOS transistors and may not be a priority when devising a process or scaling it down. As result, the optimum layout and structure will vary from process to process. Thus new ideas on how to create the access lengths or orientate the gate will continually be needed to ensure the MESFET's performance scales with feature size.

REFERENCES

[1] J. Ervin, A. Balijepalli, P. Joshi, J. Yang, V. Kushner, and T. J. Thornton, "CMOS-Compatible SOI MESFETs With High Breakdown Voltage," *IEEE Transactions on Electron Devices,* vol. 53, pp. 3129-3135, 2006.

[2] W. Lepkowski, S. J. Wilk, N. Summers, T. J. Thornton, and P. Fechner, "Scaling SOI MESFETs to 150 nm CMOS Technologies," *submitted to IEEE Transactions on Electron Devices,* 2010.

[3] J. Yang, A. Balijepalli, T. J. Thornton, J. Vandersand, B. J. Blalock, M. E. Wood, and M. Mojarradi, "Silicon-Based Integrated MOSFETs and MESFETs: A New Paradign for Low Power, Mixed Signal, Monolithic Using Commercially Available SOI," *International Journal of High Speed Electronics and Systems,* pp. 1-10, 2005.

[4] K. P. MacWilliams and J. D. Plummer, "Device Physics and Technology of Complementary Silicon MESFET's for VLSI Applications," *IEEE Transactions on Electron Devices* vol. 38, pp. 2619-2631, 1991.

[5] H. Vogt, G. Burbach, J. Belz, and G. Zimmer, "MESFETs in Thin Silicon on SIMOX," *Electronics Letters,* vol. 25, pp. 1580-1581, 1989.

[6] D. P. Vu and A. Sono, "Self-Aligned Si MESFETs Fabricated in Thin Silicon-on-Insulator Films," *Electronics Letters,* vol. 23, pp. 354-355, 1987.

[7] M. Berroth and R. Bosch, "High-Frequency Equivalent Circuit of GaAs FETs for Large-Signal Applications," *IEEE Transactions on Microwave Theory and Techniques,* vol. 39, pp. 224-229, 1991.

[8] D. Corson and P. Delatte, "Why all the buzz about SOI?," *RF Design*, pp. 36-40, Oct 1, 2003.

[9] T. J. Thornton, "Physics and Applications of the Schottky Junction Transistor," *IEEE Transactions on Electron Devices,* vol. 48, pp. 2421-2427, 2001.

[10] A. Balijepalli, "Compact Modeling and Applications of a PD SOI MESFET," Ph.D Thesis, Arizona State University-Tempe, 2007.

[11] A. Balijepalli, J. Ervin, P. Joshi, J. Yang, Y. Cao, J. Kriz, G. Hughes, and T. J. Thornton, "Characterization and Spice Model Extraction for a High-Voltage, CMOS Compatible SOI MESFET," presented at the IEEE Transactions on Microwave Theory and Techniques, 2005.

[12] J. Ervin, "Fabrication and Characterization of SOI MESFETs," Ph.D Thesis, Arizona State University-Tempe, 2007.

[13] A. Shanmugam, "Analog Circuits Using SOI MESFETs," Electrical Engineering, M.S. Thesis, Arizona State University-Tempe, 2007.

[14] R. F. Pierret, *Semiconductor Device Fundamentals*, Addison-Wesley, 1996.

[15] J. Y. Spann, P. Jaconelli, Z. Wu, T. J. Thornton, W. T. Kemp, and S. J. Sampson, "The Schottky Junction Transistor - A Contender for Ultralow-Power Radiation-Tolerant Space Electronics," presented at the IEEE Proceedings Aerospace Conference 2003.

[16] T. J. Thornton, "Physics and Applications of the Schottky Junction Transistor," *IEEE Transactions on Electron Devices,* vol. 48, pp. 2421-2427, 2001.

[17] R. J. Baker, *CMOS Circuit Design, Layout, and Simulation*, 2nd ed., Hoboken, NJ: John Wiley & Sons, 2008.

[18] D. A. Johns and K. Martin, *Analog Integrated Circuit Design*, John Wiley & Sons, 1997.

[19] C. Toumazou and D. G. Haigh, "Analogue Design Techniques For High Speed GaAs Operational Amplifiers," presented at the IEEE International Symposium on Circuits and Systems, 1988.

[20] C. Toumazou and D. G. Haigh, "Design of GaAs Operational Amplifiers for Analog Sampled Data Applications," *IEEE Transactions on Circuits and Systems* vol. 37, pp. 922-935, 1990.

[21] T. K. Chiang, Y. H. Wang, and M. P. Houng, "Modeling of threshold voltage and subthreshold swing of short-channel SOI MESFET's," *Solid-State Electronics,* pp. 123-129, 1999.

[22] "WinCal 3.1," Beaverton, OR: Cascade Microtech, Inc., 2002.

[23] A. Balijepalli, R. Vijayaraghavan, J. Ervin, J. Yang, S. K. Islam, and T. J. Thornton, "Large-Signal Modeling of SOI MESFETs," *Solid-State Electronics,* vol. 50, pp. 943-950, 2006.

[24] A. Balijepalli, J. Ervin, W. Lepkowski, Y. Cao, and T. J. Thornton, "Compact Modeling of a PD SOI MESFET for Wide Temperature Designs," *Microelectronics Journal,* vol. 40, pp. 1264-1273, 2009.

[25] S. R. Bahl and J. A. del Alamo, "A New Drain-Current Injection Technique for the Measurement of Off-State Breakdown Voltage in FETs," *IEEE Transactions on Electron Devices,* vol. 40, pp. 1558-1560, 1993.

[26] W. Lepkowski, S. J. Wilk, S.Kim, B. Bakkaloglu, and T. J. Thornton, "A Capacitor-Free LDO Using a FD Si-MESFET Pass Transistor," presented at the IEEE MWSCAS Conference, Cancun, Mexico, 2009.

[27] W. Lepkowski, S. J. Wilk, J. Ervin, and T. J. Thornton, "SOI MESFETs Fabricated Using Fully Depleted CMOS Technologies," *IEEE Electron Device Letters,* vol. 30, pp. 678-680, 2009.

[28] G. A. Garcia, R. E. Reedy, and M. L. Burgener, "High-Quality CMOS in Thin (100nm) Silicon on Sapphire," *IEEE Electron Device Letters,* vol. 9, pp. 32-34, 1988.

[29] S. M. Sze, *Physics of Semiconductor Devices*, 2 ed., New York: Wiley, 1981.

[30] Q. T. Zhao, F. Klinkhammer, M. Dolle, L. Kappius, and S. Mantl, "Nanometer patterning of epitaxial CoSi2/Si(100) for Ultrashort Channel Schottky Barrier Metal-Oxide-Semiconductor Field Effect Transistors," *Applied Physics Letters,* vol. 74, pp. 454-456, 1999.

[31] "Cadence Toolsuite : v5.1.0," San Jose, CA: Cadence Design Systems, Inc., 2010.

[32] R. B. Hallgren and P. H. Litzenberg, "TOM3 capacitance model: linking large- and small-signal MESFET models in SPICE," *IEEE Transactions Microwave Theory Techniques,* vol. 47, pp. 556-561, 1999.

[33] J. Yang, V. Kushner, A. Balijepalli, T. J. Thornton, J. Vandersand, B. J. Blalock, and M. E. Wood, "Integrated SOI MOSFETs and MESFETs," *Journal of High Speed Electronics,* Accepted for Publication.

[34] "TSP763xx-Q1: Low-Power 150-mA Low-Dropout Linear Regulators," Datasheet from Texas Instruments, 2004.

[35] D. Heisley and B. Wank, "DMOS delivers dramatic performance gains to LDO regulators," *EDN*, pp. 141-150, June 22, 2000.

[36] P. M. A. Fernandes, "High PSRR Low Dropout-out Voltage Regulator (LDO)," M.S. Thesis, Universidade Tecnica de Lisboa, 2009.

[37] G. A. Rincon-Mora, "Current Efficient, Low Voltage, Low Dropout-Out Regulators," Ph.D Thesis, Georgia Institute of Technology, 1996.

[38] V. Gupta and G. A. Rincon-Mora, "A 5mA 0.6um CMOS Miller-Compensated LDO Regulator with -27dB Worst-Case Power-Supply Rejection Using 60pF of On-Chip Capacitance," presented at the IEEE International Solid-State Circuits Conference, Feb. 11-15, 2007.

[39] M. Al-Shyoukh, H. Lee, and R. Perez., "A Transient-Enhanced Low-Quiescent Current Low-Dropout Regulator With Buffer Impedance Attenuation," *IEEE Journal of Solid-State Circuits,* vol. 42, pp. 1732-1742, 2007.

[40] R. J. Milliken, "A Capacitor-Less Low Drop-Out Voltage Regulator With Fast Transient Response," M.S. Thesis, Texas A&M University, 2005.

[41] "NCP585: Tri-Mode 300 mA CMOS LDO Regulator with Enable," Datasheet from ON Semiconductor, 2009.

[42] "NCP571: 150 mA CMOS Low Iq Low Output Voltage Regulator," Datasheet from ON Semiconductor, 2010.

[43] J. Spann, V. Kushner, T. J. Thornton, J. Yang, A. Balijepalli, H. J. Barnaby, X. J. Chen, D. Alexander, W. T. Kemp, S. J. Sampson, and M. E. Wood, "Total Dose Radiation Response of CMOS Compatible SOI MESFETs," *IEEE Transactions on Nuclear Science,* vol. 52, pp. 2398-2402, 2005.

[44] J. Spann, "Manufacturability and the characterization of the Schottky junction transistor," Ph.D. Thesis, Arizona State University-Tempe, 2005.

[45] "2N3904: General Purpose Transistors," Datasheet from ON Semiconductor, 2010.

[46] "NCS2001: 0.9 V, Rail−to−Rail, Single Operational Amplifier," Datasheet from ON Semiconductor, 2007.

[47] "LMP2231: Micropower, 1.6V, Precision Operational Amplifier with CMOS Inputs," Datasheet from National Semiconductor, 2010.

[48] "Google SketchUp 7.1," Mountain View, CA: Google Inc., 2008.

APPENDIX A

ELECTRICAL CHARACTERISTICS OF SURFACE MOUNT COMPONENTS USED ON PCB BOARDS FOR TESTING PD AND FD-MESFET LDO

2N3903, 2N3904

ELECTRICAL CHARACTERISTICS (T_A = 25°C unless otherwise noted)

Characteristic		Symbol	Min	Max	Unit
OFF CHARACTERISTICS					
Collector−Emitter Breakdown Voltage (Note 2) (I_C = 1.0 mAdc, I_B = 0)		$V_{(BR)CEO}$	40	–	Vdc
Collector−Base Breakdown Voltage (I_C = 10 μAdc, I_E = 0)		$V_{(BR)CBO}$	60	–	Vdc
Emitter−Base Breakdown Voltage (I_E = 10 μAdc, I_C = 0)		$V_{(BR)EBO}$	6.0	–	Vdc
Base Cutoff Current (V_{CE} = 30 Vdc, V_{EB} = 3.0 Vdc)		I_{BL}	–	50	nAdc
Collector Cutoff Current (V_{CE} = 30 Vdc, V_{EB} = 3.0 Vdc)		I_{CEX}	–	50	nAdc
ON CHARACTERISTICS					
DC Current Gain (Note 2)		h_{FE}			–
(I_C = 0.1 mAdc, V_{CE} = 1.0 Vdc)	2N3903		20	–	
	2N3904		40	–	
(I_C = 1.0 mAdc, V_{CE} = 1.0 Vdc)	2N3903		35	–	
	2N3904		70	–	
(I_C = 10 mAdc, V_{CE} = 1.0 Vdc)	2N3903		50	150	
	2N3904		100	300	
(I_C = 50 mAdc, V_{CE} = 1.0 Vdc)	2N3903		30	–	
	2N3904		60	–	
(I_C = 100 mAdc, V_{CE} = 1.0 Vdc)	2N3903		15	–	
	2N3904		30	–	
Collector−Emitter Saturation Voltage (Note 2)		$V_{CE(sat)}$			Vdc
(I_C = 10 mAdc, I_B = 1.0 mAdc)			–	0.2	
(I_C = 50 mAdc, I_B = 5.0 mAdc			–	0.3	
Base−Emitter Saturation Voltage (Note 2)		$V_{BE(sat)}$			Vdc
(I_C = 10 mAdc, I_B = 1.0 mAdc)			0.65	0.85	
(I_C = 50 mAdc, I_B = 5.0 mAdc)			–	0.95	
SMALL−SIGNAL CHARACTERISTICS					
Current−Gain − Bandwidth Product		f_T			MHz
(I_C = 10 mAdc, V_{CE} = 20 Vdc, f = 100 MHz)	2N3903		250	–	
	2N3904		300	–	
Output Capacitance (V_{CB} = 5.0 Vdc, I_E = 0, f = 1.0 MHz)		C_{obo}	–	4.0	pF
Input Capacitance (V_{EB} = 0.5 Vdc, I_C = 0, f = 1.0 MHz)		C_{ibo}	–	8.0	pF
Input Impedance		h_{ie}			k Ω
(I_C = 1.0 mAdc, V_{CE} = 10 Vdc, f = 1.0 kHz)	2N3903		1.0	8.0	
	2N3904		1.0	10	
Voltage Feedback Ratio		h_{re}			X 10^{-4}
(I_C = 1.0 mAdc, V_{CE} = 10 Vdc, f = 1.0 kHz)	2N3903		0.1	5.0	
	2N3904		0.5	8.0	
Small−Signal Current Gain		h_{fe}			–
(I_C = 1.0 mAdc, V_{CE} = 10 Vdc, f = 1.0 kHz)	2N3903		50	200	
	2N3904		100	400	
Output Admittance (I_C = 1.0 mAdc, V_{CE} = 10 Vdc, f = 1.0 kHz)		h_{oe}	1.0	40	μmhos
Noise Figure		NF			dB
(I_C = 100 μAdc, V_{CE} = 5.0 Vdc, R_S = 1.0 k Ω, f = 1.0 kHz)	2N3903		–	6.0	
	2N3904		–	5.0	
SWITCHING CHARACTERISTICS					
Delay Time	(V_{CC} = 3.0 Vdc, V_{BE} = 0.5 Vdc, I_C = 10 mAdc, I_{B1} = 1.0 mAdc)	t_d	–	35	ns
Rise Time		t_r	–	35	ns
Storage Time	(V_{CC} = 3.0 Vdc, I_C = 10 mAdc, I_{B1} = I_{B2} = 1.0 mAdc) 2N3903	t_s	–	175	ns
	2N3904		–	200	
Fall Time		t_f	–	50	ns

2. Pulse Test: Pulse Width ≤ 300 μs; Duty Cycle ≤ 2%.

Fig. 83. Electrical characteristics of the 2N3904 BJT. The 2N3094 was used with the Honeywell and Peregrine LDO to switch in a load for the load transient response. Refer to [45] for the complete datasheet.

MAXIMUM RATINGS

Rating	Symbol	Value	Unit
Supply Voltage (V_{CC} to V_{EE})	V_S	7.0	V
Input Differential Voltage Range (Note 1)	V_{IDR}	V_{EE} −300 mV to 7.0 V	V
Input Common Mode Voltage Range (Note 1)	V_{ICR}	V_{EE} −300 mV to 7.0 V	V
Output Short Circuit Duration (Note 2)	t_{Sc}	Indefinite	sec
Junction Temperature	T_J	150	°C
Power Dissipation and Thermal Characteristics SOT23−5 Package Thermal Resistance, Junction−to−Air Power Dissipation @ T_A = 70°C SC70−5 Package Thermal Resistance, Junction−to−Air Power Dissipation @ T_A = 70°C	 $R_{\theta JA}$ P_D $R_{\theta JA}$ P_D	 235 340 280 286	 °C/W mW °C/W mW
Operating Ambient Temperature Range NCS2001 NCV2001 (Note 3)	T_A	 −40 to +105 −40 to +125	°C
Storage Temperature Range	T_{stg}	−65 to 150	°C
ESD Protection at any Pin Human Body Model (Note 4)	V_{ESD}	2000	V

Stresses exceeding Maximum Ratings may damage the device. Maximum Ratings are stress ratings only. Functional operation above the Recommended Operating Conditions is not implied. Extended exposure to stresses above the Recommended Operating Conditions may affect device reliability.

1. Either or both inputs should not exceed the range of V_{EE} −300 mV to V_{EE} +7.0 V.
2. Maximum package power dissipation limits must be observed to ensure that the maximum junction temperature is not exceeded. $T_J = T_A + (P_D R_{\theta JA})$.
3. NCV prefix is qualified for automotive usage.
4. ESD data available upon request.

DC ELECTRICAL CHARACTERISTICS
(V_{CC} = 2.5 V, V_{EE} = −2.5 V, $V_{CM} = V_O$ = 0 V, R_L to GND, T_A = 25°C unless otherwise noted.)

Characteristics	Symbol	Min	Typ	Max	Unit
Input Offset Voltage V_{CC} = 0.45 V, V_{EE} = −0.45 V T_A = 25°C T_A = 0°C to 70°C T_A = −40°C to 125°C V_{CC} = 1.5 V, V_{EE} = −1.5 V T_A = 25°C T_A = 0°C to 70°C T_A = −40°C to 125°C V_{CC} = 2.5 V, V_{EE} = −2.5 V T_A = 25°C T_A = 0°C to 70°C T_A = −40°C to 125°C	V_{IO}	 −6.0 −8.5 −9.5 −6.0 −7.0 −7.5 −6.0 −7.5 −7.5	 0.5 − − 0.5 − − 0.5 − −	 6.0 8.5 9.5 6.0 7.0 7.5 6.0 7.5 7.5	mV
Input Offset Voltage Temperature Coefficient (R_S = 50) T_A = −40°C to 125°C	$\Delta V_{IO}/\Delta T$	−	8.0	−	μV/°C
Input Bias Current (V_{CC} = 1.0 V to 5.0 V)	I_{IB}	−	10	−	pA
Input Common Mode Voltage Range	V_{ICR}	−	V_{EE} to V_{CC}	−	V
Large Signal Voltage Gain V_{CC} = 0.45 V, V_{EE} = −0.45 V R_L = 10 k R_L = 2.0 k V_{CC} = 1.5 V, V_{EE} = −1.5 V R_L = 10 k R_L = 2.0 k V_{CC} = 2.5 V, V_{EE} = −2.5 V R_L = 10 k R_L = 2.0 k	A_{VOL}	 − − − − 20 15	 40 20 40 40 40 40	 − − − − − −	kV/V

Fig. 84. The electrical characteristics of the NCS2001 operational amplifier which was used as the moderate I_q error amplifier in the Honeywell LDO. Refer to [46] for the complete datasheet. The rest of the characteristics can be found on the next two pages.

DC ELECTRICAL CHARACTERISTICS (continued)
(V_{CC} = 2.5 V, V_{EE} = −2.5 V, V_{CM} = V_O = 0 V, R_L to GND, T_A = 25°C unless otherwise noted.)

Characteristics	Symbol	Min	Typ	Max	Unit
Output Voltage Swing, High State Output (V_{ID} = +0.5 V)	V_{OH}				V
V_{CC} = 0.45 V, V_{EE} = −0.45 V					
T_A = 25°C					
R_L = 10 k		0.40	0.494	–	
R_L = 2.0 k		0.35	0.466	–	
T_A = 0°C to 70°C					
R_L = 10 k		0.40	–	–	
R_L = 2.0 k		0.35	–	–	
T_A = −40°C to 125°C					
R_L = 10 k		0.40	–	–	
R_L = 2.0 k		0.35	–	–	
V_{CC} = 1.5 V, V_{EE} = −1.5 V					
T_A = 25°C					
R_L = 10 k		1.45	1.498	–	
R_L = 2.0 k		1.40	1.480	–	
T_A = 0°C to 70°C					
R_L = 10 k		1.45	–	–	
R_L = 2.0 k		1.40	–	–	
T_A = −40°C to 125°C					
R_L = 10 k		1.45	–	–	
R_L = 2.0 k		1.40	–	–	
V_{CC} = 2.5 V, V_{EE} = −2.5 V					
T_A = 25°C					
R_L = 10 k		2.45	2.498	–	
R_L = 2.0 k		2.40	2.475	–	
T_A = 0°C to 70°C					
R_L = 10 k		2.45	–	–	
R_L = 2.0 k		2.40	–	–	
T_A = −40°C to 125°C					
R_L = 10 k		2.45	–	–	
R_L = 2.0 k		2.40	–	–	
Output Voltage Swing, Low State Output (V_{ID} = −0.5 V)	V_{OL}				V
V_{CC} = 0.45 V, V_{EE} = −0.45 V					
T_A = 25°C					
R_L = 10 k		–	−0.494	−0.40	
R_L = 2.0 k		–	−0.480	−0.35	
T_A = 0°C to 70°C					
R_L = 10 k		–	–	−0.40	
R_L = 2.0 k		–	–	−0.35	
T_A = −40°C to 125°C					
R_L = 10 k		–	–	−0.40	
R_L = 2.0 k		–	–	−0.35	
V_{CC} = 1.5 V, V_{EE} = −1.5 V					
T_A = 25°C					
R_L = 10 k		–	−1.493	−1.45	
R_L = 2.0 k		–	−1.480	−1.40	
T_A = 0°C to 70°C					
R_L = 10 k		–	–	−1.45	
R_L = 2.0 k		–	–	−1.40	
T_A = −40°C to 125°C					
R_L = 10 k		–	–	−1.45	
R_L = 2.0 k		–	–	−1.40	
V_{CC} = 2.5 V, V_{EE} = −2.5 V					
T_A = 25°C		–			
R_L = 10 k		–	−2.492	−2.45	
R_L = 2.0 k			−2.479	−2.40	
T_A = 0°C to 70°C					
R_L = 10 k		–	–	−2.45	
R_L = 2.0 k		–	–	−2.40	
T_A = −40°C to 125°C					
R_L = 10 k		–	–	−2.45	
R_L = 2.0 k		–	–	−2.40	

DC ELECTRICAL CHARACTERISTICS (continued)
(V_{CC} = 2.5 V, V_{EE} = −2.5 V, V_{CM} = V_O = 0 V, R_L to GND, T_A = 25°C unless otherwise noted.)

Characteristics	Symbol	Min	Typ	Max	Unit
Common Mode Rejection Ratio (V_{in} = 0 to 5.0 V)	CMRR	60	70	–	dB
Power Supply Rejection Ratio (V_{CC} = 0.5 V to 2.5 V, V_{EE} = −2.5 V)	PSRR	55	65	–	dB
Output Short Circuit Current	I_{SC}				mA
V_{CC} = 0.45 V, V_{EE} = −0.45 V, V_{ID} = ±0.4 V					
Source Current High Output State		0.5	1.2	–	
Sink Current Low Output State		–	−3.0	−1.5	
V_{CC} = 1.5 V, V_{EE} = −1.5 V, V_{ID} = ±0.5 V					
Source Current High Output State		15	29	–	
Sink Current Low Output State		–	−40	−20	
V_{CC} = 2.5 V, V_{EE} = −2.5 V, V_{ID} = ±0.5 V					
Source Current High Output State		40	76	–	
Sink Current Low Output State		–	−96	−50	
Power Supply Current (Per Amplifier, V_O = 0 V)	I_D				mA
V_{CC} = 0.45 V, V_{EE} = −0.45 V					
T_A = 25°C		–	0.51	1.10	
T_A = 0°C to 70°C		–	–	1.10	
T_A = −40°C to 125°C		–	–	1.10	
V_{CC} = 1.5 V, V_{EE} = −1.5 V					
T_A = 25°C		–	0.72	1.40	
T_A = 0°C to 70°C		–	–	1.40	
T_A = −40°C to 125°C		–	–	1.40	
V_{CC} = 2.5 V, V_{EE} = −2.5 V					
T_A = 25°C		–	0.82	1.50	
T_A = 0°C to 70°C		–	–	1.50	
T_A = −40°C to 125°C		–	–	1.50	

AC ELECTRICAL CHARACTERISTICS
(V_{CC} = 2.5 V, V_{EE} = −2.5 V, V_{CM} = V_O = 0 V, R_L to GND, T_A = 25°C unless otherwise noted.)

Characteristics	Symbol	Min	Typ	Max	Unit
Differential Input Resistance (V_{CM} = 0 V)	R_{in}	–	> 1.0	–	tera Ω
Differential Input Capacitance (V_{CM} = 0 V)	C_{in}	–	3.0	–	pF
Equivalent Input Noise Voltage (f = 1.0 kHz)	e_n	–	100	–	nV/√Hz
Gain Bandwidth Product (f = 100 kHz)	GBW				MHz
V_{CC} = 0.45 V, V_{EE} = −0.45 V		–	1.1	–	
V_{CC} = 1.5 V, V_{EE} = −1.5 V		–	1.3	–	
V_{CC} = 2.5 V, V_{EE} = −2.5 V		0.5	1.4	–	
Gain Margin (R_L = 10 k, C_L = 5.0 pf)	Am	–	6.5	–	dB
Phase Margin (R_L = 10 k, C_L = 5.0 pf)	φm	–	60	–	°
Power Bandwidth (V_O = 4.0 V_{pp}, R_L = 2.0 k, THD = 1.0%, A_V = 1.0)	BW_P	–	80	–	kHz
Total Harmonic Distortion (V_O = 4.0 V_{pp}, R_L = 2.0 k, A_V = 1.0)	THD				%
f = 1.0 kHz		–	0.008	–	
f = 10 kHz		–	0.08	–	
Slew Rate (V_S = ±2.5 V, V_O = −2.0 V to 2.0 V, R_L = 2.0 k, A_V = 1.0)	SR				V/μs
Positive Slope		1.0	1.6	6.0	
Negative Slope		1.0	1.6	6.0	

1.8V DC Electrical Characteristics

(Note 4) Unless otherwise specified, all limits guaranteed for T_A = 25°C, V+ = 1.8V, V− = 0V, V_{CM} = V_O = V+/2, and R_L > 1 MΩ. **Boldface** limits apply at the temperature extremes.

Symbol	Parameter	Conditions	Min (Note 6)	Typ (Note 5)	Max (Note 6)	Units
V_{OS}	Input Offset Voltage			±10	±230 **±325**	μV
TCV_{OS}	Input Offset Voltage Drift	LMP2231A		±0.3	±0.4	μV/°C
		LMP2231B		±0.3	±2.5	
I_{BIAS}	Input Bias Current			0.02	±1.0 **±50**	pA
I_{OS}	Input Offset Current			5		fA
CMRR	Common Mode Rejection Ratio	0V ≤ V_{CM} ≤ 0.8V	76 **75**	92		dB
PSRR	Power Supply Rejection Ratio	1.6V ≤ V+ ≤ 5.5V V− = 0V, V_{CM} = 0V	83 **83**	120		dB
CMVR	Common Mode Voltage Rang	CMRR ≥ 76 dB CMRR ≥ 75 dB	−0.2 **0**		1.0 **1.0**	V
A_{VOL}	Large Signal Voltage Gain	V_O = 0.3V to 1.5V R_L = 10 kΩ to V+/2	103 **103**	120		dB
V_O	Output Swing High	R_L = 10 kΩ to V+/2 V_{IN}(diff) = 100 mV		12	50 **50**	mV from either rail
	Output Swing Low	R_L = 10 kΩ to V+/2 V_{IN}(diff) = −100 mV		13	50 **50**	
I_O	Output Current (Note 7)	Sourcing, V_O to V− V_{IN}(diff) = 100 mV	2.5 **2**	5		mA
		Sinking, V_O to V+ V_{IN}(diff) = −100 mV	2 **1.5**	5		
I_S	Supply Current			10	14 **15**	μA

1.8V AC Electrical Characteristics

(Note 4) Unless otherwise is specified, all limits guaranteed for T_A = 25°C, V+ = 1.8V, V− = 0V, V_{CM} = V_O = V+/2, and R_L > 1 MΩ. **Boldface** limits apply at the temperature extremes.

Symbol	Parameter	Conditions		Min (Note 6)	Typ (Note 5)	Max (Note 6)	Units
GBW	Gain-Bandwidth Product	C_L = 20 pF, R_L = 10 kΩ			127		kHz
SR	Slew Rate	A_V = +1, C_L = 20 pF R_L = 10 kΩ	Falling Edge		58		V/ms
			Rising Edge		48		
θ_m	Phase Margin	C_L = 20 pF, R_L = 10 kΩ			70		deg
G_m	Gain Margin	C_L = 20 pF, R_L = 10 kΩ			25		dB
e_n	Input-Referred Voltage Noise Density	f = 1 kHz			60		$nV/\sqrt{Hz}$
	Input-Referred Voltage Noise	0.1 Hz to 10 Hz			2.4		μV_{PP}
i_n	Input-Referred Current Noise	f = 1 kHz			10		$fA/\sqrt{Hz}$
THD+N	Total Harmonic Distortion + Noise	f = 100 Hz, R_L = 10 kΩ			0.005		%

Fig. 85. The electrical characteristics of the LMP2231 operational amplifier which was used as the low I_q error amplifier in the Honeywell LDO. Refer to [47] for the complete datasheet.

APPENDIX B

BARE DIE PICTURE OF LARGE PASS DEVICE

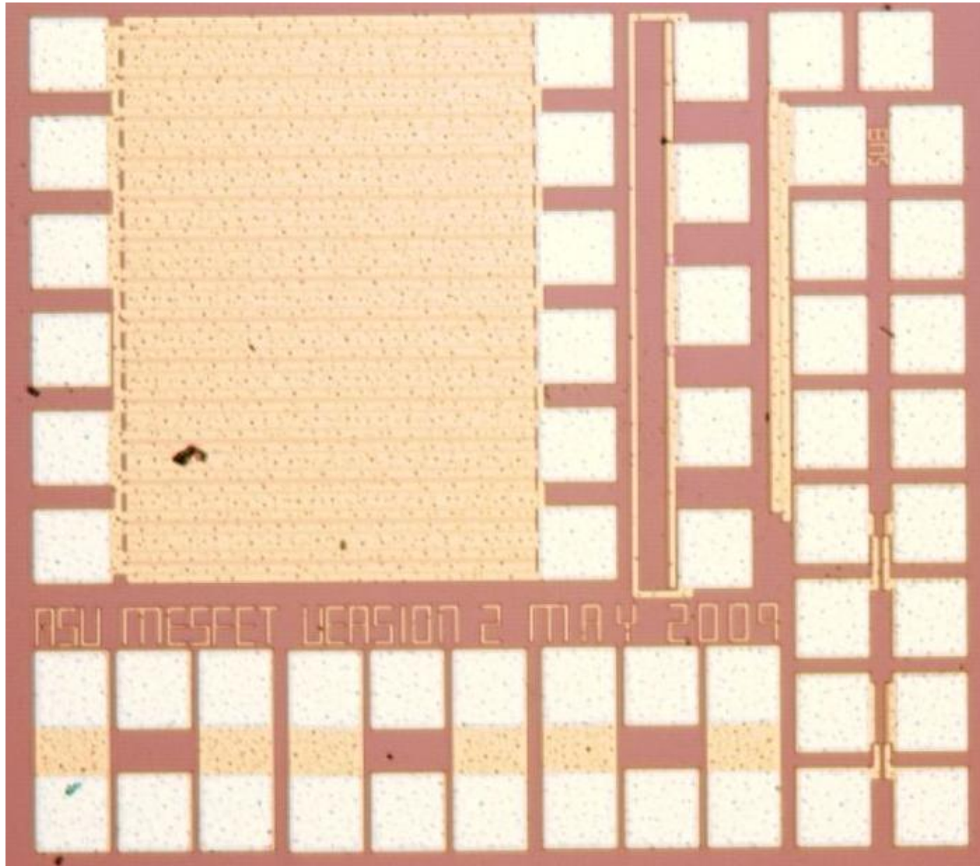

Fig. 86. Picture of bare die which includes the large MESFET device (upper left corner). Excluding pads, the MESFET is 0.73 x 0.55 mm.

APPENDIX C

ADDITIONAL WIDE TEMPERATURE MEASUREMENTS FROM HONEYWELL LDO

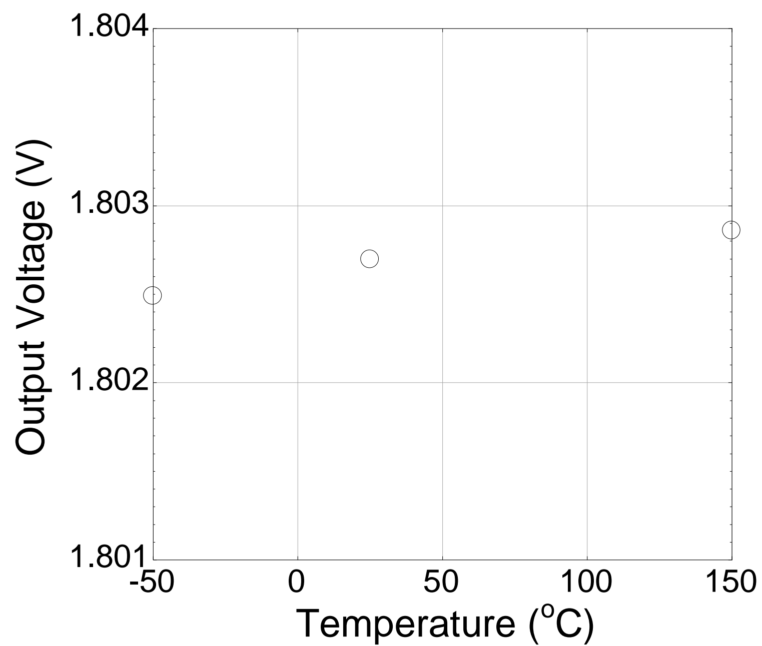

Fig. 87. The regulated output voltage of the Honeywell MESFET regulator was defined at a nominal load of 50 mA and measured over the temperature range of -50 to +150°C.

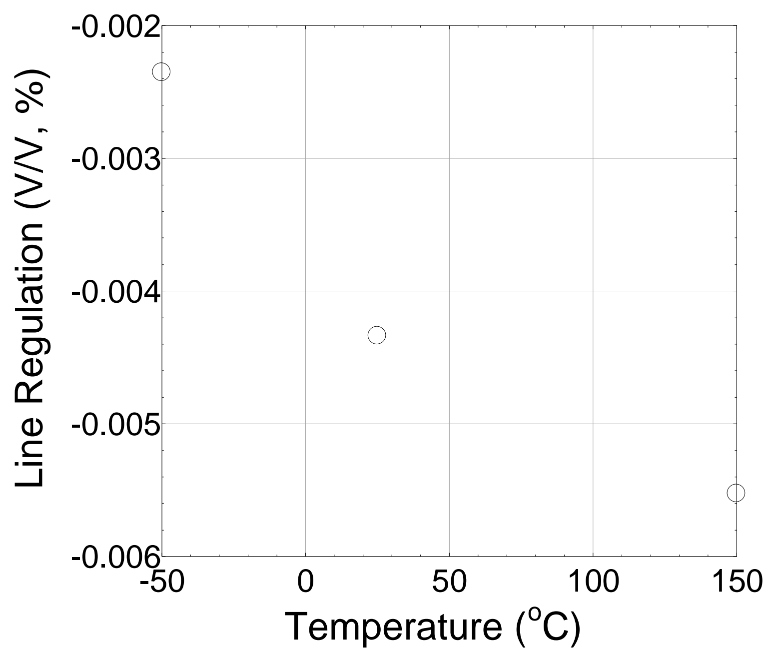

Fig. 88. The line regulation in V/V from -50 to +150°C.

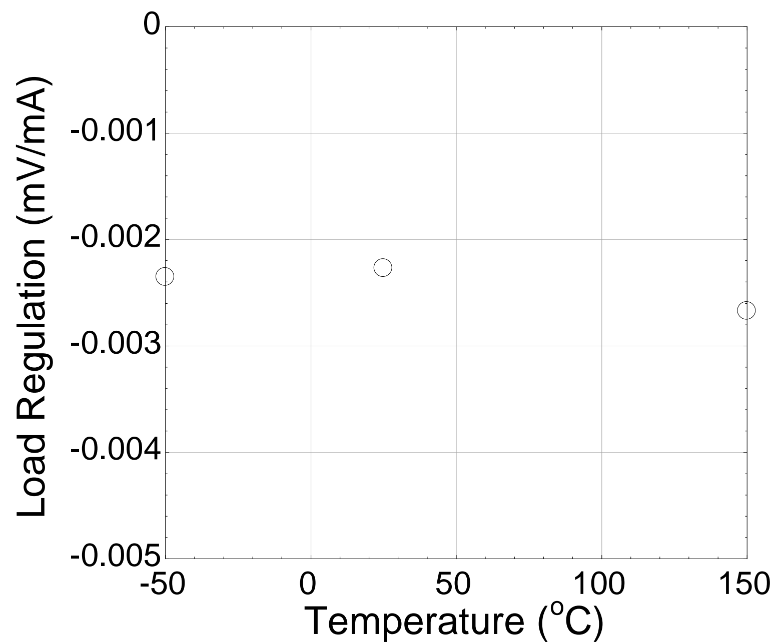

Fig. 89. The load regulation in mV/mA from -50 to +150°C.

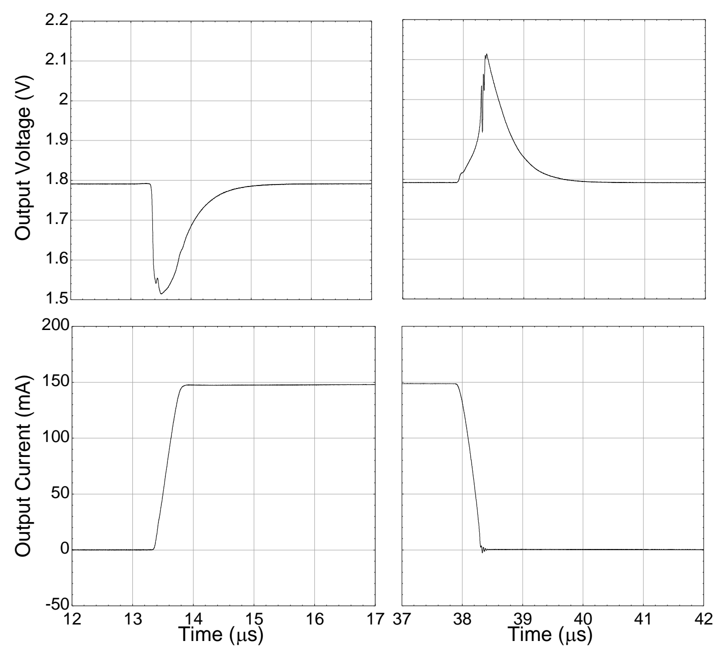

Fig. 90. Transient load regulation with the moderate I_q error amplifier at -50°C. V_{in} = 2.4 V, $t_r = t_f$ = 500 ns and T = 50 μs.

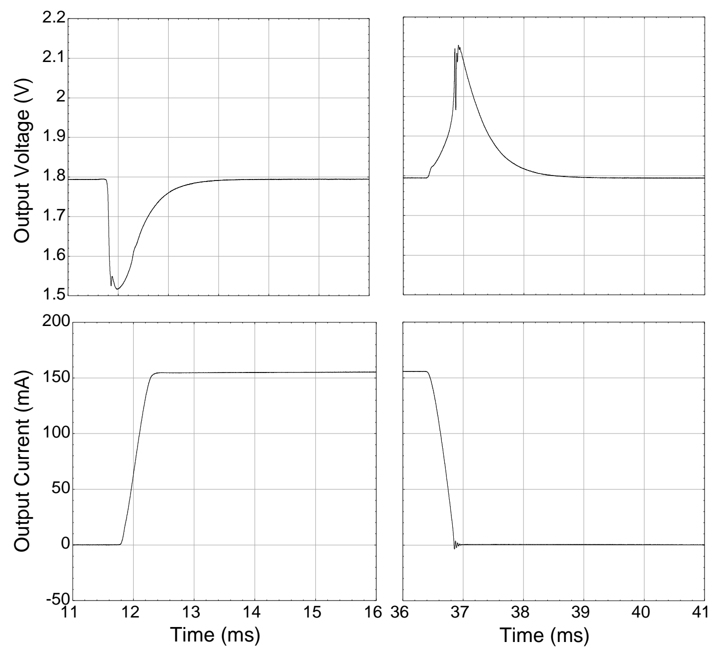

Fig. 91. Transient load regulation with the moderate I_q error amplifier at +150°C. V_{in} = 2.4 V, $t_r = t_f$ = 500 ns and T = 50 μs.

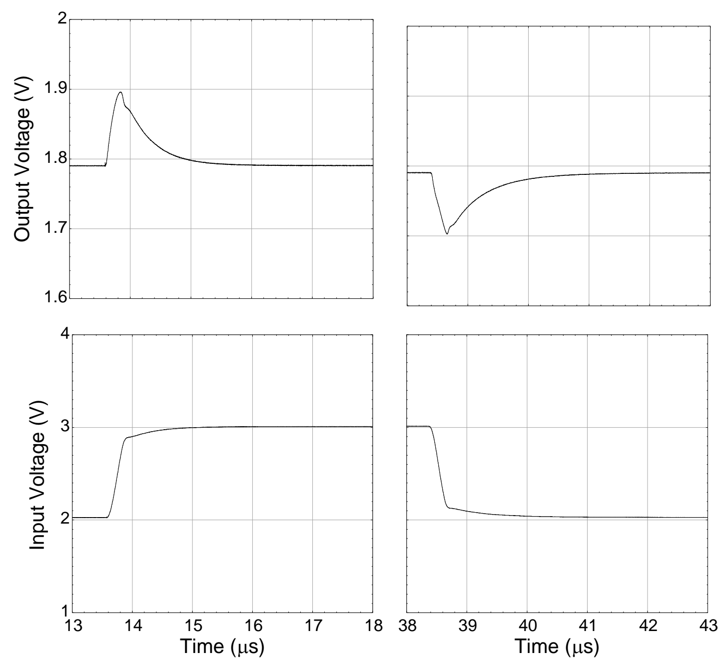

Fig. 92. Transient line regulation with the moderate I_q error amplifier at -50°C. I_{out} = 50 mA, $t_r = t_f$ = 200 ns and T = 50 μs.

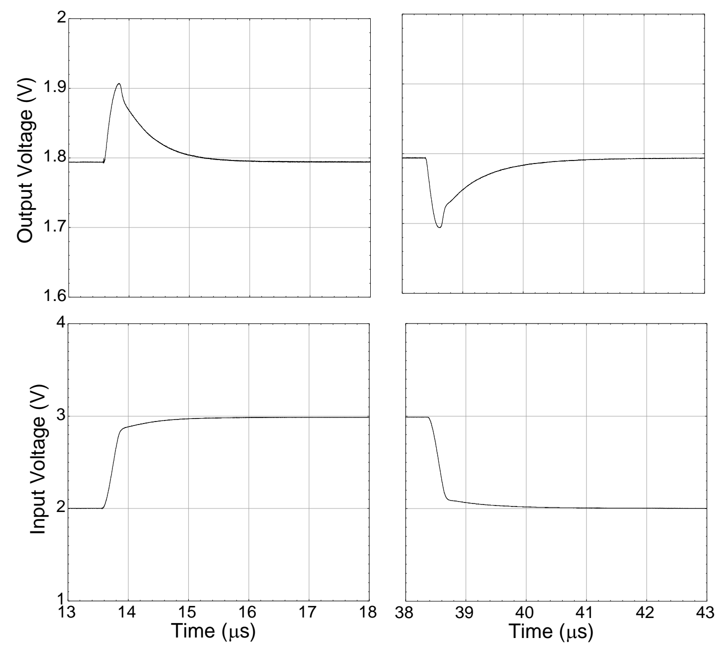

Fig. 93. Transient line regulation with the moderate I_q error amplifier at +150°C. I_{out} = 50 mA, $t_r = t_f$ = 200 ns and T = 50 μs.

APPENDIX D

ADDITIONAL RADIATION MEASUREMENTS FROM HONEYWELL LDO

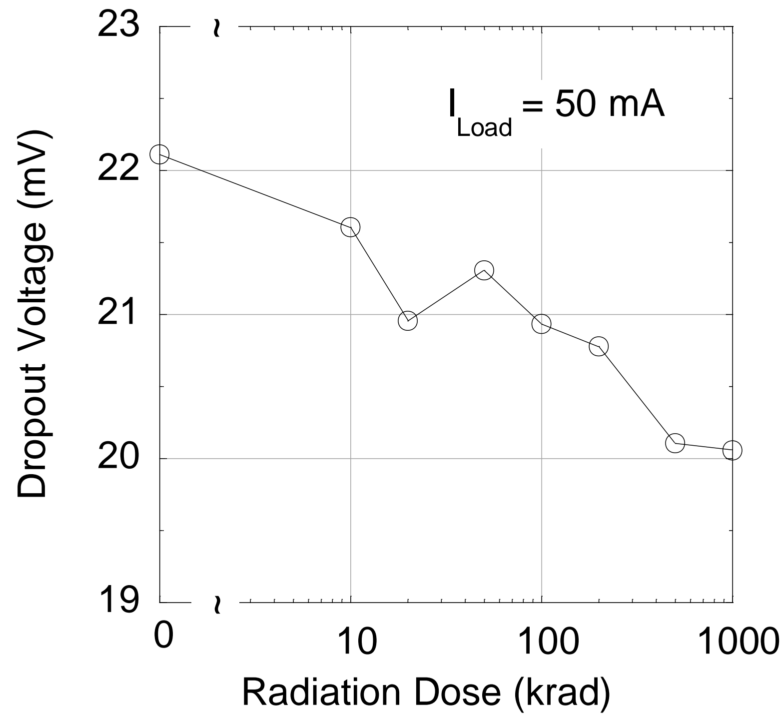

Fig. 94. Dropout voltage verses total ionizing dose at a load of 50 mA.

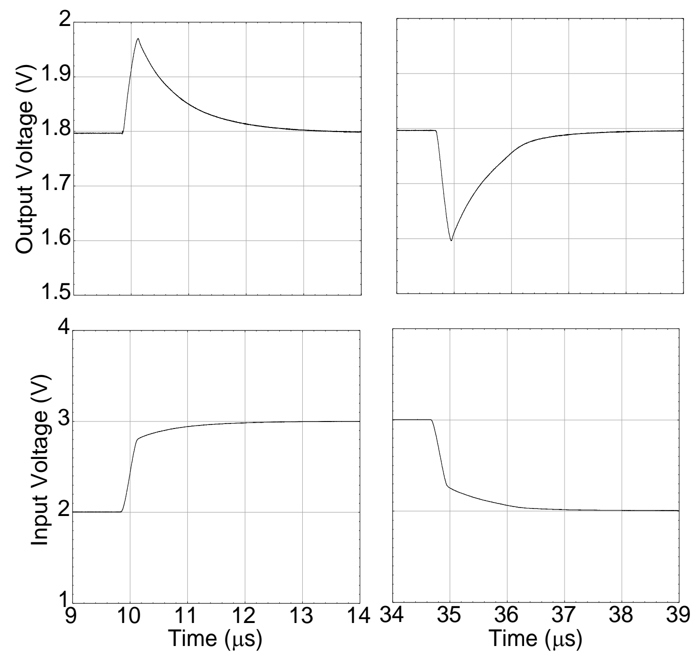

Fig. 95. Transient line regulation with the moderate I_q error amplifier after 1 Mrad(Si). I_{out} = 50 mA, $t_r = t_f$ = 200 ns and T = 50 μs.

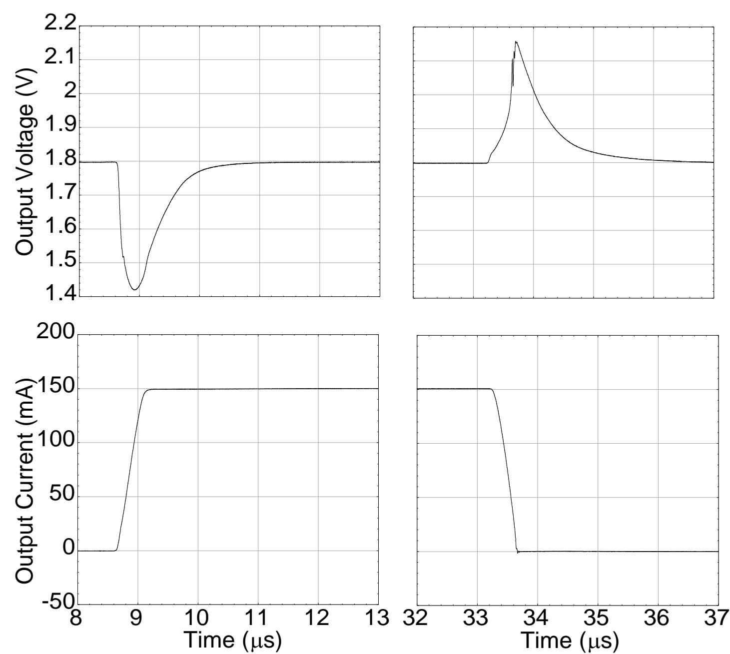

Fig. 96. Transient load regulation with the moderate I_q error amplifier after 1 Mrad(Si). V_{in} = 2.4 V, $t_r = t_f$ = 500 ns and T = 50 μs.

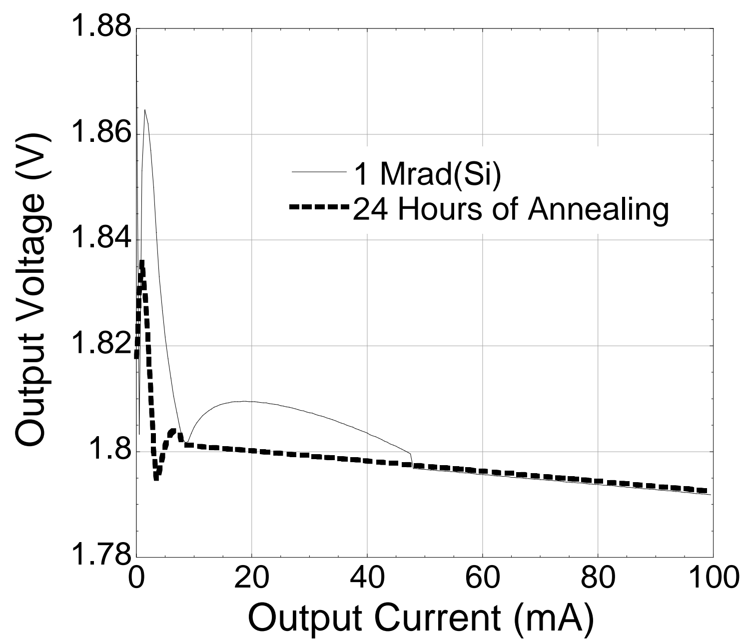

Fig. 97. Load regulation comparing the MESFET LDO immediately after 1 Mrad(Si) and after 24 hours of annealing.

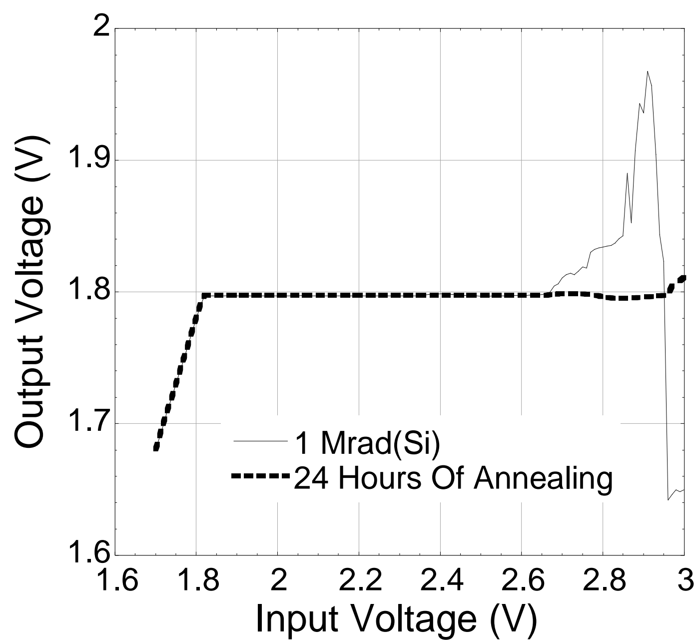

Fig. 98. Line regulation comparing the MESFET LDO immediately after 1 Mrad(Si) and after 24 hours of annealing.

APPENDIX E

3-D LAYOUT OF THE PD-MESFET PASS TRANSISTOR

In this section, Google SketchUp [48] was used to create 3-D drawings to better understand how the layout of the PD-MESFET (Fig. 86) contributed to the operation of the MESFET. While it will not be completely shown here, the total width of the PD-MESFET (119.28 mm) is broken up among 28 equal rows of MESFETs with each row consisting of 426 fingers. Once again, a finger width of 10 µm was chosen since that was the finger size of the devices measured in Chapter 2; however, that is by no means the optimal finger size. The 3-D layout of two interdigitated fingers with widths of 10 µm can be seen in Fig. 99 and Fig. 100.

Fig. 101 shows a picture of 4 of the 28 rows as well as one of the drain and source pads. With the exception of one pad in Fig. 86 being allocated for the gate (fourth pad down on the left), all the pads to the left are for the drain and the ones to the right are for the source. Only one pad was used for the gate since the gate leakage is significantly smaller than the drain current and it does not affect the dropout voltage. The bus lines for the drain run over the MESFETs fingers and consists of metal layers 2 through 6 (M2-M6). The source and gate lines are directly above and below the fingers and consist of all six metals layers (Fig. 102). Fig. 103 and Fig. 104 remove several of the metal lines and all but two of the fingers to show how the MESFET connects to the bus lines.

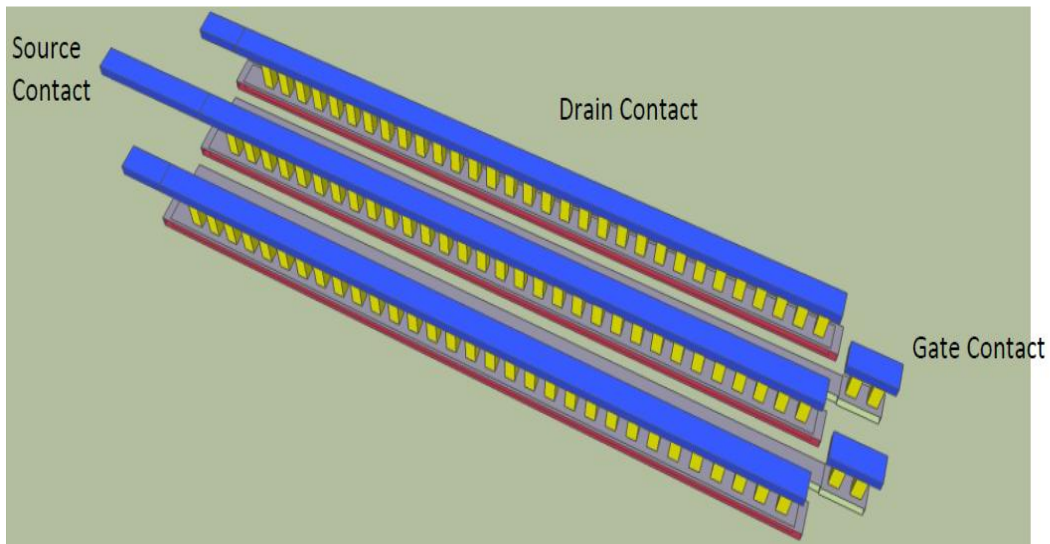

Fig. 99. Layout of two interdigitated fingers.

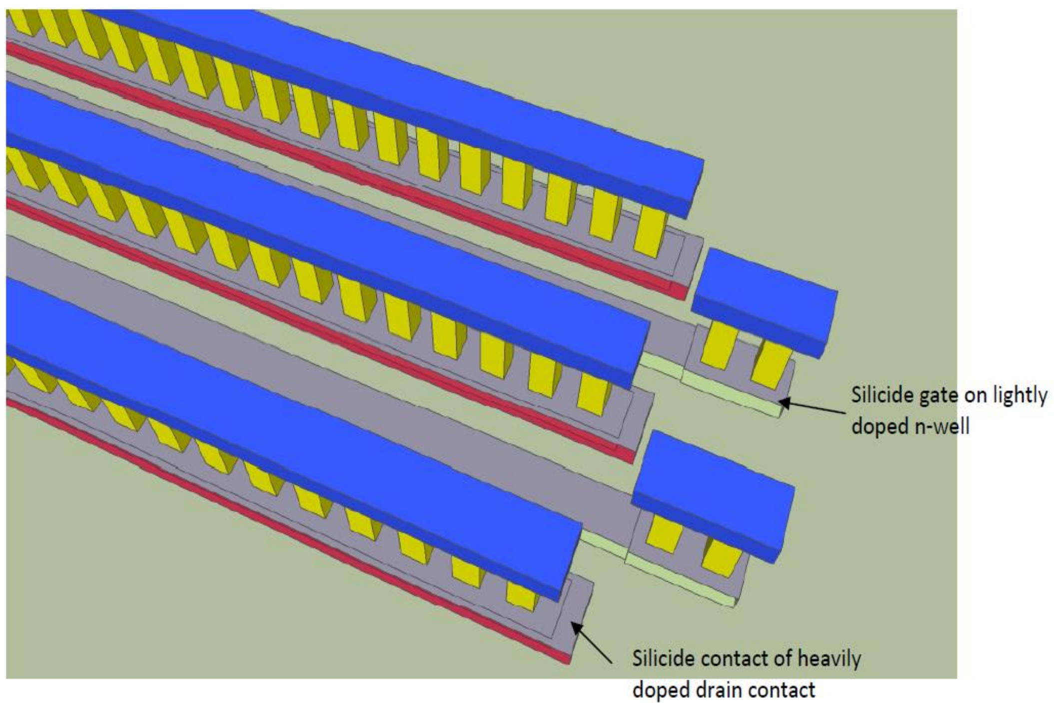

Fig. 100. Shows a zoom in of Fig. 99.

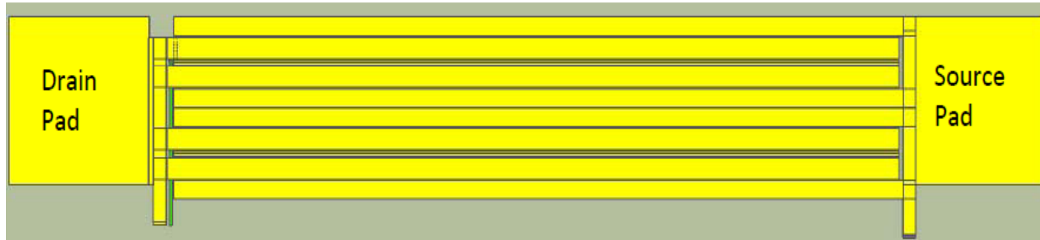

Fig. 101. Shows 4 of the 28 rows in the PD-MESFET pass transistor.

Fig. 102. Zooms in on one section of Fig. 101 to show the source, drain, and gate lines.

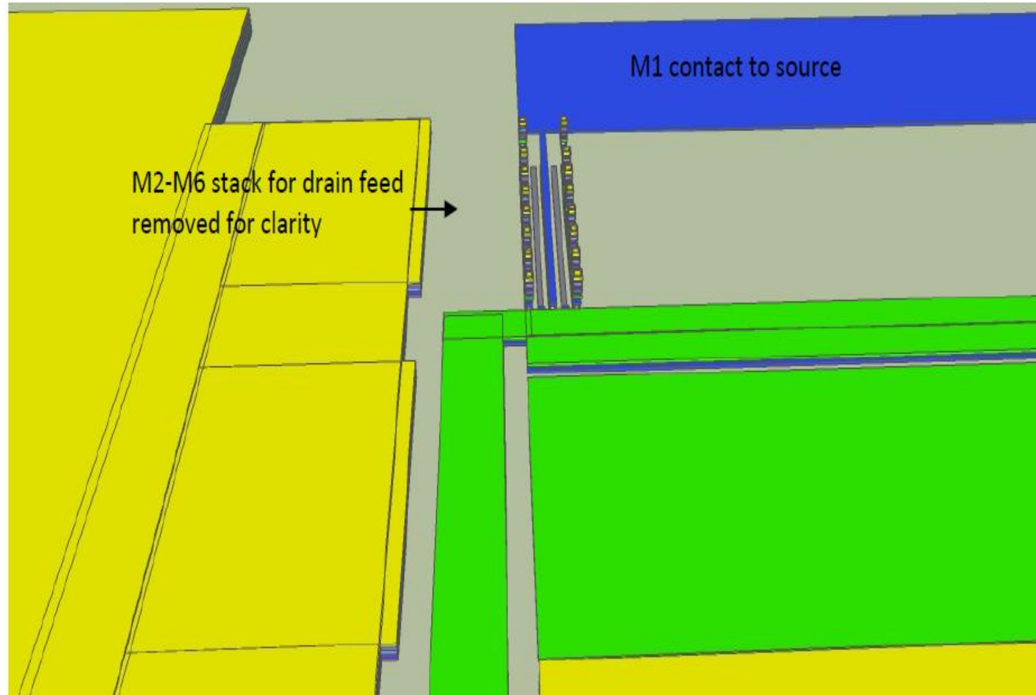

Fig. 103. Removes the entire drain line and some of the metal layers of the source and gate lines in Fig. 102 to show how individual fingers connect to the bus lines. All but two of the fingers were removed to simplify the picture.

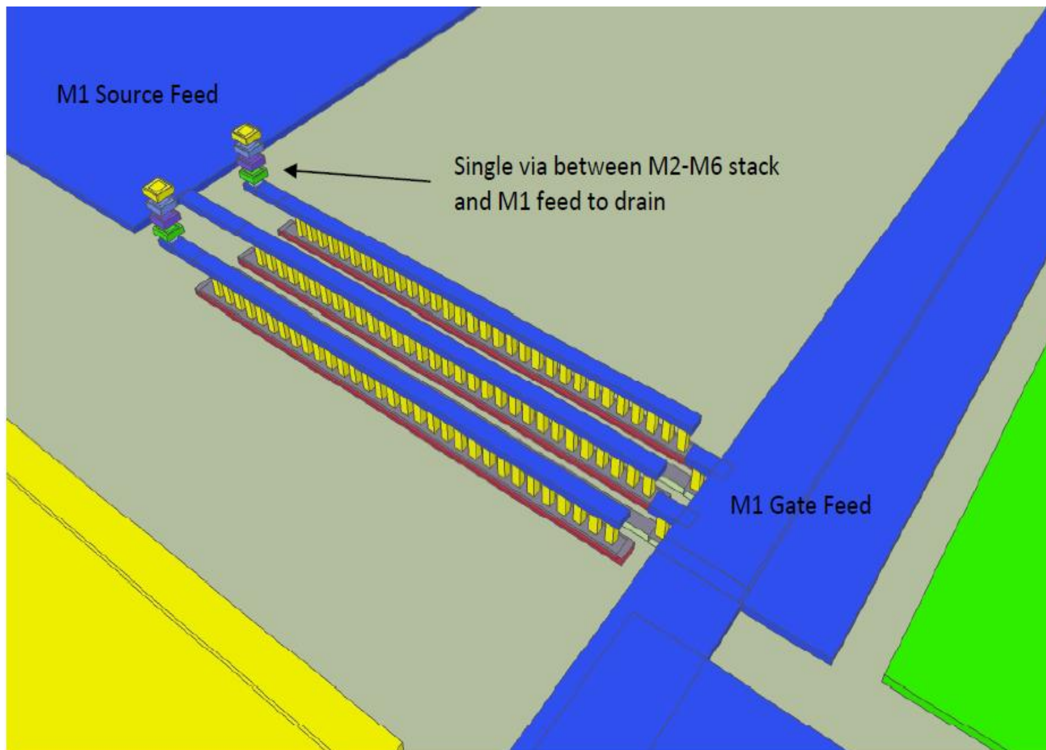

Fig. 104. Shows a zoomed in picture of Fig. 103 as well the via stack which connects the drain lines of the MESFET fingers (M1) to the drain bus line (M2-M6).